Sensorless Control of PMSM Drive Using Sliding-Mode-Observers

Barna Marcell Temesi, Una Gudrun Gautadottir

Energy Technology, MCE3-921, 2020-05

Master's Thesis

Copyright © Aalborg University 2020

Energy Engineering
Aalborg University
http://www.aau.dk

AALBORG UNIVERSITY
STUDENT REPORT

Title:
Sensorless Control of PMSM Drive Using Sliding-Mode-Observers

Theme:
Master Thesis

Project Period:
03.09.2019 - 29.05.2019

Project Group:
MCE3-921

Participant(s):
Barna Marcell Temesi
Una Gudrun Gautadottir

Supervisor(s):
Dong Wang
Kaiyuan Lu

Copies: 1

Page Numbers: 118

Date of Completion:
May 29, 2020

Abstract:

The objective of this project is to develop a sensorless control solution for SPMSM. After a brief introduction, the dynamic model of the system is established, followed by the design of a Field Oriented Control scheme. Next, a Closed-loop flux observer, a first-order sliding mode observer, a second-order sliding mode observer, and a first-order sliding mode observer in dq-reference frame are developed. Two compensation methods, a VSI voltage error compensator, and a feed-forward load torque compensator are introduced. The developed estimators are compared to each other in simulation using standardized testing. It was discovered that SMOdq has the best performance. The feed-forward torque compensator is proven to enhance the transient response. The voltage error compensator and the observer robustness are tested in the laboratory with good results. At last, the SMO was compared to the STO and showed similar trends as in simulations.

The content of this report is freely available, but publication (with reference) may only be pursued due to agreement with the author.

Preface

This thesis is the result of an academic work conducted through 2019-2020. The thesis was issued by the Department of Energy Technology at Aalborg University. Throughout this project the following software was used:

- LaTex - Report writing
- MATLAB - Data analysis, calculation & visualization
- Simulink - Modeling and simulation
- dSPACE Controldesk - Controlling the laboratory setup
- Mendeley - Bibliography organisation tool
- Inskcape - Vector graphics drawing

Reader's Guide: Relevant literature used to complete this project includes textbooks, scientific publications, data-sheets and another relevant tool -& equipment manuals. Relevant sources are cited throughout the report with IEEE citation style. A list of literature is presented in the bibliography.

Tables and figures are numbered according to chapters. All tables and figures are listed in the provided tables and figures lists. All symbols, constants and abbreviations used in the report are listed in the nomenclature.

Aalborg University, May 29, 2020

Barna Marcell Temesi
<btemes18@student.aau.dk>

Una Gudrun Gautadottir
<ugauta18@student.aau.dk>

Summary

For many years, the research and the development of sensorless control for permanent magnet synchronous motors driven at low-speed range have been of interest. The objective of this project is to develop the aforementioned control algorithm under the condition that it performs better than a conventional first-order sliding mode observer.
First, the dynamic model of the system is established, then a Field Oriented Control scheme is designed for simple and effective control of the motor. To get a better understanding of the system, a coupling effect analysis was performed, namely, singular value decomposition. This showed that the coupling effect is weak at the lower speed range, therefore it was disregarded.

Next, different sensorless control algorithms are developed to estimate the speed and angular position of the rotor. A Closed-loop flux observer is established where the observer drives the estimated flux-linkage to the real one, using a PI controller. A first-order sliding mode observer is then designed. This is a non-linear observer with a good disturbance rejection and low sensitivity against model parameter uncertainties. The chattering present in the observer output was attenuated by the implementation of a sigmoid function and by using a complex filtering structure. A second-order sliding mode controller was then introduced to deal with the chattering problem and to potentially require a simpler filtering structure. Another option was to design a first-order sliding mode observer in the dq-reference frame where the current, voltage and back-EMF signals are DC signals, therefore manipulating these signals introduces less phase-lag into the system, which is beneficial.

To further improve the system, two compensation methods are introduced. A VSI voltage error compensator is designed to deal with VSI non-linearities that are caused by the imperfections of the inverter, but mostly by the dead time. A feed-forward torque compensation method was developed to improve the transient response of the system.

Finally, the developed estimators are compared to each other in simulation. It is discovered that the SMOdq has the best performance out of all the estimators. The

feed-forward torque compensator is proven to enhance the transient response by a significant amount. The voltage error compensator and the observer robustness are tested in the laboratory with good results. At last, the first-order sliding mode observer was compared to the second-order sliding mode observer in the laboratory and showed similar trends as in the simulations.

Contents

List of Figures

List of Tables

Nomenclature

Symbols

ϵ	Sigmoid function smoothness tuning parameter	$[-]$
λ_0	Zero-component stator magnetic flux linkage	[Wb.turns]
λ_α,λ_β	Stator magnetic flux linkage on the α-axis and β-axis	[Wb.turns]
λ_d,λ_q	Stator magnetic flux linkage on the d-axis and q-axis	[Wb.turns]
λ_{mpm}	Maximum permanent magnet rotor flux linkage	[Wb.turns]
λ_s,λ_r	Stator and rotor magnetic flux linkage	[Wb.turns]
ω_m	Mechanical rotor speed	[Rad/sec]
ω_r	Electrical rotor speed	[Rad/sec]
σ	Sliding variable	$[-]$
τ	System time constant	$[s]$
θ_{err}	Angle error between the measured position and the estimated one	[Rad]
θ_L	Angle between the real and the estimated reference frames	[Rad]
θ_m	Mechanical rotor position	[Rad]
θ_r	Electrical rotor position	[Rad]
B	Viscous friction coefficient	[Pa s]
C	Coloumb friction coefficient	[N]

e_α,e_β	back-EMF α-axis and β-axis component	$[V]$
e_d,e_q	back-EMF d-axis and q-axis component	$[V]$
f_s	Stator voltage vector frequency	[Hz]
fs	Sampling frequency	[Hz]
i_α,i_β	Line-to-neutral stator current on the α-axis and β-axis	$[A]$
i_{abc}	Line-to-neutral stator current vector on *abc* reference frame	$[A]$
i_d,i_q	Line-to-neutral stator current on the d-axis and q-axis	$[A]$
i_d^*,i_q^*	Reference current signals for FOC	$[A]$
J	Total system inertia	$[kgm^2]$
K_i	Integral coefficient of a PI controller	$[-]$
K_p	Proportional coefficient of a PI controller	$[-]$
K_T	Motor torque constant	[Nm/A]
L_d,L_q	Inductance in d-axis and q-axis	[H]
L_{ls}	Leakage inductance	[H]
L_{md},L_{mq}	Magnetization inductance in d-axis and q-axis	[H]
L_s	Inductance when d-axis and q-axis inductances are equal	[H]
N_{poles},N_{pp}	Number of poles and pole pairs	[-]
p	Differential operator	[-]
R_s	Total system resistance	[Ω]
R_w	Stator resistance	[Ω]
t_{dead}	Dead time of the VSI	[μ s]
T_{dist}	Disturbance torque	[Nm]
t_d	System time delay	[Hz]

T_e	Machine torque	[Nm]
$T_{L,max}$	Expected maximum load torque at start	[Nm]
$t_{r,current}$	Current loop rise time	$[s]$
$t_{r,speed}$	Speed loop rise time	$[s]$
$t_{stcurrent}$	Settling time	$[s]$
t_s	Sampling time	[Hz]
V	Lyapunov candidate function	$[-]$
v_0	Zero-component stator voltage	$[V]$
v_α,v_β	Line-to-neutral stator voltage on the α-axis and β-axis	$[V]$
v_{abc}	Line-to-neutral stator voltage vector on abc reference frame	$[V]$
v_d,v_q	Line-to-neutral stator voltage on the d-axis and q-axis	$[V]$
v_s	Stator voltage vector magnitude	$[V]$
s	Laplace transform variable	$[-]$

Abbreviations

AC	Alternating current
CLFO	Closed-loop Flux observer
DC	Direct current
DSP	Digital signal processor
DTC	Direct torque control
EMF	Electromotive force
FOC	Field oriented control
IM	Induction motor
LPF	Low pass filter

LTID	Load torque identification
MIMO	Multiple-input, multiple-output
MTPA	Maximum torque per ampere
N.D.	Negative-definite
N.S.D.	Negative semidefinite
P.D.	Positive-definite
PCB	Printed circuit board
PI	Proportional Integral controller
PLL	Phase-locked loop
PMSM	Permanent magnet synchronous motor
PWM	Pulse width modulation
QSMO	Quasi-Sliding Mode Observer
RGA	Relative gain array
RHP	Right-hand pole
RMSE	Root mean square error
RPM	Round per minute
sat	Saturation function
sgn	Sign function
SISO	Single-input, single-output
SMO	Sliding Mode Observer
SMOdq	Sliding Mode Observer in estimated dq-reference frame
SPMSM	Surface mounted permanent magnet synchronous motor
STO	Super twisting observer

SVD	Singular value decomposition
SVM	Space vector modulation
VSI	Voltage source inverter

Chapter 1

Introduction

1.1 Study of the background

The development of sensorless synchronous motor control has been the focus of researchers for many years now. A better understanding of the machines and the rapid advancement in control and observer methods, thanks to other industries, made the performance and efficiency of sensorless control techniques get closer and closer to the sensored ones. Many techniques take advantage of the increased computational power present in modern systems. This allows engineers to use algorithms with online calculations that can adapt to continuously changing challenges faced by the controller or observer.
Sensorless control is beneficial in multiple ways. It makes it possible to remove the encoder from the system, which results in a less expensive and smaller overall system. Both of these results are advantageous in many novel use-cases [1][2].

Also, the encoder in the system is a possible failure point, which could be eliminated and that would increase the overall robustness of the system. Another consideration is to make the system more robust against failures by introducing fault-tolerant control techniques. Having both the encoder and the sensorless algorithm implemented in a system, in case of a detected encoder fault, the controller could switch over to the estimated signals. This is paramount in modern systems like autonomous vehicles where safety is a high priority. Detecting the fault could be done by comparing the encoder and observer signals and forming a residual out of them [3]. This is an efficient way of making a system, including a synchronous machine, more robust against failures without considerably increasing the cost or the weight of it.

1.2 Problem Analysis

This section gives an overview of the system components and also provides a framework of information before the beginning of the study. There are various possible control techniques currently present in the literature. A general comparison between them is also given in the lines below.

Machine description and classification

The subject of this report is a permanent magnet synchronous motor (PMSM). The rotor and the motor magnetic field are rotating synchronously. The rotor magnetic field is established by permanent magnets placed in the rotor in various ways. The placement of the magnets defines the type of motor. When the magnets are located on the surface of the rotor, the machine is called surface-mounted PMSM. When the magnets are located inside the rotor structure, we are talking about an interior PMSM [4].

The type of the most used electric motor is the induction machine. These are cheap to manufacture and control. Now, the rotor rotates at a slower speed than the stator magnetic field. The slip is an important variable here and it is defined as a function of the speed difference. The slip induces current in the rotor. The value of it is usually around 5%. With increasing load torque, the slip increases as well to stabilize the system [4].

The other large class of electric motors is the switched reluctance machine, which generates torque through the minimization of reluctance lines. This rotor is machined in a shape to optimize this effect. Reluctance machines require a more complex control system. On the other hand, synchronous reluctance machines also exist and their control is similar to the control of PMSMs.

Control type of PMSMs

The two most used methods to control PMSMs are direct torque control (DTC) and field-oriented control (FOC). In some variations of DTC, the torque is controlled by the stator flux angle instead of the current. This eliminates the need for current sensors in the system [5]. This mentioned angle will quickly change the torque, which can be controlled by changing the terminal voltage. The advantage of this method is excellent torque dynamics, no need for current sensors, no need for pulse-width modulation (PWM), or reference frame transformations. The disadvantage of the method is that the sampling frequency has to be much higher (around 40 Khz) than in other applications [6].

The other one, FOC, is easy to implement, but it is heavy on the computation side due to the use of multiple reference frame transformations. It also requires too

precise measurement of the rotor position. It separates the control of flux and torque which is beneficial. Using FOC allows free choice, magnitude and angle, of the current vector. In practical applications, FOC commands the current vector to be aligned with the q-axis and this results in maximum-torque-per-ampere for SPMSMs. However, this is not necessarily true for other motor structures [4].

Sensorless control for low speeds

Sensorless control for low speeds is notably problematic due to the low magnitude of the measured signals compared to the noise or the back-EMF, which eventually vanishing at zero speed. Methods based on rotor saliency and the change of the saliency were invented and researched.

The most popular method is called INFORM. It is based on the fact that the magnetic anisotropy of the rotor gives information about its position. The magnetic anisotropy is detected by injecting test voltages, then measuring the change in the stator current vector. Low-pass filters are needed to extract the high frequency current component which is fed back to the current controllers. Low-pass filters introduce phase delay into the system which in result, limits the bandwidth of the current controllers. In case the filtering is not adequate, torque ripples can occur in the system [7].
There are several methods based on this estimation principle, they only differ in how the voltage vector is injected. There are two widely used types, one injects a rotating voltage vector in the stationary reference frame [8], the other injects a pulsating voltage vector in the estimated d^*-axis or q^*-axis of the estimated rotor reference frame. Feeding the calculated difference signal through a PLL, the speed and position signals now can be acquired [9].

The Square-wave type voltage injection method relies on the injection of high-frequency square-wave-type voltage. The frequency is chosen to be half the sampling frequency. This frequency is much higher than the frequency of the injected voltage in other methods. Filtering is still needed in this case, but the cut-off frequency of the low-pass filters can be increased alongside with the bandwidth of the current controllers. This enhances the overall performance of the system [10].

Sensorless control for high speeds There are several different methods to estimate the rotor speed and position when the motor is operating in the medium-high speed range. Three techniques will be listed here.
Flux-linkage based methods are calculating the flux-linkage vector for every sampling cycle, based on the system model and the measured voltage and current. The flux-linkage is obtained through integration [11]. This part causes the most problem because the integrator value might start to drift due to possible measurement errors (incorrect calibration) which gets integrated. Both open-loop and closed-loop DC-drift removal methods are present in the literature [12].

The next big family of sensorless control methods is using a Kalman-filter. A Kalman-filter is an optimized state-observer, in this case, it is a reduced-order state-observer. The Kalman-filter is usually utilized in the dq-reference frame because the system equations can be linearized in this case. The gain of the observer is based on the noise present in the measurement signals and the uncertainty present in the model equations of the system [13].

Sliding mode observers are also a popular choice by control engineers. These are nonlinear observers. They are widely used because of their robustness against disturbances and parameter uncertainties present in every real system. This robustness is achieved by constructing a sliding surface in state space, and by making the control or observer law discontinuous across the surface. This causes chattering in the output signal, which is the drawback of using sliding mode observers. Attenuation of the chattering is the biggest challenge control engineers have to face during the design [1].

Open-loop startup methods

The two most used open-loop methods are V/f control and $I-f$ control. Open-loop startup techniques are often used when the criteria of performance are not strict. This results in a simpler system with fewer components. In the case of speed control, in open-loop control, the speed is not fed back to the controller. This means, an encoder is not needed, which saves weight and money. This heavily reduces the robustness of the system, because it is only assumed now that the speed matches the reference speed. The handling of load torques and the rejection of disturbance torques have to be carefully considered during the design process [14].

For research purposes, the system can also be started from a standstill using sensored FOC and then switching to the given sensorless control scheme.

Voltage modulation techniques

The system uses the commonly used topology, PWM-VSI, therefore other topologies, such as square wave or CSI, will not be discussed in this report.

There are several PWM techniques present in the literature and also in the industry [15]. One of modulation technique is ST-PWM with an added third harmonic component. The pulse width modulation duty cycles are calculated by comparing the reference signal with a high-frequency triangle carrier signal. The amplitude of the output sine wave can be increased by 14% using third-harmonic injection. This method increases the linear range which means, that the available DC-link voltage is better utilized.

Space vector modulation, as the name suggests, utilizes the space voltage vector,

which is constructed by summing the three voltage vectors. Then, the duty cycles can be calculated by using the angle and amplitude information of the vector. Using this method, more harmonics are added to the phase voltage, but that does not matter, because they cancel each other out when line-to-line voltage is considered. The advantage of using SVM is that the current ripple will be smaller than in the case of other modulation techniques [15].

Discontinuous PWM is a technique used to reduce inverter losses. One of the zero vectors is omitted and this eliminates one switching transition in each half carrier interval. This reduces the switching losses by 33%. The disadvantage of this method is that many harmonics are introduced [15].

1.3 System Description

The main components of an AC motor drive are a three-phase, two-level inverter, an AC motor, and a mechanical load. The inverter supplies electrical power to the motor, and the motor converts it to mechanical power required to drive the load. Although, the main focus of this project is the AC motor, unknown parameters, disturbances, and non-linearities arise from each of the components and have effects on the control performance.

In figure 1.1 the actual setup located in the laboratory is shown. For better understanding, a summarizing overview of the system is shown in figure 1.2.

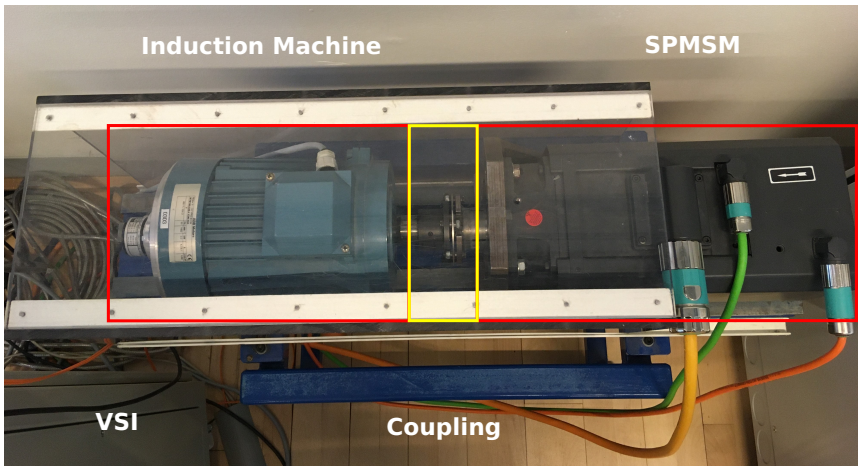

Figure 1.1: *The main components of the actual setup located in the laboratory.*

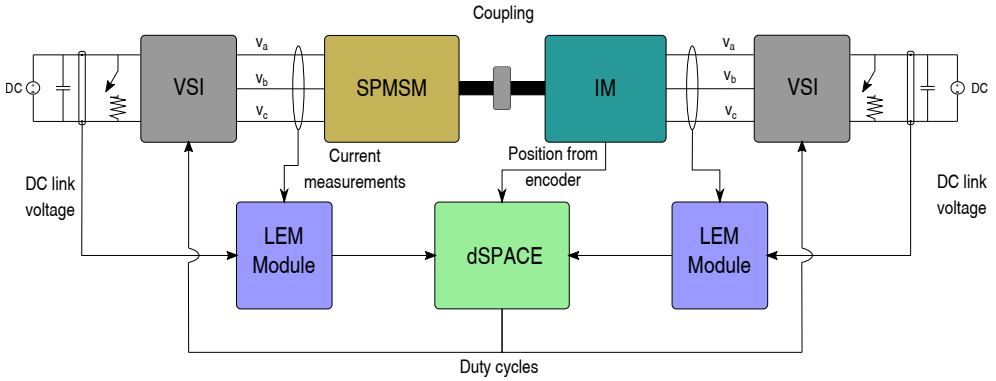

Figure 1.2: *Schematic of the test setup.* [16]

The setup consists of an SPMSM machine, which is coupled to an induction machine (IM). However, this project only focuses on the SPMSM machine. The IM machine is only there to provide the desired load torque.
The controllers and compensators are designed and tested in Matlab / Simulink. After that, the model is translated into a code which the dSPACE system can read and understand. The dSPACE system then measures the currents (using a LEM module) and voltages (using the DC link voltage information). Using these signals and the provided code, the outputs of the system are updated in every cycle.
The DC link voltage is provided by the central rectifier in the lab.
As a feature, the system states can be measured and stored by the dSPACE system. The captured data is then processed using Matlab.

1.4 Problem Statement

The main objective of this thesis is to develop a sensorless control strategy for a PMSM motor that performs better than the sliding mode observer established in the report [16]. It would be advantageous as well to reduce the complexity of the system, to simplify the filtering structure required. The main variables that determine the system performance are the following: lowest achievable speed, position angle error, and tracking performance. The improvements might be done by introducing compensators to the previously mentioned system, or by implementing an observer which is based on a new principle.
Also, the system has to be stable and has to be able to handle a step-load change.

First of all, new techniques and methods have to be introduced and analyzed. After re-tuning the system, a performance baseline has to be determined, so the new methods can be compared to the original one. Following a standard testing

procedure, the new performance values have to be recorded and processed using statistical methods.

1.4.1 Performance criteria

As the main guidelines, certain performance factors are defined here and shown in table 1.1.

Table 1.1: *Design Criteria of control loops*

	Main criteria	Sub criteria
Current loop	Max. 5% overshoot	Zero steady-state error
Speed loop	Max. 15% overshoot	Zero steady-state error
Pos. angle error	Max. 5°	Max. $\pm$ 1°variation
Stead-state speed error	0 rpm	Ripple max. 5 rpm
Load-torque rejection	Min. 10 Nm	
Operation speed range	Min. 300 rpm	Has to reach rated speed

1.5 Limitations and Assumptions

During this project, certain limitations and assumptions are made. These are summarized in the table 1.2 below.

Table 1.2: *System limitations and assumptions*

Component	**Description of the limitation, assumptions**
System	Is symmetric and balanced
VSI	Generates the voltage perfectly from the duty cycles
Magnetic core	Magnetic saturation limits are not reached
Machine electric losses	Such as core losses, Eddy current losses etc are neglectable
Motor parameters	Are constant as well as the device temperature
Sampling frequency of the system	5 kHz
Switching frequency of the VSI	5 kHz

The limitations and assumptions will be kept in mind during the report and the

effects of them will be discussed, when necessary.

1.6 Project Outline

Firstly, in chapter 2 the dynamic model of the SPMSM is established, and then the state-space model is formulated. The state-space model is necessary for further analysis of the system.

In chapter 3, Field oriented control is introduced. This requires the use of a cascade control scheme. The inner loop consists of the current controller, and the outer loop consists of the speed loop. Alongside these, the necessary startup method is also introduced which enables the system to start from a standstill.

In chapter 4, using the state-space model, the coupling effect is analyzed. This is an important aspect of the analysis because, during sensorless operation, the voltage equations cannot be de-coupled.

In chapter 5, the speed, and position estimators are introduced. A closed-loop flux linkage observer is designed, a first-order sliding mode observer, and a super-twisting observer which is second-order. Last but not least, a first-order sliding mode observer in estimated dq-reference frame is developed. The stability property of them is then further investigated. Previously observed DC-offset problem in the estimated back-EMF signals is investigated at the end of the chapter.

In chapter 6, compensation methods for the system are introduced and discussed. First, the VSI voltage error is discussed, then a simple compensation strategy is presented based on the dead time of the given inverter. Lastly, a feed-forward torque compensation method is presented. Details about the two-level inverter and the used modulation technique can be found in Appendix B.

Chapter 7, presents the standardized testing method, the tuning process of the controllers and observers, then shows the simulation results from all of the modeled algorithms. The data is also evaluated using statistical calculations.

Chapter 8, presents the used tuning process of the controllers and observers in the laboratory. First, the voltage error compensator is tested. The sensitivity to parameter changes of the observers is also investigated. Also, the SMO is compared to the STO using the test setup.

Chapter 9, gives the discussion and conclusion of the thesis. The chapter examines whether the requirements presented in the Problem statement section are met or not. The chapter also summarizes the results of the experiments in a more tangible way.

Finally, in chapter 10, the outlook of the possible improvements of the discussed methods are briefly presented.

Chapter 2

Modelling of the system

As in every design process, after the problem statement, the system has to be modeled and analyzed. This starts with an overview of the motor parameters. Next, the motor voltage equations, which are already given in the dq-reference frame, are examined. The mechanical equation of the motor is also presented.
As the last step, the state-space model of the surface-mounted permanent magnet synchronous machine (SPMSM) is established which will be used for advanced analysis tools presented in later chapters.

2.1 Synchronous machine modelling

The motor, in the scope of this thesis, is an SPMSM. This means that the permanent magnets are located on the surface of the rotor. Due to this, the motor is non-salient, and also the reluctance path is equal on the d- and q-axis. This results in equal inductance on the d- and q-axis. For easier understanding, the machine inductance will be denoted as L_s.

$$L_d = L_q = L_s \tag{2.1}$$

The most important parameters of the motor and the other necessary system parameters are listed in the table 2.1.
As can be seen from the table, the motor has 4 pole pairs. Generally speaking, this means that the machine is more geared towards high-speed operation. In high-torque operation applications, like in the case of a steering motor, the number of poles might exceed a 100.

In simulations, the total system resistance will be used, which takes into account the resistance of every possible component in the setup.

Table 2.1: *System parameters, from previous projects such as* [16],[17]

Description	Notation	Value	Unit
Number of pole pairs	N_{pp}	4	-
Winding resistance	R_w	0.19	Ω
Total system resistance	R_s	0.268	Ω
q and d-axis inductance	L_m	2.2	mH
Rotor PM flux linkage	λ_{mpm}	0.12258	wB
Rated speed, SPMSM	$\omega_{m,rated}$	4500	rpm
Rated torque, SPMSM	$\tau_{m,rated}$	20	Nm
Rated power, SPMSM	$P_{m,rated}$	9.4	kW
Rated speed, IM	$\omega_{IM,rated}$	1400	rpm
Rated torque, IM	$\tau_{IM,rated}$	14	Nm
Rated power, IM	$P_{IM,rated}$	2.2	kW
Rated current, VSI	I_{VSI}	35	A
IM machine inertia	J_{IM}	0.0069	$kg \cdot m^2$
SPMSM machine inertia	J_{SPMSM}	0.0048	$kg \cdot m^2$
Total system inertia	J_{sys}	0.0146	$kg \cdot m^2$
Coulomb friction	C	0.2295	Nm
Viscous friction	B	0.0016655	N

The motor voltage equations are shown in equation (2.2). Due to the assumption that the system is symmetrical and balanced, the zero term (v_0) is zero [6].

The detailed derivation of these equations from *abc*-reference to *dq*0-reference is explained in appendix A.

$$\begin{aligned} v_d &= R_s i_d + p\lambda_d - \omega_r \lambda_q \\ v_q &= R_s i_q + p\lambda_q + \omega_r \lambda_d \\ v_0 &= 0 \end{aligned} \tag{2.2}$$

In the *abc*-reference frame, the machine flux-linkage is dependent on position and the machine inductance is constant for a non-salient pole machine, but because the model is already transformed into the *dq*0-reference frame, the machine inductance is constant.

The stator *dq*0-reference frame is aligned with the rotor reference frame, which is naturally in the *dq*0-reference frame. The rotor *d*-axis is chosen to be aligned with

the maximum flux density line at no load condition. The q-axis is always leading the d-axis by 90°electric. This way, it is aligned with the minimum flux density line [6].

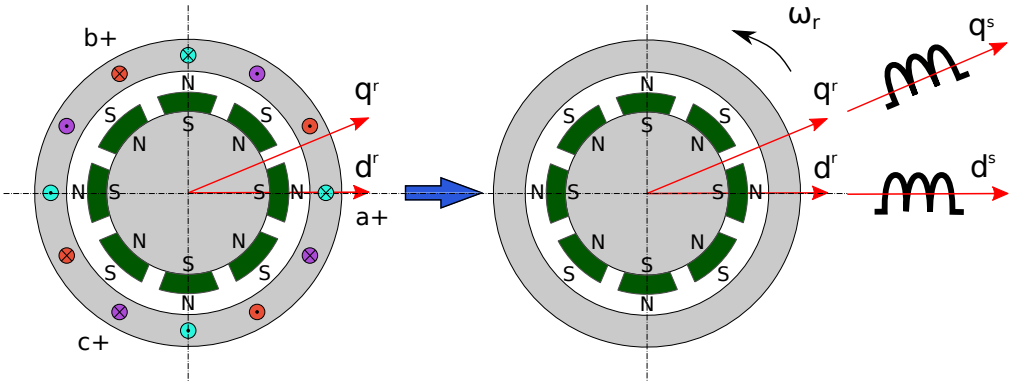

Figure 2.1: *Reference frame transformation from **abc** to dq. The structure of the motor is also shown. Inspiration [6]*

The two d-axis is in line now. This is convenient because, it results in the d-axis and the q-axis flux-linkage as shown in equation (2.3).

$$\begin{aligned} \lambda_d &= (L_{ls} + L_{md})\, i_d + \lambda_{mpm} = L_d i_d + \lambda_{mpm} \\ \lambda_q &= \left(L_{ls} + L_{mq}\right) = L_q i_q \\ \lambda_0 &= 0 \end{aligned} \tag{2.3}$$

After substitution, the voltage equations may be rewritten as seen in equation (2.4).

$$\begin{aligned} v_d &= R_s i_d + p(L_d i_d + \lambda_{mpm}) - \omega_r L_q i_q \\ v_q &= R_s i_q + p(L_q i_q) + \omega_r (L_d i_d + \lambda_{mpm}) \end{aligned} \tag{2.4}$$

Where p is the differential operator $\frac{d}{dt}$. Differentiating the equation, keeping in mind that the derivative of a constant is zero, will result in the following.

$$\begin{aligned} v_d &= R_s i_d + L_d p i_d - \omega_r L_q i_q \\ v_q &= R_s i_q + L_q p i_q + \omega_r (L_d i_d + \lambda_{mpm}) \end{aligned} \tag{2.5}$$

In one more step, the homogeneous first-order differential equation of the system is acquired.

$$\begin{aligned} \frac{d}{dt}i_d &= -\frac{R_s}{L_d}i_d + \frac{1}{L_d}v_d + \omega_r\frac{L_q}{L_d}i_q \\ \frac{d}{dt}i_q &= -\frac{R_s}{L_q}i_q + \frac{1}{L_q}v_q - \omega_r\frac{L_d}{L_q}i_d - \frac{1}{L_q}\omega_r\lambda_{mpm} \end{aligned} \tag{2.6}$$

Equations (2.4) also contain the back-EMF voltage components which are very important in position estimation, hence they are highlighted here:

$$\begin{aligned} e_d &= -\omega_r L_q i_q \\ e_q &= \omega_r(L_d i_d + \lambda_{mpm}) \end{aligned} \tag{2.7}$$

The governing torque equation can be derived from the equation of the input power of the windings. Simplifying this equation, using the attributions of the SPMSM machine, yields the following expression:

$$T_e = \frac{3}{2}N_{pp}\left(\lambda_d i_q - \lambda_q i_d\right) \tag{2.8}$$

$$T_e = \frac{3}{2}\frac{N_{poles}}{2}\left(\lambda_{mpm} i_q + (L_d - L_q) i_d i_q\right) \tag{2.9}$$

$$T_e = \frac{3}{2}N_{pp}\left(\lambda_{mpm} i_q\right) \tag{2.10}$$

Using Newton's second law, the mechanical equation of the system can be derived as shown in equation (2.11).

$$T_e = J\frac{d\omega_m}{dt} + B_m\omega_m + T_{dist} \tag{2.11}$$

Where J is the total system inertia and T_{dist}, the disturbance torque, consists of the load torque and Coulomb friction. The total system inertia includes the inertia of both the IM and PMSM machine and also the coupling and fastening components between them.

The first term is related to the torque needed to accelerate the system without friction, the last two terms are related to the torque which is needed to overcome the viscous friction and the disturbance torque, respectively.

2.2 SPMSM State Space Model

In this section, using the voltage equations of the machine expressed as first-order differential equations shown in equations (2.6), the state space form is developed [18]. This can be seen in equations (2.12) and (2.13).

$$\begin{aligned} \dot{x} &= Ax + Bu \\ y &= Cx \end{aligned} \tag{2.12}$$

$$\begin{aligned} \begin{bmatrix} \dot{i}_d \\ \dot{i}_q \end{bmatrix} &= \begin{bmatrix} -\frac{R_s}{L} & \omega_r \\ -\omega_r & -\frac{R_s}{L} \end{bmatrix} \begin{bmatrix} i_d \\ i_q \end{bmatrix} \\ &\quad + \begin{bmatrix} \frac{1}{L} & 0 & 0 \\ 0 & \frac{1}{L} & -\frac{\omega_r}{L} \end{bmatrix} \begin{bmatrix} u_d \\ u_q \\ \lambda_{mpm} \end{bmatrix} \\ C &= \begin{bmatrix} 1 & 0 \\ 0 & 1 \end{bmatrix} \end{aligned} \tag{2.13}$$

The transfer function from u_d and u_q to i_d and i_q is found using the equation (2.14).

$$\begin{aligned} G(s) = C(sI - A)^{-1}B &= \begin{bmatrix} 1 & 0 \\ 0 & 1 \end{bmatrix} \left(\begin{bmatrix} s & 0 \\ 0 & s \end{bmatrix} - \begin{bmatrix} -\frac{R_s}{L} & \omega_r \\ -\omega_r & -\frac{R_s}{L} \end{bmatrix} \right)^{-1} \begin{bmatrix} \frac{1}{L} & 0 & 0 \\ 0 & \frac{1}{L} & -\frac{\omega_r}{L} \end{bmatrix} \\ &= \begin{bmatrix} g_{11}(s) & g_{12}(s) & g_{13}(s) \\ g_{21}(s) & g_{22}(s) & g_{23}(s) \end{bmatrix} \end{aligned} \tag{2.14}$$

The transfer functions can be expressed such as:

$$g_{11} = \frac{s - R/L}{HL} \tag{2.15}$$

$$g_{12} = \frac{\omega_r}{HL} \tag{2.16}$$

$$g_{13} = -\frac{\omega_r^2}{HL} \tag{2.17}$$

$$g_{21} = -\frac{\omega_r}{HL} \tag{2.18}$$

$$g_{22} = \frac{s - R/L}{HL} \tag{2.19}$$

$$g_{23} = -\frac{(s - R/L)\omega}{HL} \tag{2.20}$$

Where $H = s^2 - 2s\frac{R}{L} + \frac{R}{L}^2 + \omega_r^2$, which is the determinant of matrix A, and used for the matrix inverse calculations. The calculations were aided by MATLAB.

Equation (2.14) gives 6 transfer functions. These transfer functions describe the linearised system when the coupling between the voltage equations, due to λ_d and λ_q, is present.

In the next chapter, the control of the SPMSM will be discussed. Later on, in chapter 4, the coupling effect is going to be analyzed using the state-space model of the system.

Chapter 3

Control of the SPMSM

In this chapter, the control scheme of the SPMSM motor is explained shortly, namely the Field Oriented Control (FOC). This chapter is heavily based on [16], because the main focus is on the design of the estimators, and not on FOC.

3.1 Field Oriented Control

Field Oriented Control (FOC) is a widely used control technique for controlling AC machines due to its efficiency. The idea of FOC is to control the torque and the flux-linkage separately. For an SPMSM when the current vector is chosen to be on the q-axis, this results in a maximum-torque-per-ampere (MTPA) operation.

It is known for electric machines when $L_d = L_q$, that, for a given amount of current, maximum torque can be achieved by placing the stator magnetic field leading the rotor magnetic field by exactly 90°electrical. If the magnetic field created by stator current is now lagging the rotor magnetic field, the direction of the torque is reversed. In an SPMSM, the rotor d-axis, or the direct-axis, is the axis where the maximum rotor flux-linkage is present. Therefore, by commanding current on the q-axis, which is conveniently defined to be leading the d-axis by 90°electrical, the above-mentioned principle is achieved. The d-axis current is controlled to be zero because it does not affect the torque directly, and also to avoid magnetic saturation. This can also be seen from equation (2.10).

3.1.1 Control Design

The main objective of the controller is to regulate the speed of the machine. To achieve this, a cascade control structure is implemented, where the outer loop is a speed controller and the inner loop consists of two current controllers. The two current controllers control the d-axis current and q-axis current. The reference q-axis current is calculated by the speed controller from the determined necessary torque to keep tracking the speed reference. For this control structure, the bandwidth of the outer loop should be $5 \sim 10$ times lower than the inner loop to avoid interference between the controllers. Using this knowledge, the inner loop can be simplified as a first-order system.

The control loops are designed as a continuous transfer function and then discretized transfer functions are found with similar characteristics. This is achieved by taking into consideration the delays present in the system and the sampling frequency of the system. This is called design-by-emulation.

The control parameters are designed for the worst-case scenario in terms of oscillations in the system, thus the parameters are designed under no-load conditions since applying a load will dampen the system.

The criteria for the control system was first introduced in section 1.4, but it is repeated here in table 3.1. It is not listed in the table, but of course, it is paramount that the system is stable.

Table 3.1: *Design Criteria of control loops*

	Max. Overshoot	Bandwidth	Steady-State Error
Current Loop	5%	High as possible	Zero
Speed Loop	15%	High as possible	Zero

Figure 3.1 shows the full structure of the field-oriented control.

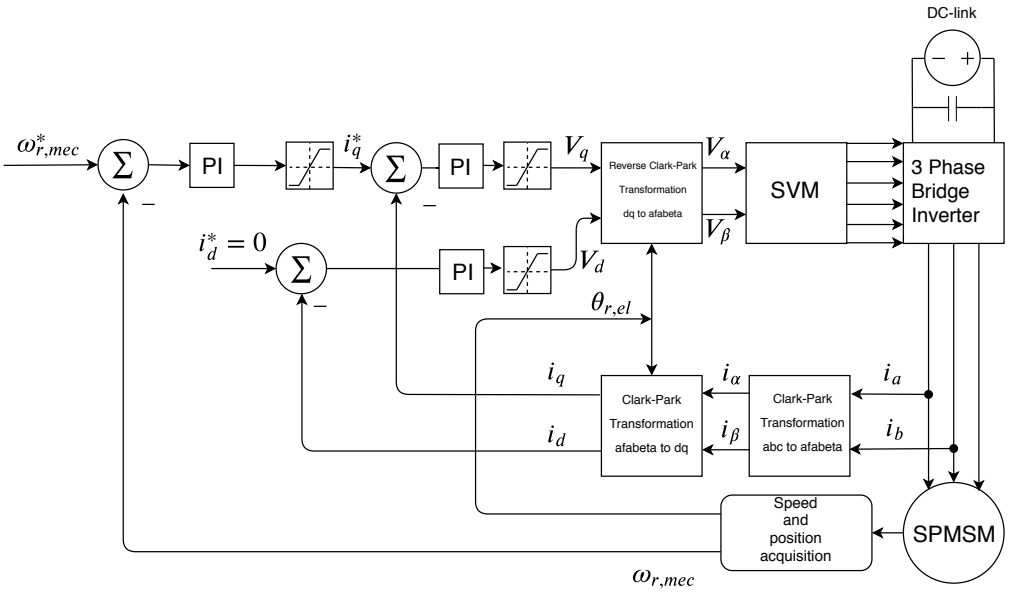

Figure 3.1: *Field Oriented Control scheme.*

3.1.2 Design of Current Controllers

The following section discusses the design process of the current control loops used in FOC [16].
The current controllers are the inner loop controlling the stator currents. To fulfill the design criteria, the system type is increased to 1 which results in no steady-state error for a step input.
The voltage equations, for both q-axis and d-axis, are used to derive the transfer functions representing the system. Transforming the voltage equations, found in equation (2.4), to Laplace domain yields:

$$i_d = \frac{v_d + \omega_r L_q i_q - s\lambda_{mpm}}{sL_d + R_s} \tag{3.1}$$

Where $s\lambda_{mpm} = 0$

$$i_q = \frac{v_q - \omega_r (L_d i_d + \lambda_{mpm})}{sL_q + R_s} \tag{3.2}$$

At this point, the system is coupled as seen in the motor voltage equations (3.1), and (3.2). The system can however be decoupled by compensating for the back-EMF disturbance. The inverse of equations (2.7) is added to the loop as shown in figures 3.2 and 3.3.

After decoupling the system, the transfer function for both q-axis and d-axis are derived as shown in equation (3.3) and equation (3.4)

$$G_d = \frac{i_d}{v_d} = \frac{1}{sL_d + R_s} \tag{3.3}$$

$$G_q = \frac{i_q}{v_q} = \frac{1}{sL_q + R_S} \tag{3.4}$$

Figures 3.2 and 3.3 show the full control loop for d-axis and q-axis current.

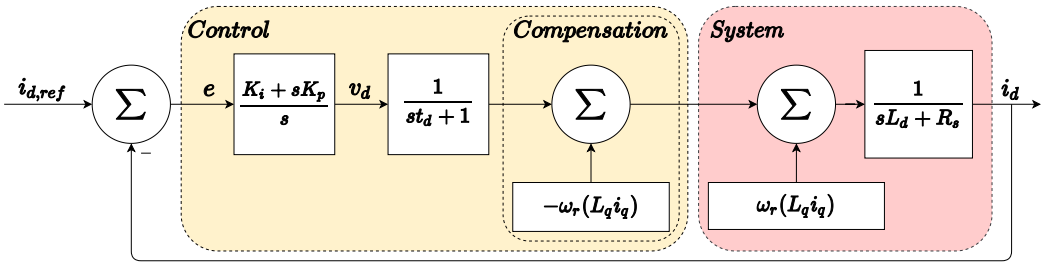

Figure 3.2: *Control loop for d-axis current with back-EMF compensation*

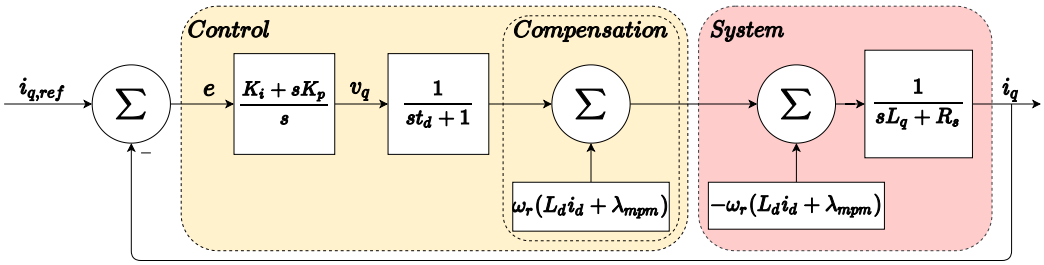

Figure 3.3: *Control loop for q-axis current with back-EMF compensation*

The resulting open-loop transfer function, including the controller and the delays, is shown in equation (3.5).

$$G_{ol}(s) = \frac{K_i + sK_p}{s} \frac{1}{st_d + 1} \frac{1}{sL_d + R_s} \tag{3.5}$$

In reality, the system is digital. This naturally means that there delays present in the system. One sampling period delay because the digital system has to process the input signals and update the output signals. Also, a 0.5 sampling period delay because the machine only sees the full voltage from the PWM modulated voltage signal after this amount of time. Overall, the time delays have a negative effect on the phase margin and in certain cases, they can make the system unstable. Therefore, it is important to include an approximation of the time-delays in the analysis of the system done in the continuous domain.

The time-delays present in a system including an SPMSM and digital controllers have been extensively examined in literature before [19], hence only the final expression for the total time delay is presented here:

$$\begin{aligned} fs &= 5kHz \\ t_s &= \frac{1}{fs} \\ t_d &= 1.5t_s \end{aligned} \tag{3.6}$$

Where the sampling frequency of the system is at fs. The delay may be approximated by a first-order system, which is effectively a low pass filter. This has the transfer function as shown in equation (3.7).

$$G_d = \frac{1}{st_d + 1} \tag{3.7}$$

Also shown above in figures 3.2 and 3.3.
The design of the control parameters was done using pole placement and SISOTOOL in Matlab with the design criteria as guidance. Because for an SPMSM, d- and q-axis inductance are the same ($L_d = L_q$), the controllers can be designed using only the d-axis. Analyzing the transfer functions, it is apparent that there is a dominant pole. The dominant pole in the system is canceled by designing the PI zero accordingly.

3.1.3 Design of Speed Controllers

The following section explains the design process of the speed control loop for the FOC [16]. A PI controller is a good choice here too because it can effectively compensate for the disturbances torque present in the system. The controller also improves the transient response of the system. It is expected that the speed loop, is much slower than the current loops. Due to this, the current loops will be

approximated by a first-order system that has the same settling time as the actual current loops.

First, the inner loop is reduced to the first-order system from the third order. The new time constant is acquired by: $\tau = t_{settling}/4$. This relation is true because, it is assumed here that an exponential term is within 2% proximity of its steady-state value after 4 time constants (τ) [20]. The transfer function then becomes equation (3.8).

$$G_{IL} = \frac{1}{\tau s + 1} \tag{3.8}$$

The next step is to derive the transfer function for the mechanical system. The mechanical equation from Newtons' second law is repeated in equation (3.9).

$$T_e = J\frac{d\omega_m}{dt} + B_m\omega_m + T_{dist} \tag{3.9}$$

Equation (3.9) is transformed into the Laplace domain where the disturbances are put to be zero, to ensure that controllers are designed the overshoot is the highest. The transfer function representing the mechanical system is formed by combining (2.10) and (3.9) resulting in the following equation:

$$\frac{\omega_m}{i_q} = \frac{K_{C2T}}{Js + B_m} \tag{3.10}$$

Where $K_{C2T} = \frac{3}{2}N_{pp}\lambda_{mpm}$. The block diagram of the speed loop is shown in figure 3.4.

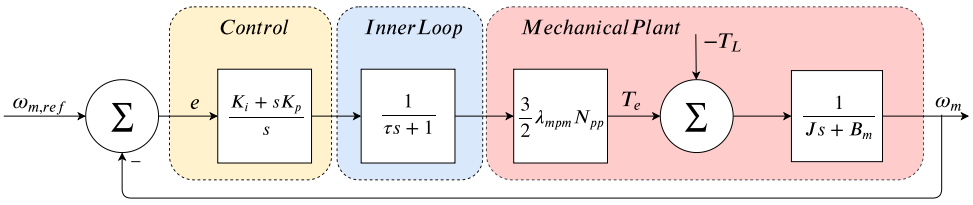

Figure 3.4: *Block diagram of the speed loop.*

The control parameters for the speed loop controller was designed similarly as the current loop controller, namely with pole placement and SISOTOOL. In figure 3.5 the open loop transfer function of the speed loop is shown where the phase margin of the system is 85.8°. This means that the system is stable. In this diagram the gain is $K_p = 1$, and oscillation is not expected in a step response.

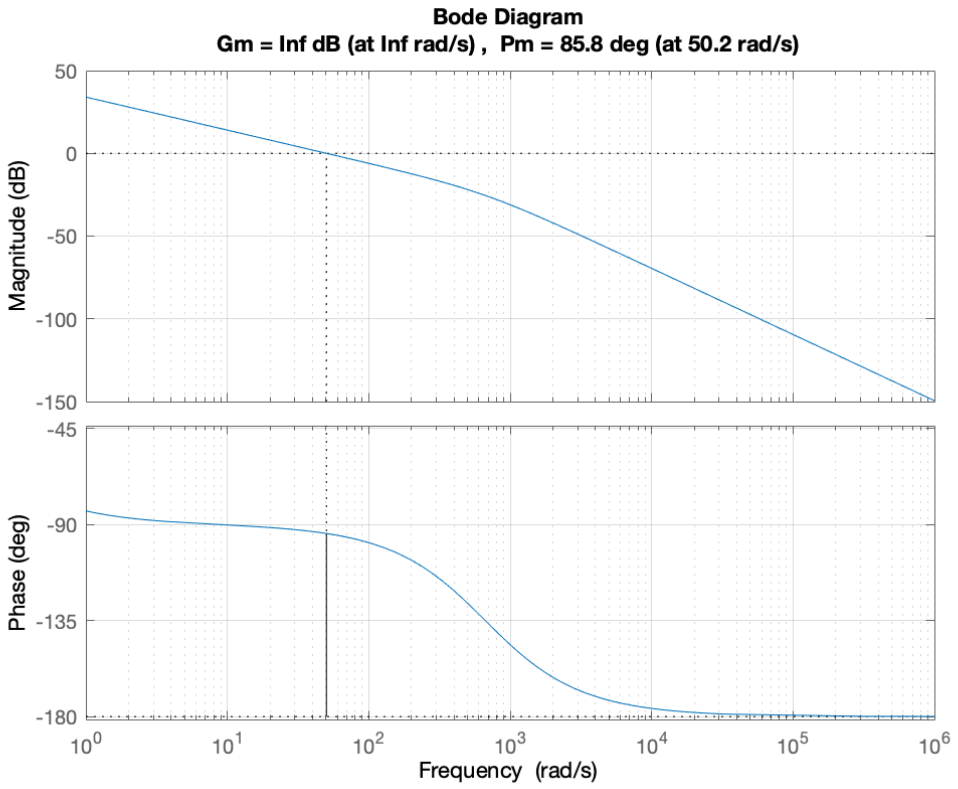

Figure 3.5: *Bode Diagram showing open loop transfer function of the speed loop.*

In figure 3.6 the bode diagram of the closed-loop transfer function of the speed and current loop is shown.

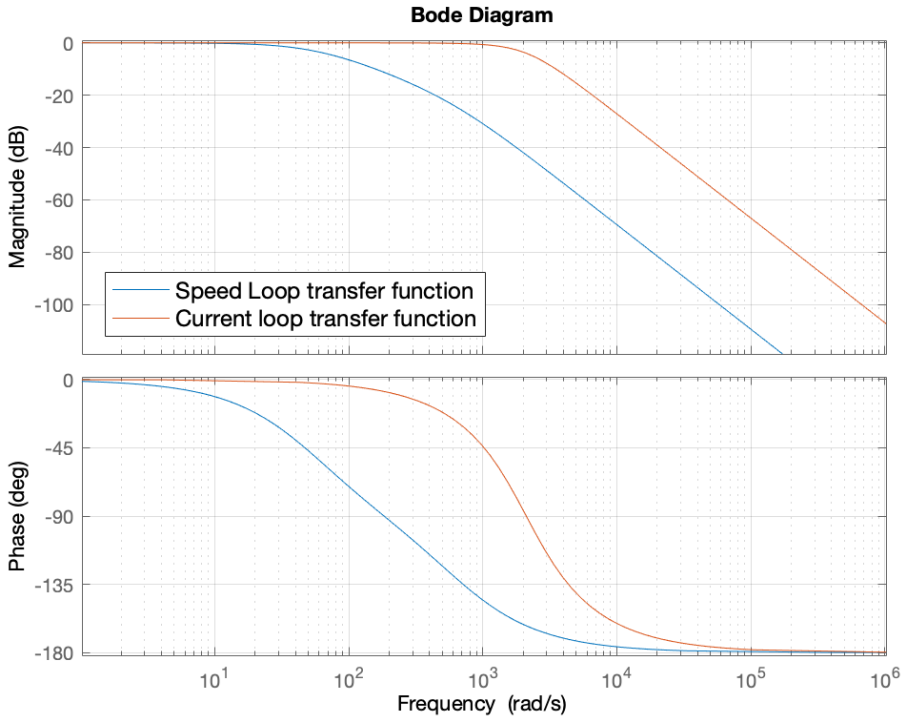

Figure 3.6: *Bode Diagram showing closed loop transfer function of the speed and current loop.*

From the figure, it is clear that the inner loop is faster than the outer. The bandwidth of the inner loop is $2400 rad/s$ and the bandwidth of the outer loop is $54 rad/s$ which means that the requirement for cascade control, is fulfilled. The control parameters will be fine-tuned in the laboratory according to the actual system response. The bandwidth of the speed controller might have to be reduced if the governing frequency of the noise in the speed signal is approximately $54 \cdot 10 = 540 rad/s$ or less. This has to be investigated later on.

Chapter 4

Coupling effect analysis

As it was mentioned earlier in chapter 3, the original MIMO, the non-linear system was first linearised, then de-coupled. The de-coupling term requires precise speed information, but due to the use of sensorless methods, this term might not be accurate enough. Therefore, it is generally advised to omit this compensation term. Gaining more insight into the coupling effects in the system is then highly desirable, because now if one input is changed, both outputs are affected.

In this chapter, one tool, the singular value decomposition (SVD) will be presented and used [21]. This method uses the state-space model of the system introduced in equation (2.13). Other methods cannot be used here, because the transfer function $G(s)$, equation (2.14), is not a square matrix. It is worth mentioning that the state-space model contains the actual rotor speed as a variable, this will cause the results to be different for different speeds. Multiple speed levels will be used, including the predefined maximum and minimum speeds.

4.1 Singular value decomposition

Eigenvalues are a poor measure of gain in a MIMO system because they can be misleading. This is due to the fact that the eigenvalues measure the gain of a system when the input vectors and the output vectors are aligned. When these vectors are not aligned, which is generally true for a MIMO system, the gain may be very different than what it is expected from the eigenvalues. Singular values of a system better represent the gain of it, because it also takes the direction of the vectors into account. It can also be used when the system matrix is not square [21]. In this section, a mathematical tool called singular value decomposition (SVD) is used to obtain these values. The definition of SVD is shown in equation (4.1) [22].

The physical meaning of this equation is a rotation, stretch, and a rotation at the end.
From a control engineering viewpoint, the singular values for MIMO systems can be interpreted as an extension of the Bode magnitude response used for SISO systems.

$$G = U\Sigma V^{\star} \tag{4.1}$$

Where G is the examined transfer function, U is a unitary matrix of output singular column vectors, Σ contains the singular values and V is a unitary matrix of input singular column vectors. Generally, only Σ is a matter of interest [21].

The benefit of using SVD is that it also gives information about the direction dependency of the input-output gain. In a coupled system, the direction of the input will change the output direction. This is apparent from the singular values as well. Evaluating the singular values at a chosen frequency will yield values between the maximum and minimum singular value. The difference is due to the different input directions. In a fully decoupled system, the maximum and minimum singular values are the same. The ratio between them can be used as a measure of the coupling effect. The closer this number is to 1, the less effect the coupling has. The maximum and minimum singular values are defined as seen in equation (4.1) [22].

$$\begin{aligned} \bar{\sigma}(G) &= \sqrt{\lambda_{max}(G^H G)} \\ \underline{\sigma}(G) &= \sqrt{\lambda_{min}(G^H G)} \end{aligned} \tag{4.2}$$

Where, λ_{max} and λ_{min} are the maximum and minimum eigenvalues of $G^H G$ respectively, and H denotes the complex conjugate transpose.

Figure 4.1 shows the plotted singular values for different reference speeds, over the frequency range of $[10^{-1}; 5 \cdot 10^4]$. The singular values are plotted for all 6 of the transfer functions are shown in equation (2.14), but for clarity, only the maximum and minimum curves are shown in each figure.

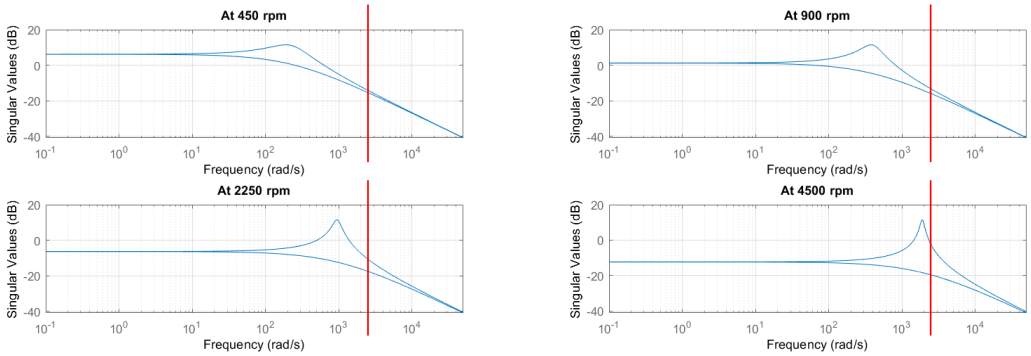

Figure 4.1: *Singular values using different reference speeds with the controller bandwidth indicated. Upper curve represents λ_{max}, lower curve represents λ_{min}*

It can be observed from figure 4.1 that the peak of the singular values gets bigger and shifts towards the right with increasing motor speeds. At maximum speed, the direction dependency is high. In the meantime, at lower speeds, the direction dependency is almost none, as in a de-coupled system.

4.2 Dynamic De-coupler for a system

This section aims to give a brief introduction to advanced control strategies for coupled systems. From the equation (2.13) it can be seen that the coupling effect would completely vanish if the A matrix had 0 terms in the off-diagonal [21]. This is shown for the given system in equation (4.3).

$$A = \begin{bmatrix} -\frac{R_s}{L} & 0 \\ 0 & -\frac{R_s}{L} \end{bmatrix} \tag{4.3}$$

This can be achieved, theoretically, by introducing a dynamic pre-compensator in the system and choosing it according to equation (4.4). It is called dynamic because it compensates for all frequencies.

$$W(s) = G(s)^{-1} \tag{4.4}$$

$$\begin{bmatrix} y_1 \\ y_2 \end{bmatrix} = G(s)W(s) \begin{bmatrix} u_1 \\ u_2 \end{bmatrix} = I \begin{bmatrix} y_1 \\ y_2 \end{bmatrix} \tag{4.5}$$

Where y_1, y_2 are the outputs, and u_1, u_2 are the inputs. This also changes the diagonal values to be 1, which results in a new system shown in equation (4.5).

However, the pre-compensator is sensitive to modeling errors because it is based on the accurate knowledge of $G(s)$. $G(s)$ is never going to be exactly the same as the real system. Still this control method could yield good performance, and therefore it is widely used, for heavily coupled systems. After compensation, the system might not be strictly proper anymore. A strictly proper system suppresses all the unwanted high-frequency dynamics, like a low-pass filter. Therefore, it is necessary to make the system strictly proper. This is done by implementing a low-pass filter with a sufficiently high order [21].

4.3 Summary of the coupling effect analysis

In the scope of this thesis, the focus is put on the lower speed range, because that is the speed range where the performance of the position and speed observers have to be improved. The coupling effect is weak in this case and it can be safely disregarded. However, in the high-speed range, the coupling effect gets stronger. Theoretically, the de-coupling terms could be switch back on when the machine is operating at high speeds, as it was shown in figure 3.2 and 3.3. This can be done due to the fact that the estimated speed signal should be accurate enough in this case and that would make the coupling effect a non-issue again. Practically, the controller regards the coupling effect a disturbance and it is assumed that it can compensate for it effectively. As a result of these, the system will be treated as a de-coupled system in the rest of the report and a pre-compensator will not be implemented.

Chapter 5

Estimators

Although every estimator discussed in this chapter uses a different approach to calculate the given states, there is one thing they all have in common: all of them are model equation based. This means that an accurate formulation of the system model is necessary, as well as, accurate identification of the model parameters.
Some of the methods are more robust against uncertainties in the system model than others. This is also a crucial point of the analysis of the estimators, because, generally speaking, the higher tolerance allowed in the model parameter identification, the better.

5.1 Estimator criteria

The foundation of FOC is the dq-reference frame transformation, which linearizes the system. This enables the control engineer to use simple PI controllers to regulate both the current and the speed. The reference frame transformation requires an accurate position signal. Therefore, the most important state to estimate is the position.

A large position error will also result in reduced torque output, and therefore in reduced power of the motor. This is due to the full i_q current from the VSI not being be available, some of it will be i_d current. This is visualized in figure 5.1. The load torque loss is dependent on the cosine of the position error angle. This also means that the operation of the motor would also not be as efficient as it could be. This has to be avoided as much as possible.

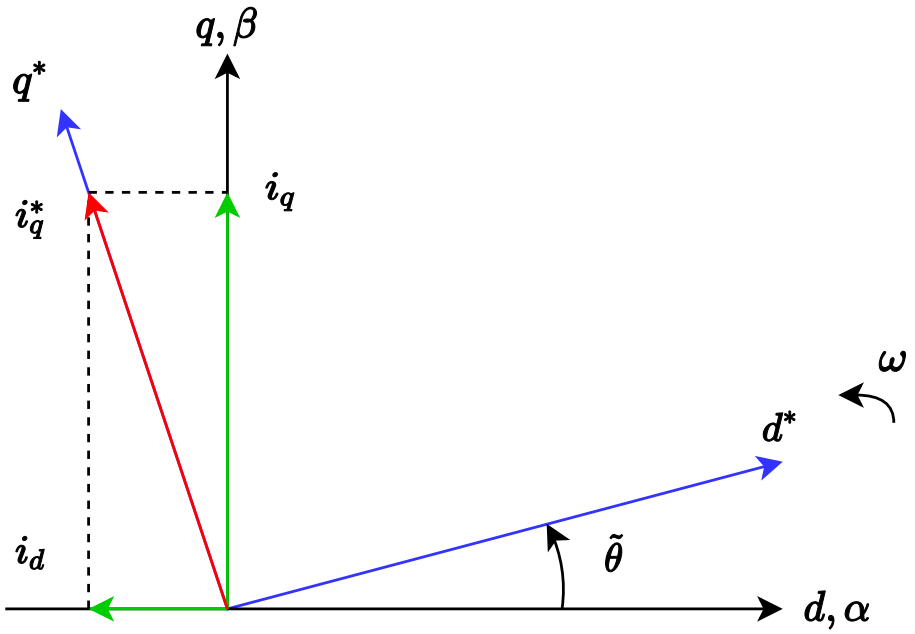

Figure 5.1: *The effect of the angle error ($\tilde{\theta}$) on the actual stator i_q current*

5.2 The foundation of estimators

It is necessary to transform the stator voltage equations, previously expressed in dq-reference frame, to the $\alpha\beta$-reference frame. In the $\alpha\beta$-reference frame, the rotating speed of the reference is zero because the reference-frame is stationary now [23]. This is beneficial because the position (θ) and the speed (ω_r) will both appear in the back-EMF equations. The new voltage equations, in vector form, can be seen in equation (5.1) and (5.2).

$$\vec{v}_{\alpha\beta} = R\vec{i}_{\alpha\beta} + p\vec{\lambda}_{\alpha\beta} \tag{5.1}$$

$$\vec{\lambda}_{\alpha\beta} = (L_d i_d + \lambda_{mpm} + jL_q i_q)e^{j\theta_r} \tag{5.2}$$

As it was mentioned, the position appears in the back-EMF components, as shown in equation (5.3).

$$\begin{aligned} e_\alpha &= -\lambda_{mpm}\omega_{r,el}sin\theta_r \\ e_\beta &= \lambda_{mpm}\omega_{r,el}cos\theta_r \end{aligned} \tag{5.3}$$

From the α, β components of the back-EMF, shown in equations (5.3), θ_r can be found by equation (5.4). This is also illustrated in figure 5.2 [16].

$$\hat{\theta} = tan^{-1}\left(\frac{-\hat{e_\alpha}}{\hat{e_\beta}}\right) \tag{5.4}$$

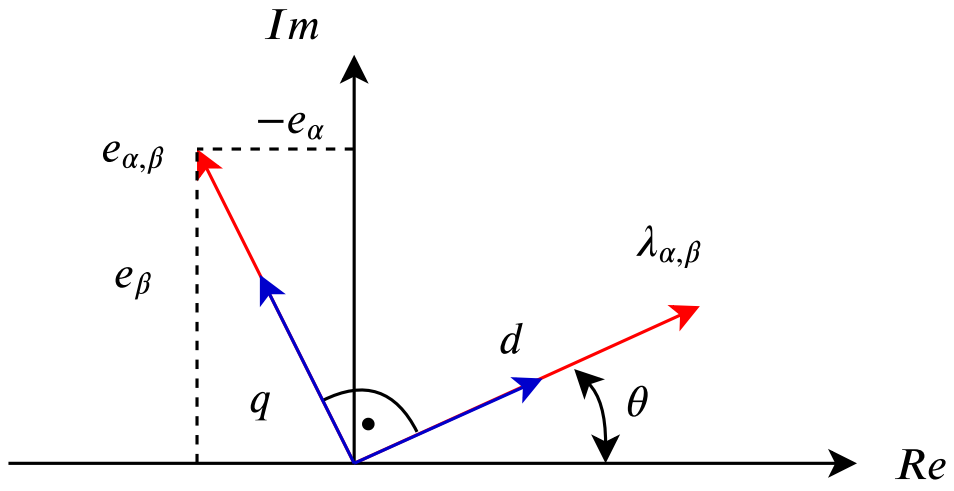

Figure 5.2: *The relation between $e_{\alpha,\beta}$ and $\lambda_{\alpha,\beta}$. Also, the relation between the vectors and the rotor position θ.*

The position can also be calculated from estimated flux-linkage because the relationship between the flux-linkage and the back-EMF voltage, under the assumption that the stator resistance is neglectable, is the following:

$$\vec{\lambda}_{\alpha,\beta} = \int \vec{v}_{\alpha,\beta}dt \tag{5.5}$$

In the graphical representation, integration or differentiation can be interpreted as a 90°rotation between the vectors. The difference between the integration and differentiation is the direction of the rotation.

Combining the equations in (5.3) a dense formula (5.6) can be acquired for the rotor speed (ω_r) estimation, but care has to be taken when using the equation. It

is very sensitive to the λ_{mpm} parameter, which acts as a scaling factor here. In case, an accurate λ_{mpm} is obtainable by measuring it online or offline, this formula can give a good speed signal compared to methods that use certain mathematical tools to differentiate the position.

$$\mid \omega_r \mid = \frac{1}{\lambda_{mpm}} \sqrt{e_\alpha^2 + e_\beta^2} \tag{5.6}$$

In other cases, where λ_{mpm} has uncertainties, it is easier to obtain the speed by differentiating the position and filtering the signal, as it is shown in figure 5.3 or by using a Phase-locked loop structure, as it is shown in figure 5.4 [24].

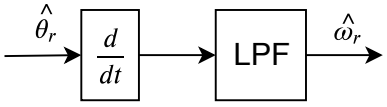

Figure 5.3: *General structure of differentiating a signal*

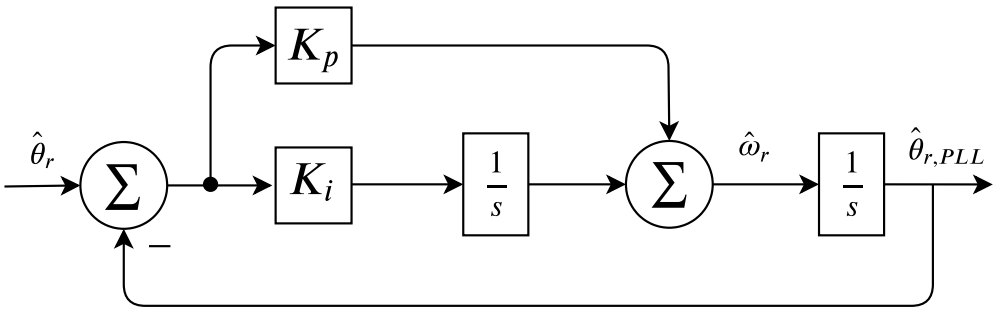

Figure 5.4: *Structure of the phase-locked loop*

The PLL structure was analysed in details in report [16]. The error signal is formulated such as:

$$\tilde{\theta}_r = \hat{\theta}_r - \hat{\theta}_{r,PLL} \tag{5.7}$$

Then, the open-loop transfer function is presented in equation (5.8).

$$\hat{\theta}_{r,PLL} = \tilde{\theta}_r(K_p + K_i\frac{1}{s})\frac{1}{s} \tag{5.8}$$

Closing the loop yields the expression shown in equation (5.9).

$$H_{PLL,\theta}(s) = \frac{\hat{\theta}_{r,PLL}}{\hat{\theta}_r} = \frac{K_p s + K_i}{s^2 + K_p s + K_i} \tag{5.9}$$

This structure can be used as a differentiator and as a filter as well.

5.3 Structure of the system with the observers

The modified structure of the system, now including the observers, is presented in figure 5.5. All observers are realized in the α, β-reference frame. Also the observers are using the directly measured current ($i_{\alpha,\beta}$), and indirectly measured voltage ($v_{a,b,c}$). In some cases, the reference speed (ω_{ref}) is needed for the observer gain calculations. An observer is chosen by changing out the block with the name: observer. In all cases, further filtering of the estimated signals is necessary. Finally, the estimated position ($\hat{\theta}_r$) is fed back to the reference frame transformations, and the estimated speed ($\hat{\omega}_r$) is fed back to the speed controller.

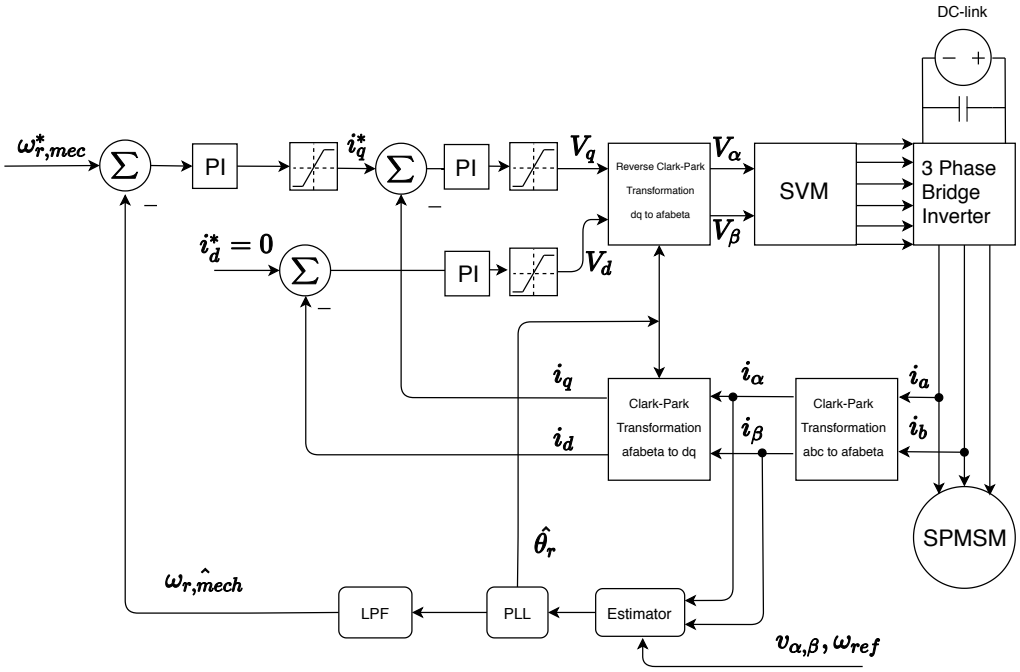

Figure 5.5: *Structure of control system with a generalized estimator included*

5.4 Closed-loop flux observer

A popular way of estimating the speed and rotor position is to observe the flux-linkage vector expressed in α, β-reference frame. Therefore this method observers the $\lambda_{\alpha,\beta}$ state as shown in figure 5.2. This is based on the voltage model of the system. Open-loop approaches are easy to realize but are usually not very accurate due to the integrator drift phenomenon. This might be compensated by removing the average value of the flux-linkage every cycle. This was first presented in [11].

However, a more efficient way to tackle this problem is to use a closed-loop observer [12]. The observer calculates the flux-linkage through a PI controller, which uses two open-loop models. One model is based on the current model, the other is based on the voltage model. Due to the current measurements being much more accurate than the voltage ones at low speed, the current model is more influential at low speeds and the accuracy of current model is influenced by the motor parameters. On the other hand, at medium to high speeds, the voltage model will give better results because it is not significantly affected by the inverter voltage errors anymore. The structure of the observer is shown in figure 5.6. Using this struc-

ture, it is expected that the stability and robustness of the observer is increased compared to open-loop methods [12].

Starting with the voltage model, the system equation expressed in α, β-reference frame is shown in equation (5.10).

$$\begin{aligned} v_\alpha &= R_{pm} i_\alpha + \frac{d}{dt}\lambda_\alpha \\ v_\beta &= R_{pm} i_\beta + \frac{d}{dt}\lambda_\beta \end{aligned} \tag{5.10}$$

Rearranging the expression yields the following:

$$\begin{aligned} \lambda_\alpha &= \int (v_\alpha - R_{pm} i_\alpha) dt \\ \lambda_\beta &= \int (v_\beta - R_{pm} i_\beta) dt \end{aligned} \tag{5.11}$$

The other model is established in equation (5.12) and equation (5.13). This requires the transformation from α, β-reference frame to dq-reference frame, and after the calculations, back to α, β-reference frame.

$$\begin{aligned} \lambda_d^* &= L_d i_d + \lambda_{mpm} \\ \lambda_\alpha^* &= (L_d i_d + \lambda_{mpm}) cos\theta - L_q i_q sin\theta \end{aligned} \tag{5.12}$$

$$\begin{aligned} \lambda_q^* &= L_q i_q \\ \lambda_\beta^* &= (L_d i_d + \lambda_{mpm}) sin\theta + (L_q i_q) cos\theta \end{aligned} \tag{5.13}$$

The equations (5.12) and (5.13) are used as a reference in the compensation block, Using this, an error signal is formed and then fed to a PI controller. The loop is then closed as shown in figure 5.6. This figure shows the structure of the closed-loop flux observer. The system is considered stable if all the individual parts of the system are stable. This requirement is fulfilled if the PI controller only has right-hand plane poles (RHP). The compensator can be tuned by changing the bandwidth of the PI regulator.

Using the above introduced expressions, the estimated rotor position may be calculated utilizing the 'tan2' function, as shown in equation (5.14)

$$\hat{\theta}_r = tan2^{-1} \frac{\hat{\lambda_\beta} - L_{pm} i_\beta}{\hat{\lambda_\alpha} - L_{pm} i_\alpha} \tag{5.14}$$

Furthermore, the rotor speed (ω_r) may be acquired by a PLL. The PLL can also be used to filter the signals.

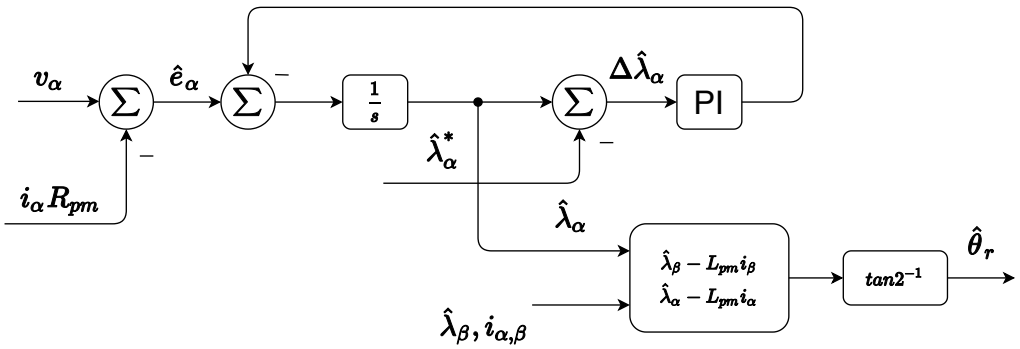

Figure 5.6: *Structure of closed-loop flux observer*

5.5 First-order sliding mode observer

Sliding mode observers are non-linear observers with high capability of disturbance rejection and low sensitivity against model parameter uncertainties [1]. This is achieved by constructing a sliding surface in the state space. The observer law is made discontinuous across the surface by utilizing the sign function. Thus, the reason why the controller has the above-mentioned properties. Utilizing the sign function results in chattering in the observer output signal, which is undesirable because the estimated speed signal is fed back to the speed PI control loop. When a pure sign function is used, the bandwidth of the chattering is the same as the sampling frequency. Therefore, the bandwidth of the chattering is much higher than the bandwidth of the speed PI control loop, which makes the speed PI control loop to act as a low-pass filter. The overall system performance is reduced, hence the attenuation of the chattering is one of the most important tasks during the design of sliding mode observers. The attenuation can be done by substituting the sign function with an approximation of it, for instance with the sigmoid function or with the saturation function. This introduces a boundary layer around the sliding surface. The benefit of it is a smoother observer output signal, the drawbacks of it are loss of robustness and accuracy [25].

The sliding mode observer is machine model-based. The starting point of every design is the slightly rewritten voltage equations expressed in the $\alpha\beta$ reference frame.

$$\begin{aligned} \frac{di_\alpha}{dt} &= fi_\alpha + g(v_\alpha - e_\alpha) \\ \frac{di_\beta}{dt} &= fi_\beta + g(v_\beta - e_\beta) \end{aligned} \tag{5.15}$$

Where $f = -\frac{R_s}{L_s}$ and $g = \frac{1}{L_s}$. The resistance and inductances are time-invariant [16], since with increasing temperature, the resistance increases, and in the meantime, the inductance decreases. However, this effect is assumed to be very minor and will be neglected.

The sliding variable, which characterizes the observer, is chosen as presented in equation (5.16). Since the system is first-order, the sliding variable directly gives the estimation error.

$$\boldsymbol{\sigma} = (\frac{d}{dt} + \lambda)^{n-1}\tilde{\boldsymbol{x}} = \tilde{\boldsymbol{i_s}} = \hat{\boldsymbol{i_s}} - \boldsymbol{i_s} \tag{5.16}$$

Where n is the order of the system, $\boldsymbol{\sigma} = [\sigma_\alpha, \sigma_\beta]$, λ is a strictly positive observer variable, and $\tilde{\boldsymbol{x}} = \tilde{\boldsymbol{i}}$ is the error in the estimated stator current [1].

Next, the observer law is formulated, such as [26]:

$$\begin{aligned} \frac{d\hat{i}_\alpha}{dt} &= f\hat{i}_\alpha + g(v_\alpha - ksgn(\sigma_\alpha)) \\ \frac{d\hat{i}_\beta}{dt} &= f\hat{i}_\beta + g(v_\beta - ksgn(\sigma_\beta)) \end{aligned} \tag{5.17}$$

The main goal is to use the measured states for the calculations and observe the rest of the system equation using the sliding mode observer.
By driving the error between the measured and the estimated currents to zero, the unknown part of the equation (last two terms in equation (5.17)) is well estimated. This part mainly contains back-EMF terms, and also some unmodelled system dynamics. It is assumed that the back-EMF terms are dominant, therefore the rotor position can be calculated from them with good precision using equation (5.4).

Stability of the observer

Choosing the observer gain is a crucial part of the design because of too high gain results in high chattering action, and too low gain results in an unstable observer, consequently in an unstable system. A simple analysis may be conducted by looking at the dynamics of the sliding variable, equation (5.16) [27].

$$\begin{aligned} \frac{d}{dt}\sigma_\alpha &= \frac{d}{dt}\tilde{i_\alpha} - \frac{d}{dt}i_\alpha = f\sigma_\alpha + ge_\alpha - gksgn(\sigma_\alpha) \\ \frac{d}{dt}\sigma_\beta &= \frac{d}{dt}\tilde{i_\beta} - \frac{d}{dt}i_\beta = f\sigma_\beta + ge_\beta - gksgn(\sigma_\beta) \end{aligned} \tag{5.18}$$

In case, the observer gain k is large enough, the sign of $\sigma_\alpha, \sigma_\beta$ will be different than the sign of $\frac{d}{dt}\sigma_\alpha, \frac{d}{dt}\sigma_\beta$. As a result, $\sigma_\alpha \to 0, \sigma_\beta \to 0$ and once the sliding mode occurs, $\sigma_\alpha = 0, \sigma_\beta = 0$.

Under the assumption that the first term containing σ_α is small enough in equation (5.18), it can be seen that the gain has to be $k > max(\mid e_\alpha \mid, \mid e_\beta \mid)$, to satisfy the above stated requirement.

A detailed proof, which utilizes the Lyapunov theory, was shown in [16]. The basis of the Lyapunov theory is the same as in the method above. The final conclusion of the aforementioned report is the same, the observer gain has to be chosen such as $k > max(\mid e_\alpha \mid, \mid e_\beta \mid)$. This makes the given equilibrium point, defined by the Lyapunov theory, globally asymptotically stable, which in practice means that the error will be driven to zero in finite time. This is an important quality of any observer.

The observer gain might be reduced at lower speeds, because e_α, e_β are a function of the speed. The outcome of it is lower observer activity which reduces the chattering. By making the gain change based on the reference speed, and also adding a safety margin term to it to compensate for transient effects, the gain can be changed linearly. The final equation for the observer gain is presented in equation (5.19) [16].

$$k = \omega_{ref}\lambda_{mpm} + k_{add} \tag{5.19}$$

Chattering attenuation

There is chattering present in the observer output signal. This is because the observer is discretized. The chattering is attenuated by implementing the sigmoid function [26], shown in equation (5.20). This will make the observer be a quasi-sliding mode observer and the sliding variable will converge to a band around the sliding surface, rather than to the surface itself. This reduces the chattering significantly, however, it can be seen in the experimental results in [16] that even then, the position ($\hat{\theta}_r$) has to be filtered by multiple PLLs, and the speed ($\hat{\omega}_r$) also has to be filtered by high-order low-pass filters. The cut-off frequency of the filters has to be chosen according to the bandwidth of the given controller.

$$F = \frac{\sigma}{\mid \sigma \mid + \frac{\phi}{100}} \tag{5.20}$$

After filtering, it was observed that the estimated speed and position signals are satisfactory and the overall system performance is good, but oscillation can be observed in the estimated signals. The oscillation frequency is equal to the fundamental electrical frequency. This phenomenon is further investigated in section 5.8.

5.6 Second-order sliding mode observer

A system using a traditional, first-order sliding mode observer needs multiple filters to deal with the chattering problem present in the observer output signal, as it was mentioned in section 5.5. This increases the overall complexity of the system [28].

Implementing a higher-order sliding mode observer, for instance, a super twisting observer (STO), instead, is a popular way of reducing the number of filters needed in a system [28]. The order of the observer is increased by introducing new terms that are then integrated into the observer law. The main characteristic of a higher-order sliding mode observer is that the observer signal is now made continuous. Furthermore, it allows for a sliding mode on $\sigma = \dot{\sigma} = 0$ using only σ [25]. In this case, σ is defined the same as for the first-order SMO, $\boldsymbol{\sigma} = \hat{\boldsymbol{i}}_{\boldsymbol{s}} - \boldsymbol{i}_{\boldsymbol{s}}$, due to the fact that the system remained the same.

Using the same starting point for the design, as for the first-order sliding mode observer, the new observer law is formulated in equation (5.21).

$$\begin{aligned} \frac{d\hat{i}_\alpha}{dt} &= f\hat{i}_\alpha + gu_\alpha + gk_1\sqrt{\mid \sigma_\alpha \mid}sign(\sigma_\alpha) + gw_\alpha \\ \frac{d\hat{i}_\beta}{dt} &= f\hat{i}_\beta + gu_\beta + gk_1\sqrt{\mid \sigma_\beta \mid}sign(\sigma_\beta) + gw_\beta \end{aligned} \tag{5.21}$$

$$\begin{aligned} \dot{w}_\alpha &= k_2 sign(\sigma_\alpha) \\ \dot{w}_\beta &= k_2 sign(\sigma_\beta) \end{aligned} \tag{5.22}$$

Where $f = -\frac{R_s}{L_s}, g = \frac{1}{L_s}$, and the errors, $\sigma_\alpha = \hat{i}_\alpha - i_\alpha, \sigma_\beta = \hat{i}_\beta - i_\beta$.

The first observer gain (k_1) corresponds to the dynamic performance of the observer, and the second gain (k_2) is responsible for smoothing out the output signal. The smoothing is done by integration of the sign function. Before looking at the

proof of the stability, it can be seen that k_2 has to be larger than k_1 to attenuate the chattering, but the ratio cannot be too high because that would reduce the overall performance of the system in transients.
The two terms with the observer gains in equation (5.21) directly give the estimated back-EMF signal, as presented in equation (5.23).

$$\begin{aligned} \hat{e}_\alpha &= -k_1\sqrt{\mid \sigma_\alpha \mid}sign(\sigma_\alpha) - \int \dot{w}_\alpha dt \\ \hat{e}_\alpha &= -k_1\sqrt{\mid \sigma_\beta \mid}sign(\sigma_\beta) - \int \dot{w}_\beta dt \end{aligned} \tag{5.23}$$

Stability of the observer

It can be noticed that in an SPMSM, the perturbation terms are the following:

$$\begin{aligned} \rho_{1,\alpha} &= fi_\alpha + gu_\alpha \\ \rho_{1,\beta} &= fi_\beta + gu_\beta \end{aligned} \tag{5.24}$$

In other words, the perturbation terms are the terms present in equation (5.21) but not in equation (5.23).
The stability of the observer is shown in details in Appendix C. For this system, it is a fair assumption that the first perturbation term is globally bounded, such as: $\mid \rho_1 \mid \leq \delta_1\sqrt{\mid max(e_\alpha, e_\beta) \mid}$, and there is no second term present in this system, hence $\rho_2 = 0$. If this is true, the expressions for the gains can be simplified, as show in equation (5.25).

$$\begin{aligned} k_1 &> 2\delta_1 \\ k_2 &> k_1\frac{5\delta_1 k_1 + 4\delta_1^2}{2(k_1 - 2\delta_1)} \end{aligned} \tag{5.25}$$

Where δ_1 is a positive constant. From the above equation (5.25), it can be seen that many gain combinations will result in a stable system because there is not an explicit equation or an upper constraint defined for the gains. It is worth repeating it here, that higher observer gains will result in higher chattering, so a practical upper bound may be set. This formula implies the necessity of experimental tuning of the observer.

Another approach to finding the observer gains is presented in [25]. This is an explicit strategy for choosing the parameters. The gains are chosen based on the measure of the perturbation in the system. The condition, that the perturbations have to be bounded, must be true again.

$$\begin{aligned} k_1 &= 1.5\sqrt{max(\rho_{1,\alpha}, \rho_{1,\beta})}, \\ k_2 &= 1.1max(\rho_{1,\alpha}, \rho_{1,\beta}) \end{aligned} \tag{5.26}$$

Equation (5.26) defines a nonlinear relation between the gains. The detailed proof for this case is not shown in this report, but it can be found in [25].

The approach presented above is generally not used in SPMSM applications because the gains are chosen non-linearly. It can be expected, from the first-order sliding mode observer, that using static observer gains is not feasible here, because the perturbation terms, equation (5.24), can change in a wide range.

As a conclusion, the observer gains will be tuned later in both simulation and the laboratory according to a linear law, based on the reference speed, or they will be changed using a look-up table, based on experimental results.

5.7 First-order sliding mode observer in *dq*-reference frame

Another option is to design the sliding mode observer in the estimated dq-reference frame denoted as dq^* [29]. The advantage of this is that in dq-reference frame the current, voltage, and back-EMF signals are DC signals. However, the position cannot be directly acquired from the estimated back-EMF signals, only the position error ($\tilde{\theta}$). This new state, position error, will become the focus of this method. Using a PLL, the rotor position and speed can be calculated in the next steps.
Due to the signals being DC, it can be assumed that a simpler filtering structure will be sufficient and 0 phase lag will be added. This will be verified later on in the report.

As a first step, the voltage equations expressed in dq-reference frame are transformed into dq^* reference frame. Using the position error angle, as it is shown in figure 5.7, the transformation is done by using simple 2 dimensional projections [29].

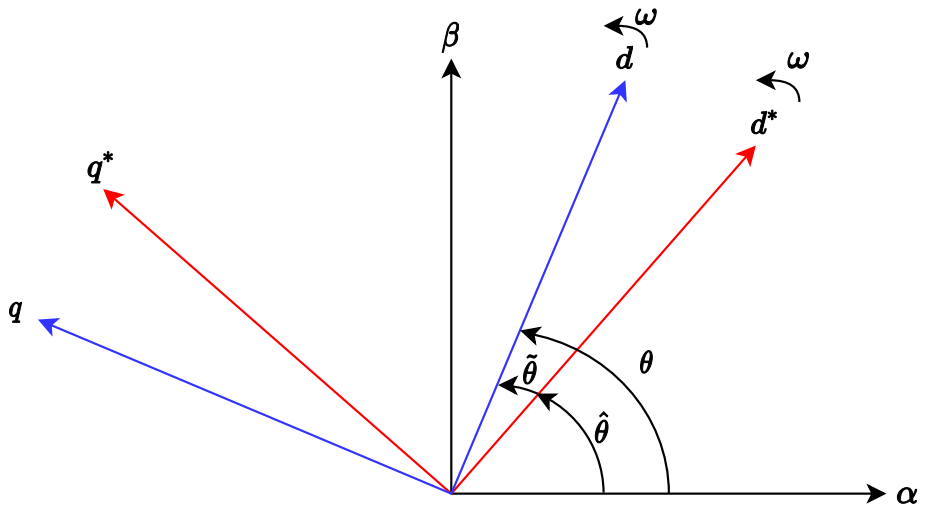

Figure 5.7: *The definition of the dq^* reference frame*

The transformations are done by utilizing the definition of the *sin* and *cos* functions. This is summarized in equation (5.27).

$$T(\tilde{\theta}) = \begin{bmatrix} cos(\tilde{\theta}) & -sin(\tilde{\theta}) \\ sin(\tilde{\theta}) & cos(\tilde{\theta}) \end{bmatrix} \tag{5.27}$$

And with the supporting matrix (J_m) seen in equation (5.28).

$$J_m = \begin{bmatrix} 0 & -1 \\ 1 & 0 \end{bmatrix} \tag{5.28}$$

First, the voltage is transformed from dq to dq^*.

$$v_{dq^*} = \begin{bmatrix} v_{d^*} \\ v_{q^*} \end{bmatrix} = T(\tilde{\theta}) \begin{bmatrix} v_d \\ v_q \end{bmatrix} = \begin{bmatrix} v_d cos(\tilde{\theta}) - v_q sin(\tilde{\theta}) \\ v_d sin(\tilde{\theta}) + v_q cos(\tilde{\theta}) \end{bmatrix} \tag{5.29}$$

This means that even if we only have d component in the voltage vector, in the dq^*-reference frame a q^* component will also appear. The resulting rotor flux-linkage in dq^* is the following :

$$\lambda_{mpm,dq^*} = \begin{bmatrix} \lambda_{mpm,d^*} \\ \lambda_{mpm,q^*} \end{bmatrix} = \lambda_{mpm} \begin{bmatrix} cos(\tilde{\theta}) \\ sin(\tilde{\theta}) \end{bmatrix} \tag{5.30}$$

Next, the rest of the system states are transformed in equations (5.31) and (5.32).

$$i_{dq^*} = \begin{bmatrix} i_{d^*} \\ i_{q^*} \end{bmatrix} = T(\tilde{\theta}) \begin{bmatrix} i_d \\ i_q \end{bmatrix} = \begin{bmatrix} i_d cos(\tilde{\theta}) - i_q sin(\tilde{\theta}) \\ i_d sin(\tilde{\theta}) + i_q cos(\tilde{\theta}) \end{bmatrix} \tag{5.31}$$

$$\lambda_{dq^*} = \begin{bmatrix} \lambda_{d^*} \\ \lambda_{q^*} \end{bmatrix} = L_{pm} T(\tilde{\theta}) \begin{bmatrix} i_d \\ i_q \end{bmatrix} + \lambda_{mpm} T(\tilde{\theta}) \begin{bmatrix} 1 \\ 0 \end{bmatrix} = L_{pm} \begin{bmatrix} i_{d^*} \\ i_{q^*} \end{bmatrix} + \begin{bmatrix} \lambda_{mpm,d^*} \\ \lambda_{mpm,q^*} \end{bmatrix} \tag{5.32}$$

As the last step, the derivative of the flux-linkages (λ_{dq^*}) are calculated. This can be seen in equation (5.33).

$$\dot{\lambda}_{dq^*} = \begin{bmatrix} \dot{\lambda}_{d^*} \\ \dot{\lambda}_{q^*} \end{bmatrix} = L_{pm} \begin{bmatrix} \dot{i}_{d^*} \\ \dot{i}_{q^*} \end{bmatrix} + \begin{bmatrix} \dot{\lambda}_{mpm,d^*} \\ \dot{\lambda}_{mpm,q^*} \end{bmatrix} \tag{5.33}$$

Now, let's calculate the last unknown term in the voltage equation, $\dot{\lambda}_{mpm,dq^*}$, using equation (5.34). A term based on saliency is ignored because the given system does not have saliency.

$$\dot{\lambda}_{mpm,dq^*} = \begin{bmatrix} \dot{\lambda}_{mpm,d^*} \\ \dot{\lambda}_{mpm,q^*} \end{bmatrix} = \lambda_{mpm} \dot{\tilde{\theta}} \begin{bmatrix} -sin(\tilde{\theta}) \\ cos(\tilde{\theta}) \end{bmatrix} = \lambda_{mpm} \dot{\tilde{\theta}} J_m \begin{bmatrix} cos(\tilde{\theta}) \\ sin(\tilde{\theta}) \end{bmatrix} \tag{5.34}$$

The first-order differential equation of the system is repeated here in equation (5.35).

$$\begin{aligned} \frac{di_d}{dt} &= f i_d + g v_d + \omega_r i_q \\ \frac{di_q}{dt} &= f i_q + g v_q - \omega_r i_d - g \omega_r \lambda_{mpm} \end{aligned} \tag{5.35}$$

Finally, the total system equations, now transformed into dq^*-reference frame, are shown in equation (5.36). Here, the last terms are the back-EMF terms.

$$\begin{aligned} \frac{di_{d^*}}{dt} &= f i_{d^*} + g v_{d^*} + \omega_r i_{q^*} + g \omega_r \lambda_{mpm} sin(\tilde{\theta}) \\ \frac{di_{q^*}}{dt} &= f i_{q^*} + g v_{q^*} - \omega_r i_{d^*} - g \omega_r \lambda_{mpm} cos(\tilde{\theta}) \end{aligned} \tag{5.36}$$

The observer law is then derived similarly as it was done in section 5.5.

$$\begin{aligned} \frac{d\hat{i}_{d^*}}{dt} &= fi_{d^*} + gv_{d^*} + \hat{\omega}_r i_{q^*} - gksgn(\sigma_{d^*}) \\ \frac{d\hat{i}_{q^*}}{dt} &= fi_{q^*} + gv_{q^*} - \hat{\omega}_r i_{d^*} - gksgn(\sigma_{q^*}) \end{aligned} \tag{5.37}$$

Where $f = -\frac{R_s}{L_s}$, $g = \frac{1}{L_s}$, and $\sigma_{d^*}, \sigma_{q^*}$ are sliding variables for the first-order system and are defined in equation (5.39).

$$\sigma_{d^*} = \tilde{i}_{d^*} = i_{d^*} - \hat{i}_{d^*} \tag{5.38}$$

$$\sigma_{q^*} = \tilde{i}_{q^*} = i_{q^*} - \hat{i}_{q^*} \tag{5.39}$$

It is assumed that the controller can perfectly follow the reference, therefore $\hat{\omega} = \omega_{ref}$. The resistance and inductance are also assumed to be time-invariant [16]. In the next section, the stability of the observer is proved.

Stability of the observer

A detailed stability proof is presented now. The stability of the sliding mode observer is proven by using the Lyapunov stability theory. This will also determine how to select the observer gains.
The chosen Lyapunov candidate function is Positive-definite (P.D.), radially unbounded and shown in equation (5.40) [25].

$$\boldsymbol{V}(\boldsymbol{\sigma}) = \frac{1}{2}\boldsymbol{\sigma}^T\boldsymbol{\sigma} = \frac{1}{2}(\tilde{i}_{d^*}^2 + \tilde{i}_{q^*}^2) \tag{5.40}$$

Where $\boldsymbol{\sigma} = [\sigma_{d^*}, \sigma_{q^*}]$.

In order to prove stability of the equilibrium the time derivative, $\dot{\boldsymbol{V}}$, shown in equation (5.41), needs to be at least Negative-semi definite (N.S.D.). If however, the time derivative,$\dot{\boldsymbol{V}}$, is Negative-definite (N.D) the system is also globally asymptotically stable [1].

$$\dot{\boldsymbol{V}}(\boldsymbol{\sigma}) = \sigma_{d^*}\dot{\sigma}_{d^*} + \sigma_{q^*}\dot{\sigma}_{q^*} \tag{5.41}$$

The derivative is calculated by subtracting equations (5.36) and (5.37) which yields, for the estimated d-axis:

$$\begin{aligned} \dot{\sigma}_{d^*} = \dot{i}_{d^*} - \dot{\hat{i}}_{d^*} &= fi_{d^*} + gv_{d^*} + \hat{\omega}_r i_{q^*} + g\omega_r\lambda_{mpm}sin(\tilde{\theta}) \\ &\quad - f\hat{i}_{d^*} + gv_{d^*} + \hat{\omega}_r\hat{i}_{q^*} - gksgn(\sigma_{d^*}) \\ &= f\sigma_{d^*} + g(\omega_r\lambda_{mpm}sin(\tilde{\theta}) - ksgn(\sigma_{d^*})) + \hat{\omega}_r\sigma_{q^*} \end{aligned} \tag{5.42}$$

And for the estimated q-axis:

$$\begin{aligned}\dot{\sigma}_{q^*} = \dot{i}_{q^*} - \dot{\hat{i}}_{q^*} &= f i_{q^*} + g v_{q^*} - \hat{\omega}_r i_{d^*} - g\omega_r \lambda_{mpm} cos(\tilde{\theta}) \\ &\quad - f\hat{i}_{q^*} + g v_{q^*} - \hat{\omega}_r \hat{i_{d^*}} - gksgn(\sigma_{q^*}) \\ &= f\sigma_{q^*} - g(\omega_r \lambda_{mpm} cos(\tilde{\theta}) + ksgn(\sigma_{q^*})) - \hat{\omega}_r \sigma_{d^*} \end{aligned} \tag{5.43}$$

These two equation above are then substituted into equation (5.41), which yields:

$$\begin{aligned}\dot{\boldsymbol{V}}(\boldsymbol{\sigma}) &= \sigma_{d^*}(f\sigma_{d^*} + g(\omega_r \lambda_{mpm} sin(\tilde{\theta}) - ksgn(\sigma_{d^*})) + \hat{\omega}_r \sigma_{q^*}) \\ &\quad + \sigma_{q^*}(f\sigma_{q^*} - g(\omega_r \lambda_{mpm} cos(\tilde{\theta}) + ksgn(\sigma_{q^*})) - \hat{\omega}_r \sigma_{d^*}) \\ &= f(\sigma_{d^*}^2 + \sigma_{q^*}^2) + g(\sigma_{d^*}\omega_r \lambda_{mpm} sin(\tilde{\theta}) - k\sigma_{d^*} sgn(\sigma_{d^*})) \\ &\quad + g(-\sigma_{q^*}\omega_r \lambda_{mpm} cos(\tilde{\theta}) - k\sigma_{q^*} sgn(\sigma_{q^*})) \end{aligned} \tag{5.44}$$

Where $\sigma sgn(\sigma) = |\sigma|$, and the back-EMF is defined as:

$$e_{d^*} = \omega_r \lambda_{mpm} sin(\tilde{\theta}) \tag{5.45}$$

$$e_{q^*} = -\omega_r \lambda_{mpm} cos(\tilde{\theta}) \tag{5.46}$$

Simplification yields the following:

$$\dot{\boldsymbol{V}}(\boldsymbol{\sigma}) = f(\sigma_{d^*}^2 + \sigma_{q^*}^2) + g(|e_{d^*}||\sigma_{d^*}| - k|\sigma_{d^*}|) + g(|e_{q^*}||\sigma_{q^*}| - k|\sigma_{q^*}|) \tag{5.47}$$

As mentioned above for the system to be globally asymptotically stable, equation (5.41) has to be N.D and then stability would be proven. The gain k is again designed under the worst case scenario as in Section 5.5. The first term of equation (5.47) is always N.D due to $f = -\frac{R_s}{L_s}$. Next two terms are N.D if k is chosen to be:

$$k > max(|e_{d^*}|, |e_{q^*}|) \tag{5.48}$$

For this implementation of the sliding mode controller, in the estimated dq^* the k is chosen to be a constant which satisfies equation (5.48). With this chosen k, the equilibrium point of the system becomes globally asymptotically stable. Furthermore, when the sliding surface is reached by the trajectory, then $\dot{\sigma} = \sigma = 0$ in finite time. The back-EMF voltages (e_{dq^*}), and consequently the angle error converges to zero since e_{dq^*} depends on the angle error [29].

Chattering attenuation

In practice, the sign function will be changed to a sigmoid function, equation (5.49), to attenuate the chattering present in the system. The parameter of the sigmoid function (ϕ) will be tuned experimentally. The effects of it were discussed in [16].

$$F = \frac{\sigma}{\mid \sigma \mid + \frac{\phi}{100}} \tag{5.49}$$

Using the two estimated back-EMF signals ($\hat{e}_{dq^*}$), there are two possible options to calculate the estimated rotor position. The position estimation error can be directly calculated using the tangent function, such as $\hat{\theta} = tan^{-1}(\frac{-\hat{e}_{d^*}}{\hat{e}_{q^*}})$. The positive thing about using the tangent function is that it is robust against magnitude error in the signals, as long as both of them contain the same error. Using the now known $\tilde{\theta}$ and a simple PLL structure, the estimated position ($\hat{\theta}$) and speed ($\hat{\omega}_{r,mech}$) can be acquired. The speed signal is filtered by an LPF before it is fed back to the speed controller.

As it was shown above, the system now using an SMO, realized in dq-reference frame, requires less filtering. Thus a new structure of the system is established and is shown in figure 5.8.

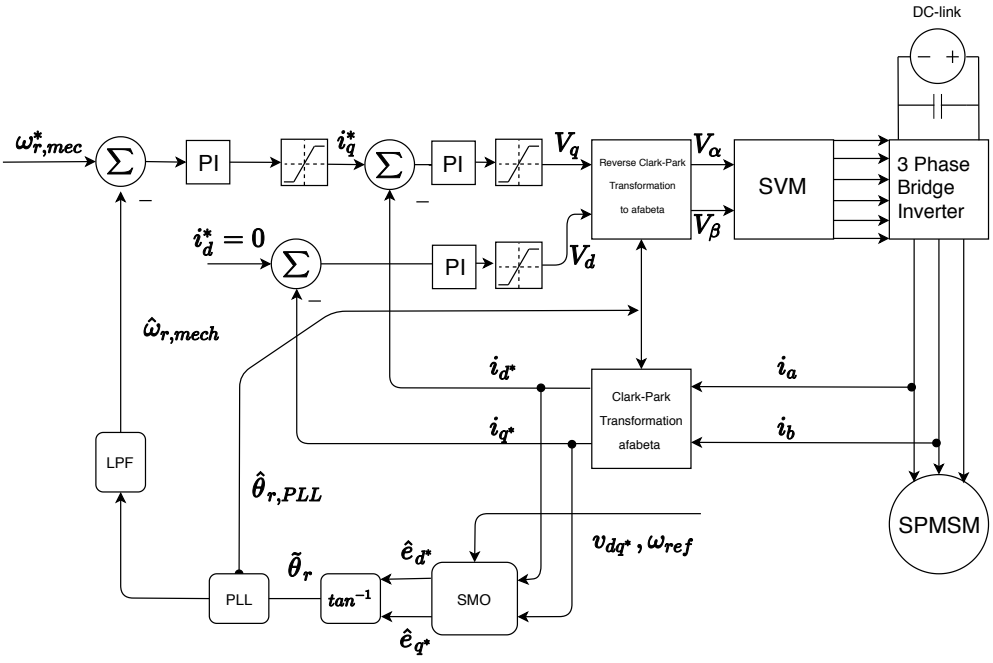

Figure 5.8: *Structure of control system with a first-order sliding mode observer in dq*-reference frame included*

5.8 DC-offset in the estimated signals

It is apparent from experiments in previous reports, such as [16], and data recorded during the first part of the writing of this project, that both the position error and the speed signal contain oscillations. These oscillations have the same frequency as the fundamental electrical frequency, which leads to the conclusion that there is a DC-offset in the system [12].

The frequency of the oscillations was verified in the lab, and the results are shown in figure 5.9. The oscillation frequency is $\frac{1}{0.5679-0.5171} \approx 20Hz$. The electrical frequency is the same at $300rpm$, because $\frac{300N_{pp}}{60} = 20Hz$.

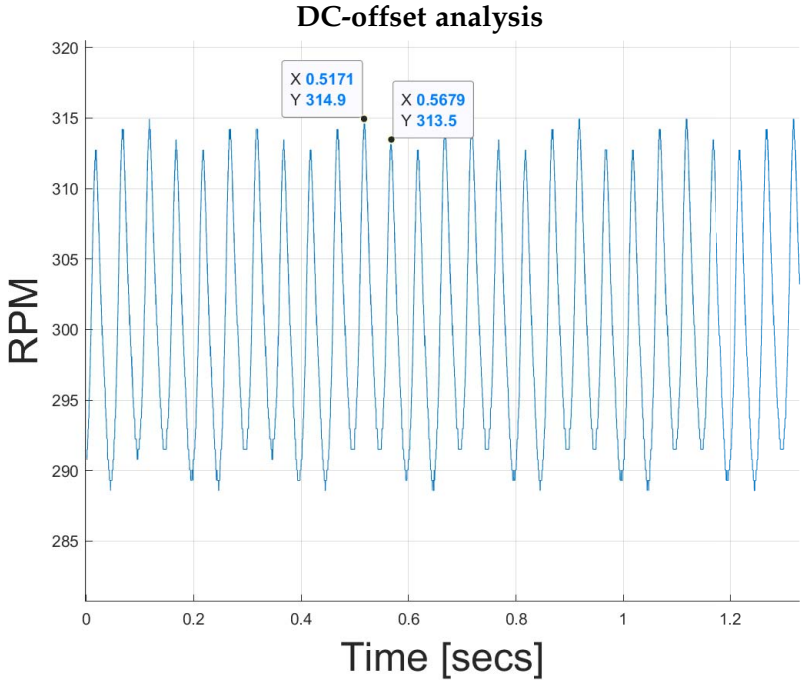

Figure 5.9: *Oscillations present in the speed of the machine due to a DC-offset in the estimated back-EMF signal. Used speed = 300rpm*

This can be partly explained by DC-offset of the inverter and partly with limit cycles present in the sliding mode observer. These two possibilities are further investigated in the upcoming pages.

5.8.1 Analytical analysis of the DC-offset

It was shown analytically in [30] that, if there is a DC-offset in the voltage and current measurements, the output signal of the sliding mode observer is going to contain a DC-offset as well. This is true for both the first-order and the second-order sliding mode observers. The analysis starts from the governing first-order observer equations (5.15), which are repeated here.

$$\begin{aligned} \frac{d\hat{i}_\alpha}{dt} &= f\hat{i}_\alpha + gv_\alpha - g\hat{e}_\alpha \\ \frac{d\hat{i}_\beta}{dt} &= f\hat{i}_\beta + gv_\beta - g\hat{e}_\beta \end{aligned} \tag{5.50}$$

Where $f = -\frac{R_s}{L_s}$ and $g = \frac{1}{L_s}$. Considering only the DC-offset, the voltage model equations become the following:

$$\begin{aligned} 0 &= f\hat{i}_{\alpha,DC} + gv_{\alpha,DC} - g\hat{e}_{\alpha,DC} \\ 0 &= f\hat{i}_{\beta,DC} + gv_{\beta,DC} - g\hat{e}_{\beta,DC} \end{aligned} \tag{5.51}$$

Rewriting the expression yields the next.

$$\begin{aligned} \hat{e}_{\alpha,DC} &= R_s\hat{i}_{\alpha,DC} + v_{\alpha,DC} \\ \hat{e}_{\beta,DC} &= R_s\hat{i}_{\beta,DC} + v_{\beta,DC} \end{aligned} \tag{5.52}$$

It can be observed from equation (5.52) that if the measured voltage and current contain a DC-offset, then the estimated back-EMF voltage will contain a DC-offset as well. This will increase the error in the position and speed estimation and can also cause the previously discussed oscillations. It is assumed that, at the low-speed operation range, it is more difficult to measure the current and voltage accurately, therefore the DC-offset is worse in this speed region.

5.8.2 Existence of limit cycles in the system

The oscillations in the system could also be explained by the existence of limit cycles [1]. A sliding mode observer is non-linear and therefore limit cycles could be present in the system. These are a phenomenon unique to non-linear controllers and observers. Limit cycles can cause oscillations with a given, constant frequency, and amplitude without external excitation. By definition, these are invariant sets and they appear as a closed circle in phase plane analysis [1]. Therefore, it is paramount to investigate the existence of limit cycles in the system. Many methods

were developed and are widely available in the literature to verify the existence of limit cycles, for instance, the Bendixson theorem, but they are limited to second-order systems. None of them are easily applicable to first or higher-order systems [1].

For first-order systems, phase plane analysis, a graphical tool, could be utilized. This is a powerful tool, developed for second-order systems, but by eliminating one of the axes, the order could be reduced. Instead of doing this, only the second-order sliding-mode observer will be analyzed because this allows the use of the previously mentioned analytical tools, which is preferred.

The Bendixson theorem states that: "For a non-linear system, no limit cycle can exist in a region Ω of the phase plane in which $\partial f_1/\partial x_1 + \partial f_2/\partial x_2$ does not vanish and does not change sign" [1].

The analysis sets off by looking at the basic form of the STO observer design, originally introduced in [31]. This is the following:

$$\begin{aligned} f_1 = \dot{x}_1 = -k_1\sqrt{\mid \tilde{x}_1 \mid}sign(\tilde{x}_1) + x_2 + C_1(x_1, t) \\ f_2 = \dot{x}_2 = -k_2 sign(\tilde{x}_1) + C_2(x_2, t) \end{aligned} \tag{5.53}$$

Where $x_i, \tilde{x}_i, k_i, and C_i$, are state variables, error between estimated and actual state variables, observer gains, and perturbation terms, respectively. Using the definition presented above, and assuming that the perturbations terms are zero, the analysis continues such as:

$$\frac{\partial f_1}{\partial x_1} + \frac{\partial f_2}{\partial x_2} = -k_1 \frac{(x_1 - \hat{x}_1)sign(x_1 - \hat{x}_1)}{2 \mid x_1 - \hat{x}_1 \mid^{3/2}} \tag{5.54}$$

Due to the fact, that equation (5.54) becomes zero when the error is zero, which can occur outside of the origin point, the system might have limit cycles in the phase plane. This theorem can only prove that if there are no limit cycles, therefore further analysis is required in this subject.

5.8.3 Phase plane analysis of limit cycles

Phase plane analysis is a graphical method to analyze both the linear and nonlinear second- and first-order systems. Generally, these systems can be described as shown in equation (5.55) [1].

$$\begin{aligned} \dot{x_1} &= f_1(x_1, x_2) \\ \dot{x_2} &= f_2(x_1, x_2) \end{aligned} \tag{5.55}$$

Where x_1, x_2 are the system states and f_1, f_2 are nonlinear functions of the states. Phase plane analysis uses x_1, x_2 as coordinates. After setting the initial conditions, time is varied from zero to infinity, and the solution will be represented as a curve in the phase plane. This curve is called trajectory and it shows the properties of the system.

The method will be used to see if there are limit cycles in the system or not. Also, it can show the equilibrium points, and from the nature of the trajectories, the system properties can be concluded. An equilibrium point is a point in the state space where the states will stay forever. Mathematically this means, that $\dot{\boldsymbol{x}} = 0$ [1]. For the analysis, a MATLAB script called 'pplane8' will be used. The script was made by Hugh Harvey, and George Williams, University of Bristol. The equations from (5.53) are used. The observer gains are chosen to be $k_1 = 1, k_2 = 4$. Changing the gains will scale the trajectories but will not change the governing properties of the system. The initial condition is chosen arbitrarily.

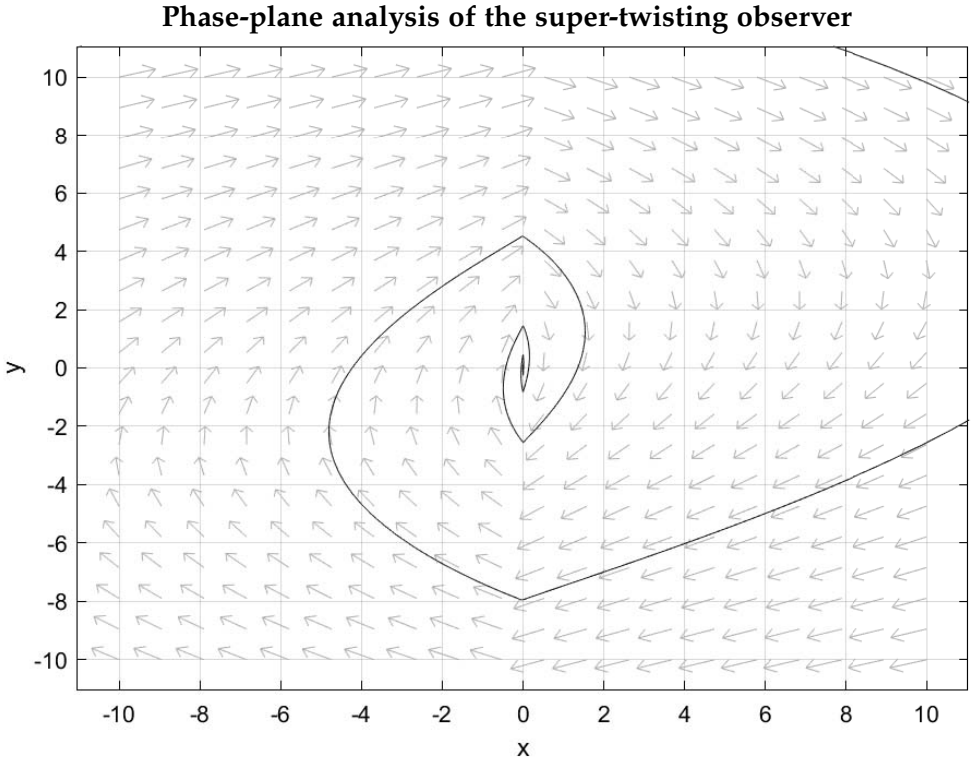

Figure 5.10: *Phase plane analysis of the super-twisting observer using $k_1 = 1, k_2 = 4$, and an arbitrary initial condition. Also, y represents $\dot{x}$. Made with script called 'pplane8' made by Hugh Harvey and George Williams.*

It can be examined from the figure 5.10, that the observer has a stable equilibrium point in (0,0). There are no limit cycles present because there are no closed circles in the phase plane, however, the periodic nature of the motion can be seen from the figure.

5.8.4 Oscillation mitigation strategies

Mitigation of the oscillations is necessary to achieve better sensorless system performance. There are several different methods available, and these are presented in the list below.

- Re-calibration of the current sensors in the system
- Solve the problem at the observer level. Advanced chattering attenuation strategies and gain calculations might help. Also, increasing the sampling frequency of the sampled system will reduce the chattering.

- Open-loop or closed-loop compensation of the DC-offset in the estimated back-EMF signal

The difficulty of the oscillation mitigation strategy increases from top to bottom. Most of the time, catching and solving a problem in a system is easier at the point where it is originated from. Later, the solution could be obscured or amplified by the different components found in the system.

Before the beginning of the experiments, the current sensors will be re-calibrated in the laboratory.

A simple solution to compensate the inverter voltage error is presented in chapter 6, section 6.2.

The observer gain was made adaptive in section 5.5 for the first-order SMO and will be made adaptive for the STO in section 8.

The sigmoid function parameter, for the first-order SMO, was tuned in [16] and the same value will be used here as well.

The DC-offset compensation in the back-EMF signal is discussed in chapter 10.

Chapter 6

Compensation Methods

Compensation methods for the system, are presented and explained in the following chapter.
At low speeds, the VSI has voltage error due to its non-linear effects. VSI non-linearities are caused by dead time, on/off switching device delays, and voltage drops in the inverter [32]. These effects distort the voltage and this causes an error in the estimated signals because the estimator is using the voltage signal (among other signals) for the calculations. The voltage is not directly measured, but rather it is assumed that the commanded voltage is the actual voltage, hence this is the origin of some of the estimation errors. Directly measuring the stator voltages is problematic, because the voltage is composed out of pulses. Filtering the voltage would be necessary then, but filtering also introduces phase lag into the system and that is not acceptable [33]. Therefore a compensation method is desired to make the average voltage error to be zero.

The system uses a traditional two-level VSI and SVM technique. These are discussed in Appendix B, in more detail.

A torque compensation method was used to improve the transient response of the system. A feed-forward load torque observer is introduced to observe the load torque and detect changes in the torque. The observer is then used to compensate for speed changes that occur when the load torque is changed [34].

In this chapter, first, the VSI voltage error is analyzed, then a simple compensation method based on average voltage is given and finally, a feed-forward torque compensation method is introduced.

6.1 Analysis of the VSI voltage error

During the introduction of the two-level VSI, the switches were assumed to be ideal. This means that they were assumed to switch in zero time. In reality, the switches are never ideal. Therefore, a small delay, called dead time is introduced which is necessary to prevent the shoot-through effect. This occurs when both switches are closed at the same time. The dead time can increase or decrease the average voltage in the system [35]. To aid the explanation, a short example, using only one leg, is shown in figure 6.1 and figure 6.2.

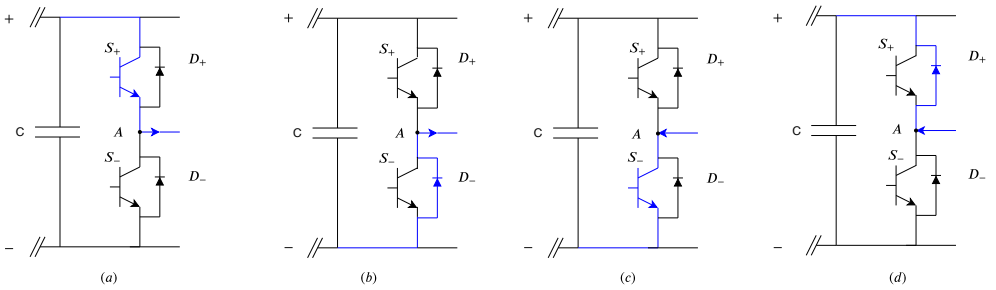

Figure 6.1: *The four different possible states of one leg when considering the dead time effect.*

In case, only the switch is conducting (figure (a), (c)), the switch can be turned off by the gate signal, and this stops the current flowing in that direction immediately. This does not result in a dead time effect.
In case the diode is conducting (figure (b), (d)), the dead time effect occurs, because the diode cannot be closed immediately. This is due to the presence of an inductive load (the motor) in the system.

As it is shown in figure 6.2, the dead time effect occurs between the dotted lines. At first, only the case when the current is positive ($i > 0$) will be considered. The upper switch is conducting and the voltage of point A is equal to $V_{dc} - V_{on}$. Then the switch S_+ is switched off. At this point both switches are open and the current flows through the lower diode. The voltage of point A is the same as the voltage drop on the diode now. Switch S_- is turned on, the lower diode keeps conducting and the forward voltage keeps to be the same because the diode and the switch are in parallel. As a next step, S_- is turned off. The current keeps flowing even after that because the diode keeps conducting until the switch S_+ is switched back on, after the given dead time. The voltage of point A becomes the same as the initial value now. This examined the case results in a loss in the average voltage in the system.

In case the current direction is negative ($i < 0$), first, the upper switch (S_+) is

open and the parallel diode is conducting. Due to this, the voltage of point A, is $V_{dc} + V_D$. When S_+ is turned off, D_+ keeps conducting until the other switch is turned on. It is similar to how it was explained before. This examined the case results in a positive gain in the average voltage in the system.

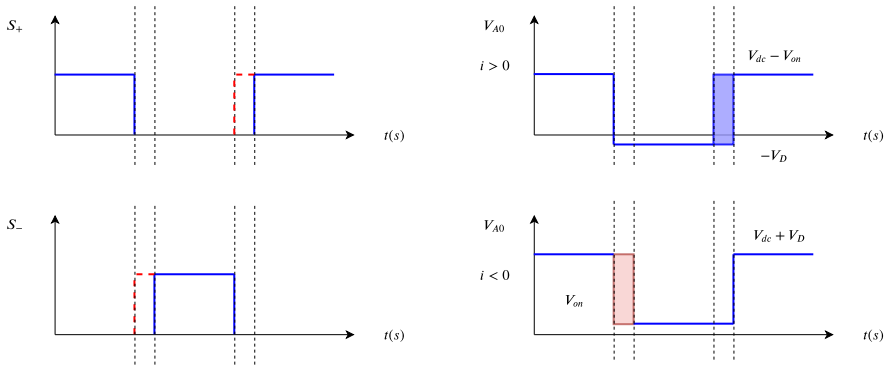

Figure 6.2: *The dead time effect for one sequence when the current is positive.*

Where V_{dc} is the voltage of the power supply, V_{on} is the voltage drop on the switch, and V_D is the voltage drop on the diode.

After further investigation, it is apparent that, due to the snubber capacitor in the system, the voltage cannot change immediately. The snubber capacitor is in parallel with the diode and the switching device. This makes the dead time effect nonlinear, and can be represented by the following equation [35]:

$$\Delta v = \frac{i}{C_{snubber}} \Delta t \tag{6.1}$$

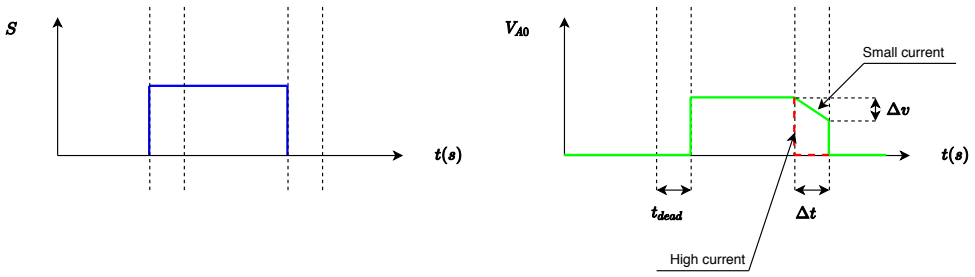

Figure 6.3: *The effect of the snubber capacitor on the dead time effect. Examining one leg and using an arbitrary switching signal.*

Where t_{dead} is the dead time, and S represents the control signal of a switch.

Generally, equation (6.1), cannot be calculated because $C_{snubber}$ is not known and is hard to measure. However, an important conclusion can be drawn: if the current is large enough, the voltage change can be seen as instantaneous, and this effect can be safely disregarded [35]. To interpret what 'large enough' means, data from a previous report [17] (using the same standard setup as this report) will be used. The test was conducted by giving a current step input to the stator α-axis. This ensures that the rotor does not rotate during the test.

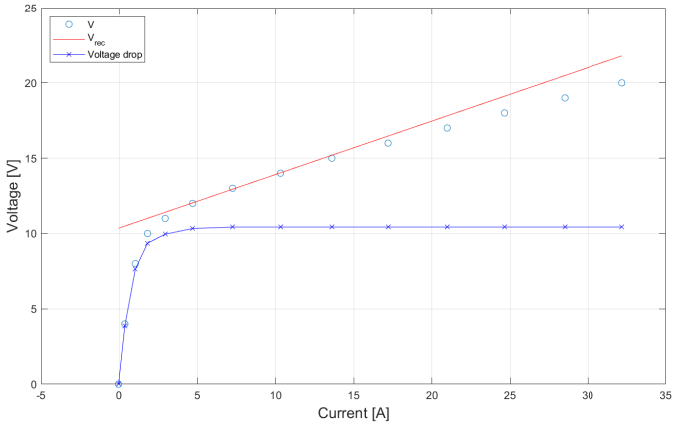

Figure 6.4: *The voltage-current characteristics of the inverter of the setup [17].*

From figure 6.4, it can be observed that the effect of the dead time is linear if the current is larger than $4A$. Below $4A$, the inverter shows high nonlinearities.

6.2 Voltage Compensation Strategy

The voltage compensation strategy is based on the analysis shown in the previous section. The relationship between the output voltage of the inverter and the reference voltage obtained from the current controllers is realized with equation (6.2) [36].

$$\begin{bmatrix} v_a \\ v_b \\ v_c \end{bmatrix} = \begin{bmatrix} v_{a_{ref}} \\ v_{b_{ref}} \\ v_{c_{ref}} \end{bmatrix} - \Delta V \begin{bmatrix} f(i_a) \\ f(i_b) \\ f(i_c) \end{bmatrix} \tag{6.2}$$

Where $f(i)$ is a function of the phase current, and ΔV is the voltage error due to

the dead time of the inverter which varies according to the operating conditions. The voltage error can be calculated as shown in equation (6.3) [36].

$$\Delta V = \frac{t_{dead} + t_{on} - t_{off}}{ts} V_{dc} + \frac{V_{on} + V_D}{2} \tag{6.3}$$

Where t_{dead} is the dead time, t_{on}, t_{off} are the turn-on time and turn-off time of the switching device, V_{on}, V_D are the voltage drops on the switch and the diode, and ts is the sampling period.
It is worth mentioning that the actual voltage error ΔV depends on the load as well due to parameters being a function of the current. For simplicity, this fact is not considered here.

The compensation depends on the direction of the current, therefore the method utilizes the sign function of the phase current as shown in figure 6.5(A) [36]. The function for the phase current is formulated using equation (6.4). For high current region this approach is acceptable. However, for low current regions the sign function is not optimal due to the difficulty of direction detection around zero crossing and the fact that the dead time depends on the magnitude and phase of the current [37]. A better solution is to use the saturation function with a boundary layer k, and keep the using the sign function outside of this layer [36]. This is shown in equation (6.4).

$$f(i) = \begin{cases} i/k, & for\ |i| < k \\ sgn(i), & for\ |i| \geq k \end{cases} \tag{6.4}$$

Where k is the boundary layer parameter of the saturation function which can also be seen in figure 6.5(B). The value of the boundary layer k is arbitrary chosen to be $0.5A$.

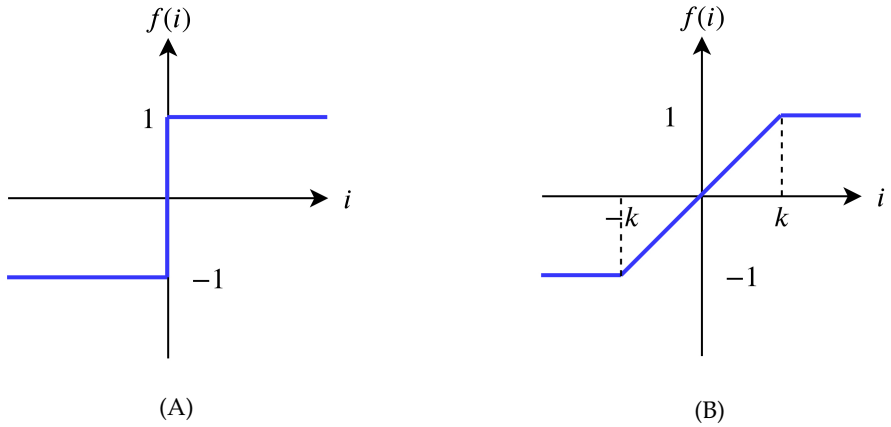

Figure 6.5: *Illustration of the two different forms in equation 6.4*

This is then implemented in the setup, and equation (6.2) is calculated for each cycle after evaluating the direction of the current.

It is worth noting that, in certain applications, the performance could be worse when using the above mentioned compensation technique, because it is open-loop. The compensation changes the voltage input of the duty cycle calculator but there is no feedback present which could correct errors and help to reject disturbances.

With this compensation method, the inverter voltage nonlinearities will be reduced noticeably and the results from the laboratory experiments are presented in Chapter 8.

6.3 Feed-forward Torque Compensation

Another important control objective is to improve the transient response of a given system. In this section, the load torque is estimated, then using feed-forward, the settling time of the system is reduced [34].

To estimate the load torque, a linear state observer is constructed based on the mechanical equations of the system. These were introduced in chapter 2, but for clarity, they are also repeated here in equation (6.6) and in equation (6.5).

$$\frac{d\omega_m}{dt} = \frac{1}{J}(T_e - T_{dist} - B_m\omega_m) \tag{6.5}$$

$$T_e = \frac{3}{2}N_{pp}\left(\lambda_{mpm}i_q\right) \tag{6.6}$$

Load torque (T_L) is an input of the system. It is assumed that the change of it is much slower than the change of rotor speed and position, therefore $\frac{dT_L}{dt} = 0$ [34]. Based on the above mentioned, now the system can be described in state-space form. This is presented in equation (6.7) and in (6.8).

$$\begin{aligned} \dot{\boldsymbol{x}} &= \boldsymbol{A}\boldsymbol{x} + \boldsymbol{B}\boldsymbol{u} \\ \boldsymbol{y} &= \boldsymbol{C}\boldsymbol{x} \end{aligned} \tag{6.7}$$

$$\begin{aligned} \begin{bmatrix} \dot{\omega}_m \\ \dot{T}_L \end{bmatrix} &= \begin{bmatrix} -\frac{B_m}{J} & -\frac{1}{J} \\ 0 & 0 \end{bmatrix} \begin{bmatrix} \omega_m \\ T_L \end{bmatrix} + \begin{bmatrix} \frac{1}{J} \\ 0 \end{bmatrix} T_e \\ \boldsymbol{y} &= \begin{bmatrix} 1 & 0 \end{bmatrix} \begin{bmatrix} \omega_m \\ T_L \end{bmatrix} \end{aligned} \tag{6.8}$$

Before designing the state observer, the observability of the second-order system has to be checked. The observability matrix is shown in equation (6.9).

$$\boldsymbol{Ob} = \begin{bmatrix} \boldsymbol{C} \\ \boldsymbol{CA} \end{bmatrix} \tag{6.9}$$

The matrix is full rank, therefore the system is observable. Utilizing linear control theory, a linear state observer can be designed [20] [34]. This is presented in equations (6.10), (6.11), and (6.12). The last one is the dynamic equation of the state estimation ($\hat{\omega}_m$, $\hat{T}_L$).

$$\dot{\hat{\boldsymbol{x}}} = \boldsymbol{A}\hat{\boldsymbol{x}} \quad + \boldsymbol{B}\boldsymbol{u} + \boldsymbol{L}[\boldsymbol{y} - \boldsymbol{C}\hat{\boldsymbol{x}}] \tag{6.10}$$

$$\dot{\hat{\boldsymbol{x}}} = (\boldsymbol{A} - \boldsymbol{LC})\hat{\boldsymbol{x}} \quad + \begin{bmatrix} \boldsymbol{B} & \boldsymbol{L} \end{bmatrix} \begin{bmatrix} \boldsymbol{u} \\ \boldsymbol{y} \end{bmatrix} \tag{6.11}$$

$$\begin{bmatrix} \dot{\hat{\omega}}_m \\ \dot{\hat{T}}_L \end{bmatrix} = \begin{bmatrix} -\frac{B_m}{J} & -\frac{1}{J} \\ 0 & 0 \end{bmatrix} \begin{bmatrix} \hat{\omega}_m \\ \hat{T}_L \end{bmatrix} + \begin{bmatrix} \frac{1}{J} \\ 0 \end{bmatrix} T_e + \boldsymbol{L}\tilde{\omega}_m \tag{6.12}$$

The equation states that, by designing the observer gains ($\boldsymbol{L} = [l_1; l_2]$) to make the new system $(\boldsymbol{A} - \boldsymbol{LC})$ stable and sufficiently fast, the estimation error is driven to

zero using the estimated speed as a feedback ($\tilde{\omega}_m = \omega_m - \hat{\omega}_m$). Sufficiently fast means that the observer has to be 3-5 times faster than the speed PI controller [20]. $\boldsymbol{L}$ can be designed using the pole placement control approach. The closed-loop poles are placed at the desired place, and the new characteristic equation is calculated. By comparing the coefficients of the new and the old characteristic equations, the gains are found.
In this case, the poles of the new system are placed such as: $s_1 = [-100 - 100j]$, and $s_2 = [-100 + 100j]$. By doing so, the dampening of the system will be $1/\sqrt{2}$, which will result in a stable, fast observer response with an acceptable overshoot [20].
For the given system, the calculated observer gains are the following:

$$\begin{aligned} l_1 &= 200 \\ l_2 &= -292 \end{aligned} \tag{6.13}$$

The block diagram of the state observer is shown in figure 6.6.

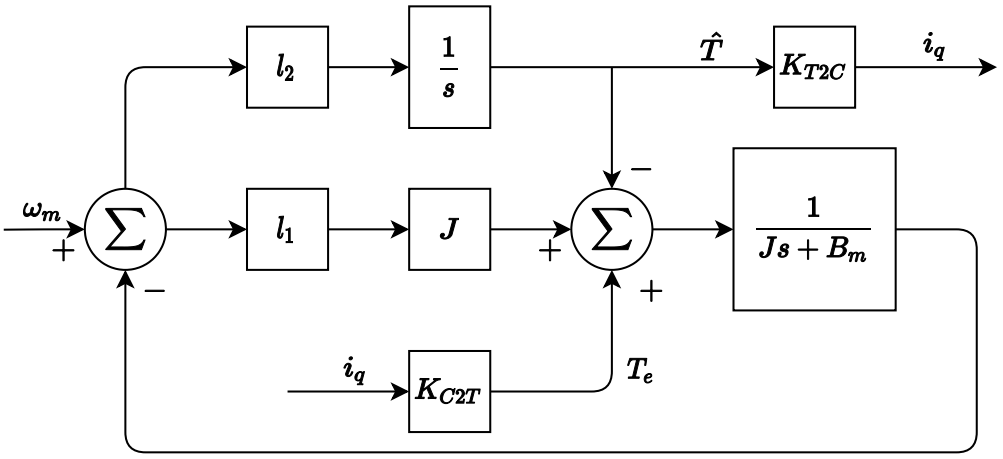

Figure 6.6: Block diagram of the load torque observer.

Where K_{T2C} and K_{C2T} are the constants from torque to current and vice versa. Their equations can be seen in (6.14), and in (6.15).

$$K_{T2C} = \frac{1}{\frac{3}{2} N_{pp} \lambda_{mpm}} \tag{6.14}$$

$$K_{C2T} = \frac{3}{2} N_{pp} \lambda_{mpm} \tag{6.15}$$

The modified block diagram of the system is presented in figure 6.7.

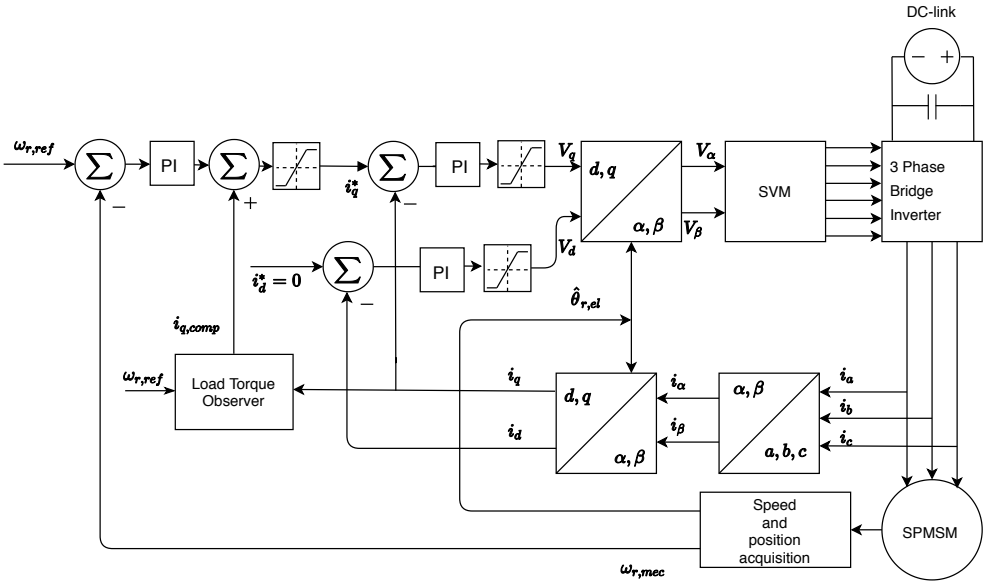

Figure 6.7: Block diagram of the system with a load torque observer.

The compensator will be tested and the effectiveness of it will be verified in section 7.5.

Chapter 7

Simulation Results

This chapter shows and discusses the simulation results of the modeled estimators defined in Chapter 5. The base of all simulations and thus experiments is the FOC scheme introduced in Chapter 3. From a standstill, the motor is commanded to reach the pre-defined low speed using sensored FOC. Sensorless control is only turned on after the system stabilized at low speed. This happens at 0.5 secs.

During the tuning of simulation models, only one parameter will be changed at one step. This allows for a better understanding of the effect of each parameter. The gains of the FOC PI controllers defined above are held constant unless noted otherwise. The parameters for those two controllers are shown in table 7.1 and they are chosen based on report [16].

Table 7.1: *PI parameters used for laboratory work [16].*

System	Description	Notation	Value
Current loop	q-axis proportional gain	Kp_q	3.8
	q-axis integral gain	Ki_q	463
	d-axis proportional gain	Kp_d	3.8
	d-axis integral gain	Ki_d	463
Speed loop	Speed proportional gain	Kp_{speed}	0.1
	Speed integral gain	Ki_{speed}	1
	Anti-windup gain	$K_{as,PM}$	3

The simulation results presented in this chapter include the results of a Closed-loop flux-linkage observer (CLFO), first-order sliding mode observer (SMO), first-order sliding mode observer realized in the estimated dq-reference frame (SMOdq) and a higher-order sliding mode observer (STO). Furthermore, the simulation data was

processed using statistical methods.

7.1 Introduction of the standardized experiments

It is important to establish a standardized environment for the experiments, both in simulations and also in the lab. This makes the results easier to interpret and be compared. The load and speed change profile, which will be used for every test, except when the change is noted, as shown in figure 7.1.

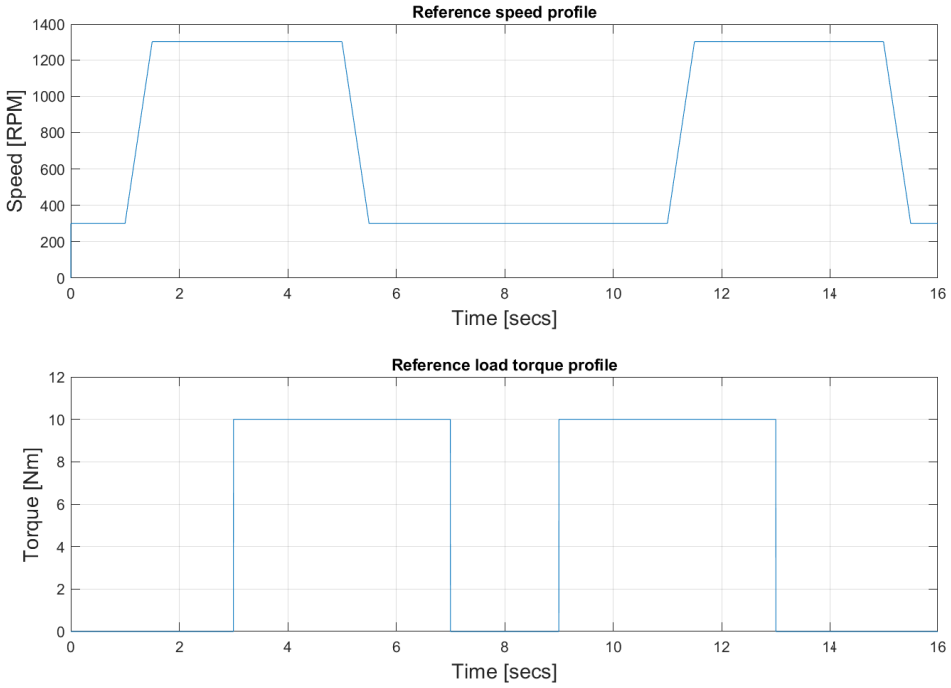

Figure 7.1: *The standardized measuring profile used for every test*

The profiles are symmetric and using them will ensure that every possible operating condition is tested. Low speed is chosen based on the performance of the first-order SMO [16]. The system using this observer is deemed to have a good performance at $300rpm$, but not below that. Further reducing the speed makes the system unstable. The slope of the speed change is $2000rpm/sec$. The speed is changed with a ramp instead of a step to better represent a real application. Also, this makes sure that the test profile is the same for both the simulations and experimental tests. The change of the load torque is defined to be a step-input from

$0Nm$ to $10Nm$. It is also worth noting that the maximum load torque was limited by the IM found in the standard laboratory setup of the University [16].

7.2 Evaluation of data

One of the most important parameters is the position error. Originally, the position is sawtooth-shaped, but instead of unwrapping the signal, one vector will be constructed from the measured position, equation (7.1), and one vector from the estimated position, equation (7.2), at each sampling time. After that, the angle error will be calculated using the dot product definition, as shown in equation (7.3). As the last step, the sign will be corrected, based on whether the estimated position vector is lagging or leading the actual position vector. This is done with equation (7.5). The sign is positive when vector $\vec{v}$ is lagging $\vec{u}$ and negative otherwise [16].

$$\vec{u} = [cos(\theta_{act}), sin(\theta_{act})] \tag{7.1}$$

$$\vec{v} = [cos(\theta_{est}), sin(\theta_{est})] \tag{7.2}$$

$$\theta_{err} = cos^{-1}\left(\frac{\vec{u}(1)\cdot\vec{v}(1) + \vec{u}(2)\cdot\vec{v}(2)}{(norm(\vec{u})\cdot norm(\vec{v}))}\right) \tag{7.3}$$

$$CrossP = \vec{v}(1)\cdot\vec{u}(2) - \vec{v}(2)\cdot\vec{u}(1) \tag{7.4}$$

$$\theta_{err} = \theta_{err}\cdot sign(CrossP) \tag{7.5}$$

It could also be interesting to analyze the speed or position error using statistical methods. The MATLAB function 'mean' is used to calculate average values. A simple variation value is calculated as seen in equation (7.6).

$$Var = \frac{MAX - MIN}{2} \tag{7.6}$$

The root mean square error is a well-known formula that can be used to evaluate the reference speed tracking performance. The equation is shown in (7.7).

$$RMSE = \sqrt{mean(n_{ref} - n_{meas})^2} \tag{7.7}$$

For the calculations, not the whole measuring range is considered, but rather it is calculated for high and low-speed steady states. These sub-ranges are indicated with red boxes on the primary speed graphs. The values will be calculated for every one of the estimators to help evaluating and to compare their performance.

7.3 First-order SMO, SMOdq, and CLFO simulation results

In this section, the simulation results of the tuned first-order sliding mode observer in $\alpha\beta$-reference frame, first-order sliding mode observer in dq-reference frame, and closed-loop flux observer are shown and compared.

The parameters of the first-order sliding mode observer in $\alpha\beta$-reference frame were chosen based on the report [16] and the gains were calculated using equation (5.19). The sigmoid parameter (ϵ_{SMO}), was reduced to 10 from 25. This resulted in a decreased rotor position error.
The SMOdq uses a constant observer gain and it was chosen based on the maximum measurable back-EMF voltage. It was observed that the estimated back-EMF signal contained square-wave components too. The signal was smoothed out by increasing the sigmoid parameter (ϵ_{SMOdq}) from 25 to 200.
The parameters of the CLFO PI controllers were tuned like any other PI controller parameters. First, the proportional gain was increased until the dynamic response was satisfactory, this gain corresponds to the high-frequency domain. After this, the integral gain was increased to achieve the desired overshoot and to remove the steady-state error. Both α-axis β-axis were handled in the same manner.
A first-order PLL was used for all of the observers. The estimated speed was further filtered by a 1st order LPF. All of the filter parameters were kept the same during the tests.

The above mentioned gains are summarized in table 7.2.

Table 7.2: *Estimator and filter parameters used simulations.*

	Description	Notation	Value
SMO parameters	Gain off-set	k_{add}	100
	Sigmoid parameter	ϵ_{SMO}	10
SMOdq parameters	Observer gain	k	500
	Sigmoid parameter	ϵ_{SMO}	200
CLFO parameters	CLFO proportional gain	Kp_{CLFO}	15
	CLFO integral gain	Ki_{CLFO}	100
Filter parameters	PLL cut-off frequency	$\omega_{c,PLL}$	$1570 Rad/s$
	LPF cut-off frequency	$\omega_{c,LPF}$	$500 Rad/s$
	PLL order		1
	LPF order		1

The simulation results, for these cases, are shown in figure 7.2. Here, the real and estimated speeds of the CLFO, SMO, and SMOdq estimators are compared with the reference. Some parts of figure 7.2 are magnified. These are indicated with

red boxes and shown in figure 7.3, and figure 7.4. It should also be noted that the magnified parts are all presented using the estimated speed and position of a given estimator.

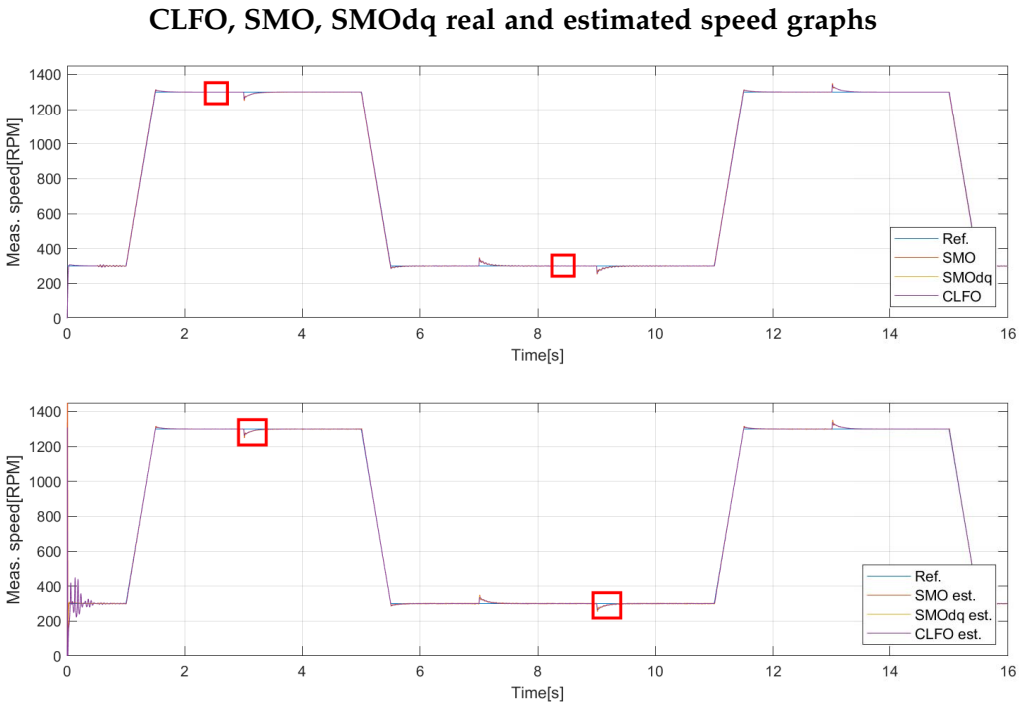

Figure 7.2: *Top graph: measured motor speeds, using different estimators, compared to the reference speed. Bottom graph: the various estimated speeds compared to the reference speed. The indicated parts of the graphs are presented in separate figures.*

Figure 7.3 presents speed signals of the previously mentioned magnified parts. It should be noted that all graphs capture a no-load operation condition since that is the assumed worst-case scenario. From the figure, it can be observed that at high speeds, all the estimators have a similar performance. This is expected because in these cases, the magnitude of the back-EMF voltage signals is relatively large. This makes the estimation process more precise.
At low speeds, the above-mentioned trend continues, but the speed-error is slightly increased. This is in-line with the expectations because at low speeds the amplitude of the back-EMF voltages is comparable to the stator voltages. Thus, they cannot be separated as easily as before, and this results in the estimators to work less reliable.

CLFO and SMOdq estimated speeds contain high-frequency periodic jumps, while the SMO estimated speed contains relatively low-frequency, high magnitude oscil-

lations. The oscillations are the same as it was discussed in section 5.8. The CLFO, SMOdq signals could be further improved by low-pass filtering them, but this is not true for the SMO signal. However, these oscillations can be neglected since they have a minor effect on the, in comparison low bandwidth, speed controller. Furthermore, the filtering was not changed and tuned for one individual observer, because that would have changed the testing methodology.

It can also be examined that the CLFO has a steady-state error in the examined time-range. The signal gets close to the reference but the integration action is not fast enough. On the other hand, SMO and SMOdq do not have steady-state errors. Further increasing Ki_{CLFO} to 200 will result in a faster but more oscillatory transient response.
It can be concluded that, at all speeds, the SMOdq has the best performance since it stabilizes faster than the CLFO, and does not contain the same oscillations as the SMO.

CLFO, SMO, SMOdq real and estimated speed magnified graphs

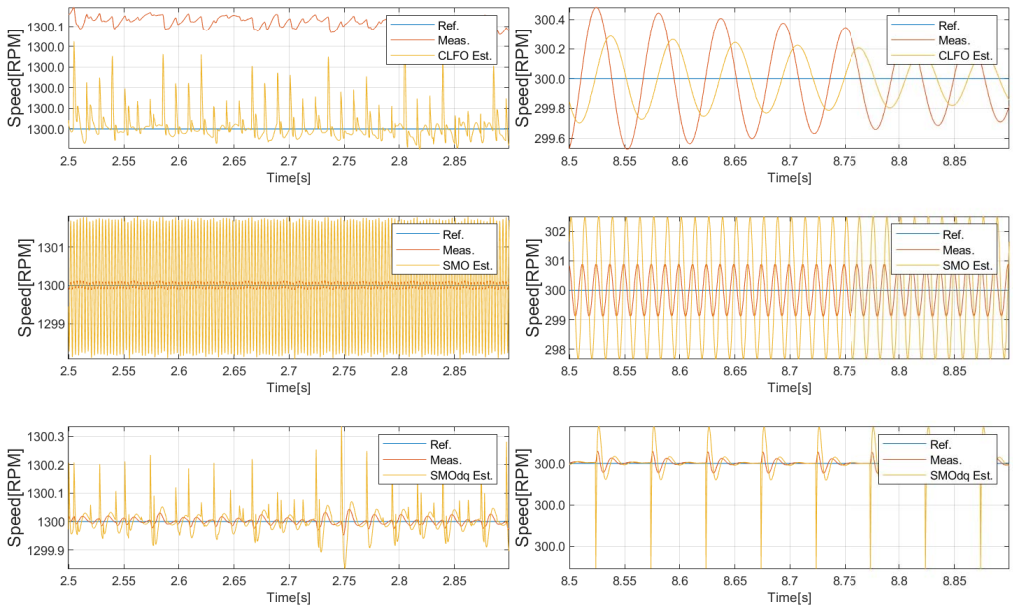

Figure 7.3: *First row: CLFO high speed, and CLFO low speed results. Second row: SMO high speed, and SMO low speed results. Third row: SMOdq high speed, and SMOdq low speed results.*

Next, the transient periods are observed. The magnified graphs of the transient responses are shown in figure 7.4. The layout of the figure is the same as before. The transient response of the speed, when a load torque is added at high speed, shows that the SMOdq has the lowest speed drop out of the three observers. At low

speeds, the SMO and SMOdq have a similar amount of speed change, while the CLFO has the smallest one. However, the CLFO signal has an oscillatory behavior, while the SMOdq is smooth. Again, it takes the CLFO slightly longer time to stabilize than either of the other systems.

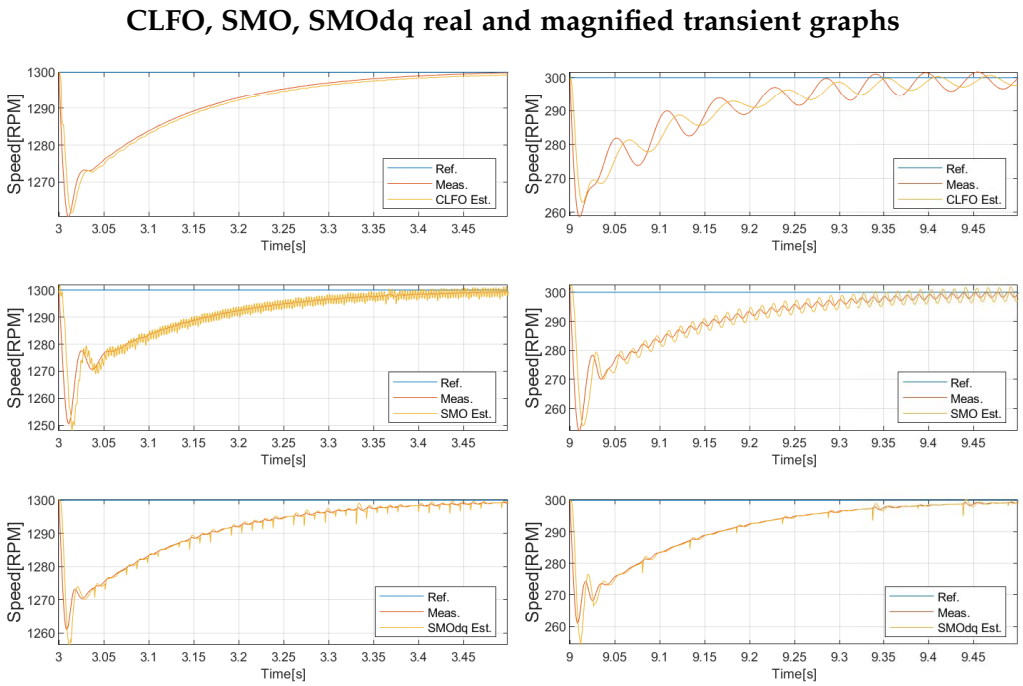

Figure 7.4: *First row: CLFO high speed, and CLFO low speed results. Second row: SMO high speed, and SMO low speed results. Third row: SMOdq high speed, and SMOdq low speed results.*

The estimated and measured positions are shown in figure 7.5. The examined time range is the same as in figure 7.3 and figure 7.4. When observing the estimated position of the three observers at high speed, the SMOdq shows the best performance. The estimated position of the SMO is lagging the measured signal, and in the meantime, the estimated position of the CLFO, and SMOdq is leading the measured signal. At low speeds, the above-mentioned trend continues and the angle error is increased. This is in-line with the expectations. The position angle errors over the same time ranges are shown in figure 7.6. The figure is discussed in the paragraph below.

To analyses the difference between the measured and the actual rotor position, two metrics were calculated: the average angle error, and the variation of them. This was done as presented in section 7.2. The results of these calculations are presented in table 7.3. Figure 7.6 visualizes the data contained in the mentioned

table. In there, it is observed that at high speeds, all of the observers meet the requirements discussed in section 1.4, most importantly to have an error less than 5°.
At low speeds, the simulations show that the SMOdq is the only observer that satisfies the previously defined requirements.

CLFO, SMO, SMOdq real and estimated position magnified graphs

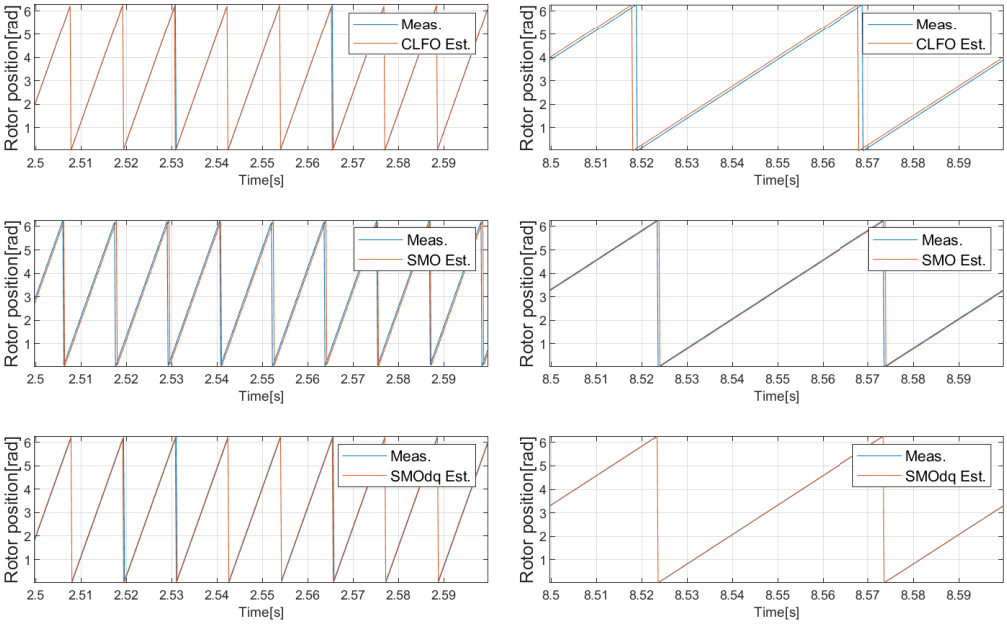

Figure 7.5: *First row: CLFO results. High speed on the left side, and low speed on the right side. Second row: SMO results. High speed on the left side, and low speed on the right side. Third row: SMOdq results. High speed on the left side, and low speed on the right side.*

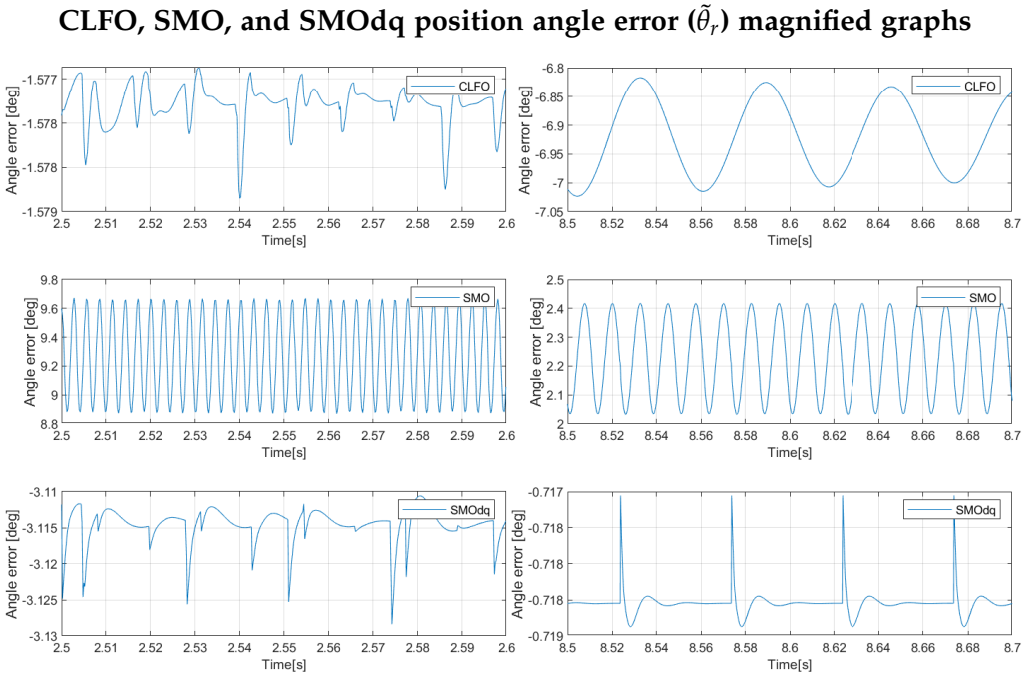

Figure 7.6: *First row: CLFO results. High speed on the left side, and low speed on the right side. Second row: SMO results. High speed on the left side, and low speed on the right side. Third row: SMOdq results. High speed on the left side, and low speed on the right side.*

Table 7.3: *Statistical results of the CLFO, SMO, SMOdq simulations*

Estimator/Operating cond.	CLFO	SMO	SMOdq
Position error, high speed	-1.717°± 0.002°	2.23°± 0.19°	-0.72°± 0.0°
Position error, low speed	-6.867°± 0.002°	8.59°± 0.38°	-2.88°± 0.010°
Overall speed RMSE	7.914rpm	8.159rpm	7.865rpm

The overall speed tracking performance of the systems are very similar to each other, yet, it can be concluded, that the SMOdq performs the best in this metric as well.

7.4 High-order SMO simulation results

In this section, the simulation results of a high-order sliding mode observer, in this case, a super-twisting observer, are presented and compared with the SMOdq observer, which was the best-overall observer from section 7.3.

As it was discussed in section 5.6, an STO has two observer parameters. k_1 corresponds to the dynamic response, and k_2 corresponds to the steady-state performance of the system.

Keeping in mind the above mentioned, first, k_2 was tuned for a given speed (1300 rpm and 300 rpm), next k_1 was tuned so the system remained stable after applying the load-torque (10 Nm). It was found that the system is stable at 1300 rpm with $k_1 = 1.2$, and $k_2 = 5000$ gain choices. However, the system was unstable for a wide range of gain combinations at 300 rpm. k_1 was varied between [0.1, 2], and k_2 was varied between [1000, 5000]. The *sign* function was also changed to a *sigmoid* function (see equation (5.20)), but this could not improve the performance either. Without a stable low-speed operation point, a linear relationship between the reference speed and the gains could not be constructed. It was concluded that the observer is not functional at this low speed.
To be able to show the potential of a system including an STO, the minimum speed of the speed reference, shown in figure 7.1, was increased to 500 rpm. The tuning was re-done, and $k_1 = 0.6$, and $k_2 = 2500$ gain combination yielded a good performance over the whole new speed range (500 - 1300 rpm). The applied load-torque remained the same, and the *sign* function was changed to the *sigmoid* function.

The STO parameters used for the simulations and graphs are summarized in table 7.4.

Table 7.4: *Second-order sliding mode observer tuned parameters*

	Description	Notation	Value
STO parameters	Chattering term gain	k_1	0.6
	Integral term gain	k_2	2500
	Sigmoid parameter	ϵ_{STO}	100

The simulation results of the STO compared with the SMOdq are shown in figure 7.7. The figure is the same as in section 7.3 where the top graph shows the measured speed and the bottom graph shows the estimated speed. Again, the parts highlighted with red boxes are shown in detail in the following graphs. From figure 7.7, it can be observed that the estimators work relatively well over the full-time range.

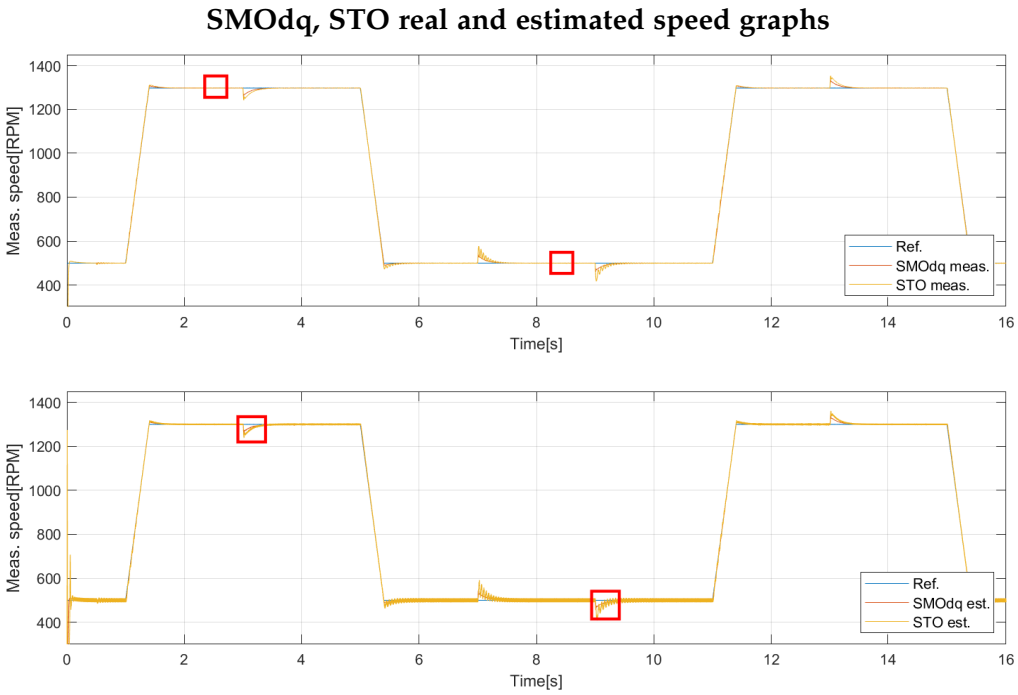

Figure 7.7: *Top graph: measured motor speeds, using different estimators, compared to the reference speed. Bottom graph: the various estimated speeds compared to the reference speed. The indicated parts of the graphs are presented in separate figures.*

Figure 7.8 shows the results of the estimated speed and position at high and low speeds. When comparing these graphs, it clearly shows that the SMOdq has a significantly better performance at both high and low speeds. The STO shows large chattering which is introduced by the k_1 term of the observer law. The chattering could be attenuated by increasing the gain k_2, but this would also reduce the already poor dynamic performance of the system.

When the estimated position is observed, the SMOdq shows the same reflection as the estimated speed. It shows significantly better performance than the STO in both high and low speeds again. The STO at high speed seems to follow the reference relatively well but still shows a difference. The performance of the STO at low speed is not satisfactory. It can be assumed that a relatively large phase-delay is introduced into the system by the integrator term of the estimator. Also, there is an estimation error due to the use of the *sigmoid* function. This was minimized by tuning the parameter ϵ_{STO}.
At the bottom of figure 7.8, the rotor position signals are shown. The STO position signal is leading the reference signal and this phase difference is the largest so far in this report. This subject is further discussed below.

It is worth noting, that no well-developed compensation method for the phase-lag or tuning-method is present in the current literature.

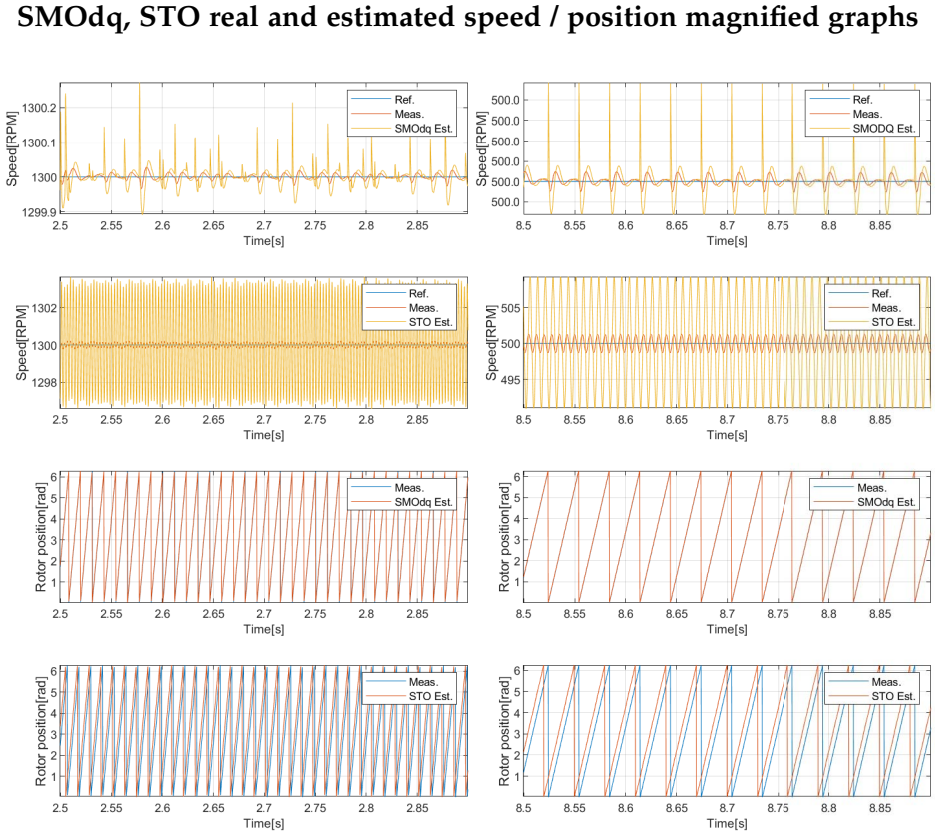

Figure 7.8: *First row: SMOdq high speed, and SMOdq low speed results. Second row: STO high speed, and STO low speed results. Third row: SMOdq position results. High speed on the left side, and low speed on the right side. Fourth row: STO position results. High speed on the left side, and low speed on the right side.*

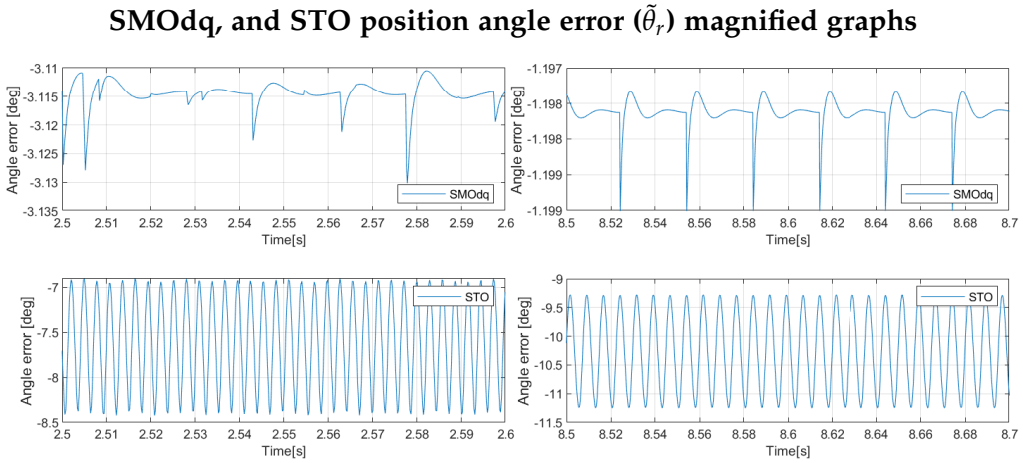

Figure 7.9: *First row: SMOdq results. High speed on the left side, and low speed on the right side. Second row: STO results. High speed on the left side, and low speed on the right side.*

Finally, the transient response of the load changes is examined and shown in figure 7.10. Again, the same may be concluded, that the transient response of the SMOdq is better than the one of the STO. At low speed the transient response of the STO has a lot of oscillations, however, the settling-time is about the same as for the SMOdq.

The difference between the measured and the actual average angle error variation was calculated as presented in section 7.2. The results of these calculations are shown in table 7.5. They are also visualized in figure 7.9. Both system show oscillatory behavior which can be explained by the fact that the systems are digital, therefore sliding mode trajectory is never exactly on the sliding surface in state-space. Table 7.5 shows that the STO could not satisfy the criteria defined in section 1.4.

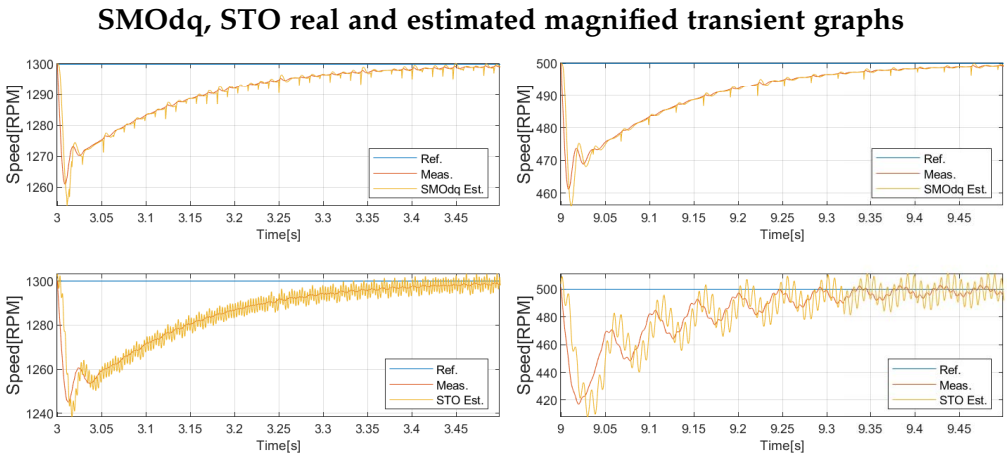

Figure 7.10: *First row: SMOdq high speed, and SMOdq low speed results. Second row: STO high speed, and STO low speed results.*

Table 7.5: *Statistical results of the SMOdq, STO simulations*

Estimators/Operating condition	SMOdq	STO
Position error, high speed	-1.198°± 0.0°	-9.332°± 0.719°
Position error, low speed	-3.115°± 0.012°	-10.244°± 0.984°
Overall speed RMSE	8.278rpm	14.077rpm

The results of the STO simulations showed good potential, but the drawback of the observer is the increased complexity of the tuning process. On the other hand, engineers have a higher degree of control over the properties of the observer. The testing of the STO was continued in the laboratory where the tuning process was further developed.

As a conclusion, the SMO defined in dq-reference frame shows the best performance out of all the developed estimators presented in this report.

7.5 Feed-forward torque compensation simulation results

The feed-forward torque compensation technique, which was introduced in 6.3, is be verified using simulations in this section. The chosen system is the SMOdq, which was proven to have the best performance out all the candidates in 7.3 and 7.4. It will be potentially further improved with the implementation of the compensator.

The observed operation conditions are the same as it was defined in section 7.1, but the main parameters are listed here again. Load torque: $T_L = 10$, speed: 300 rpm and 1300 rpm. Figure 7.11 shows the results for 300 rpm, and figure 7.12 shows the results for 1200 rpm.

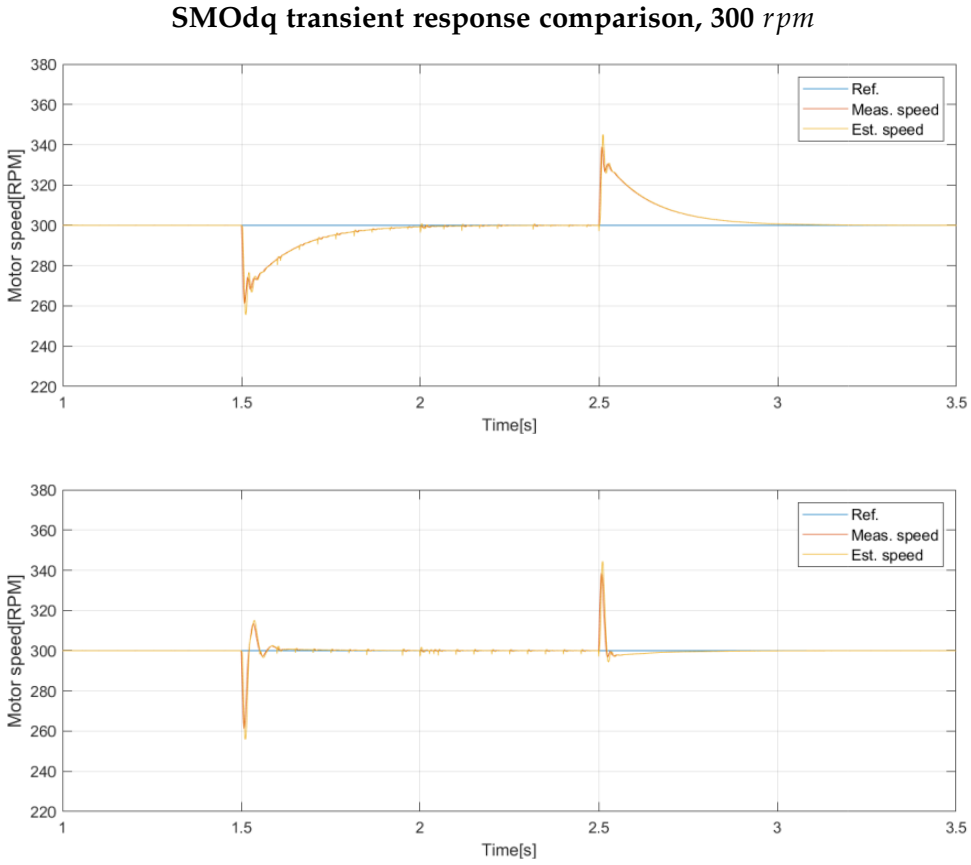

Figure 7.11: Upper figure: without compensator. Lower figure: with compensator. $T_L = 10$, and speed at 300 rpm

It can be observed, that the behavior of the system, including the compensator, shares similarities to a general first-order linear system. The transient response was improved and as a trade-off, a small overshoot is now present. Also, the response is more oscillatory. However, the approximate settling-time was reduced from 0.5 secs to 0.1 secs. This is a significant improvement.

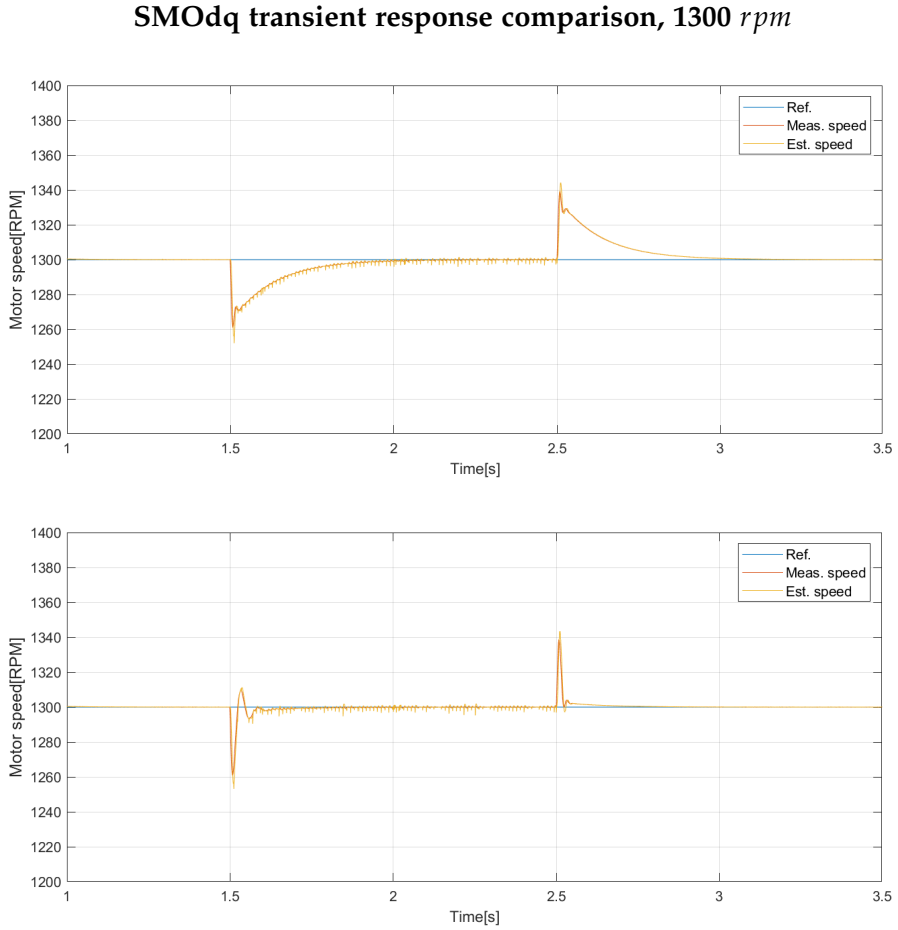

Figure 7.12: Upper figure: without compensator. Lower figure: with compensator. $T_L = 10$, and speed at 1300 rpm

Chapter 8

Experimental Results

The tests were performed in the Drives Control Laboratory of the Energy Technology Department at Aalborg University. The used setup was introduced in section 1.3. The base of every experiment is the FOC scheme which was introduced in chapter 3. All of the measurements start from sensorless operation mode. The system is in steady-state and the motor speed is defined low speed (300 rpm). During the system start-up, sensored FOC was used as it was described in chapter 7. The parameters for the PI controllers are the same as before and are shown in table 7.1.

During the test, only one parameter will be changed at one step. Every change will be indicated in the text. The same methodology was used as in chapter 7. The used speed and load-change profile were defined in section 7.1. The equations used for data evaluation can be found in 7.2.

8.1 Test of the inverter voltage error compensation

The inverter voltage error and its effects were discussed in detail in section 6.1. In this section, the experimental results, using the compensator and the original sensorless control systems, are compared.
The VSI has a custom made PCB, this allows the researchers of the University to change the dead-time between 4 predefined values. In this case, the dead-time was set to be $t_{dead} = 2.5\mu secs$ through all the tests.

First, for comparison purposes, the tests were done without using the inverter voltage compensation. The baseline for the parameters of the estimator and filters were chosen as in the report [16]. The parameters were then slightly re-tuned for

the given setup and are presented in table 8.1.

Table 8.1: *Estimator and filter parameters used for laboratory work, based on [16].*

	Description	Notation	Value
SMO parameters	Sigmoid parameter	ϵ_{SMO}	2.5
	Gain off-set	k_{add}	20
Filter parameters	PLL cut-off freq.	$\omega_{c,PLL}$	$1885 Rad/s$
	LPF cut-off freq	$\omega_{c,LPF}$	$200 Rad/s$
	LPF order		2
	PLL order		2

The results, for this case, are shown in figure 8.1. On the graphs, the same oscillations can be observed as it was discussed in section 5.8.

Test using SMO, without the inverter voltage compensation implemented

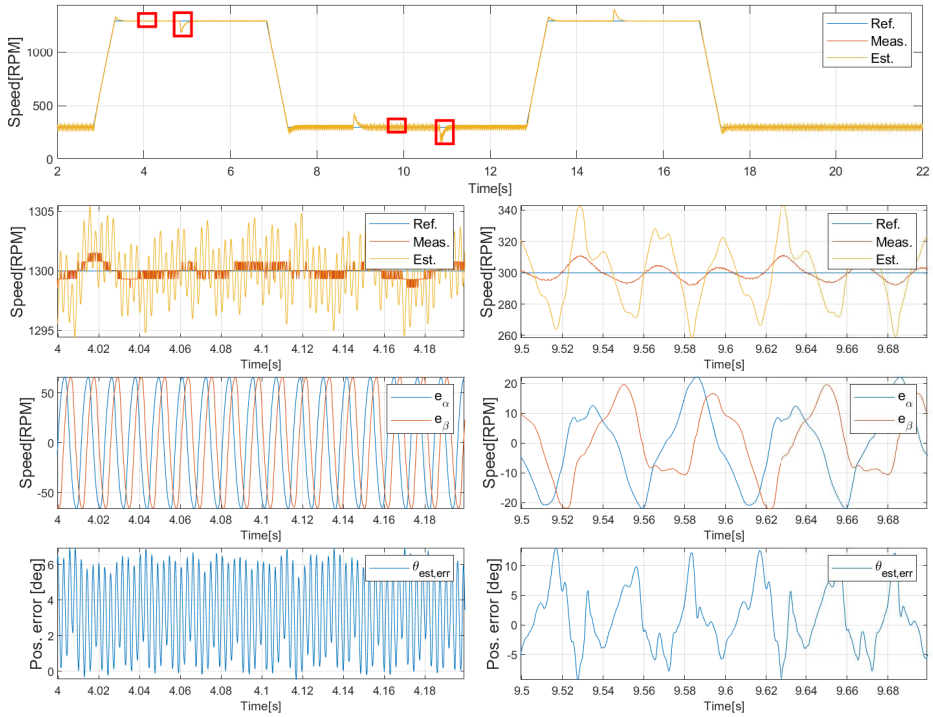

Figure 8.1: *Top graph, the full timeline showing the speed signals. Left side, top to bottom: high speed, no-load condition, steady state speed signals. α and β components of the estimated b-EMF. Position error expressed in degrees. Right side: same measured variables but using low speed, no-load conditions.*

In the next set of figures, namely on 8.2, the highlighted transient responses are shown. It was worth noting that the settling time of the system was faster here (0.2 secs vs 0.5 secs) compared to the simulations. The speed drop was 7.7% and 33.3% during high and low speed operations, respectively. More importantly, the system remained stable when it was loaded at low speed.

Test using SMO, without the inverter voltage compensation implemented, transient responses

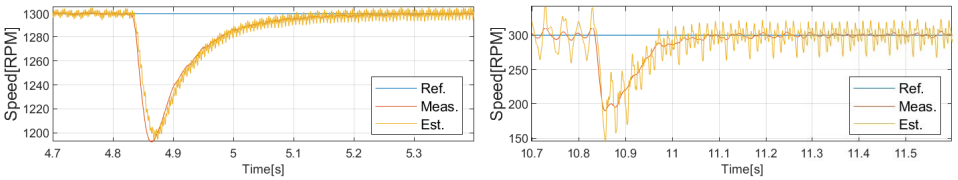

Figure 8.2: *Left graph: high speed. Right graph: low speed.*

For the next experiment, the method was repeated but with the inverter voltage compensation included. In the voltage compensation equation (6.3), only t_{dead} was chosen to be not 0. This is a reasonable simplification because other parameters have a lesser impact, and most of them are not known precisely. The parameters are often not listed in the data-sheet of the manufacturer and are hard to isolate for accurate measurements. The results are shown in figure 8.3.

Test using SMO, with the inverter voltage compensation implemented

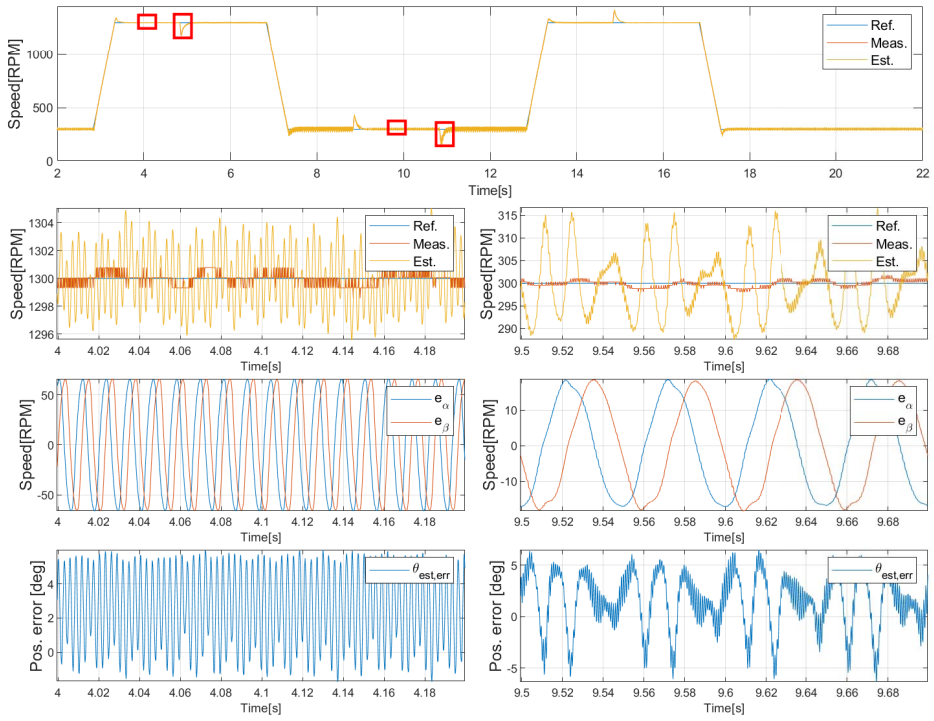

Figure 8.3: *Top graph: the full timeline showing the speed signals. Left side, top to bottom: high speed, no-load condition, steady state speed signals. α and β components of the estimated b-EMF. Position error expressed in degrees. Right side: same measured variables but using low speed, no-load conditions.*

In figure 8.4, the transient responses are presented of the compensated system. The inverter voltage error compensation does not effect the transient response in a significant way.

Test using SMO, with the inverter voltage compensation implemented, transient responses

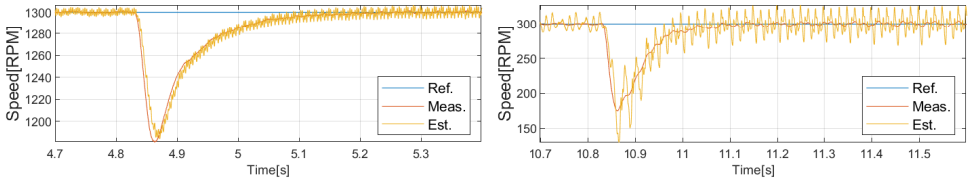

Figure 8.4: *Left graph: high speed. Right graph: low speed.*

As it can be observed from the graphs, the waveform of the estimated back-EMF was improved a lot at the low-speed operation range. The waveform is closer to pure sinusoidal and the offset of it was greatly removed as well. Due to this, both the position and the speed signal estimations became more accurate. The average angle error variation was calculated as presented in section 7.2, and is summarized in table 8.2.

Table 8.2: *Statistical results of the voltage error compensation experimental tests*

Estimators/Operating condition	SMO without comp.	SMO with comp.
Position error, high speed	2.49 °± 3.93°	3.29 °± 3.81°
Position error, low speed	1.16 °± 11.06°	1.52 °± 6.79 °
Overall speed RMSE	12.39 rpm	12.38 rpm

Starting with the low speed data first, the position error changed from $\theta_{err} = 1.16° \pm 11.06°$ to $\theta_{err} = 1.52° \pm 6.79°$. The error offset change from 0 was in the margin of error but the variation of angle error was reduced. Therefore, it can be seen, that the performance of the system is enchanted in the low-speed region.
In the high-speed region, the difference in the angle variation is minor and can be concluded as an error in the measurements. It changed from $\theta_{err} = 2.49° \pm 3.93°$ to $\theta_{err} = 3.29° \pm 3.81°$. This is expected due to the fact that the inverter voltage error does not affect the system as heavily when the commanded voltage is significantly higher than 0.
The speed RMSE for the total examined range did not change. This is also in line with the expectations because the compensator should barely affect the tracking performance.

As a result of the tests shown above, the inverter voltage compensation will be used for every measurement from now on.

8.2 Robustness tests of the observer

As for any model-based observer, the degree of how susceptible a given system is to initial parameter uncertainties or changes-over-time is of paramount importance. To test this, chosen system parameters were changed in a realistic way. The permanent magnet rotor flux-linkage (λ_{mpm}) was reduced by 25%, the stator inductance (L_s) was reduced by 25%, and the total system resistance (R_{sys}) was increased by 50%. This scenario simulates a major temperature increase after running the motor for a long period of time.

The subject of the tests was the first-order sliding mode observer using voltage

error compensation. The tests were done using the same method as before. The results are shown in figure 8.5.

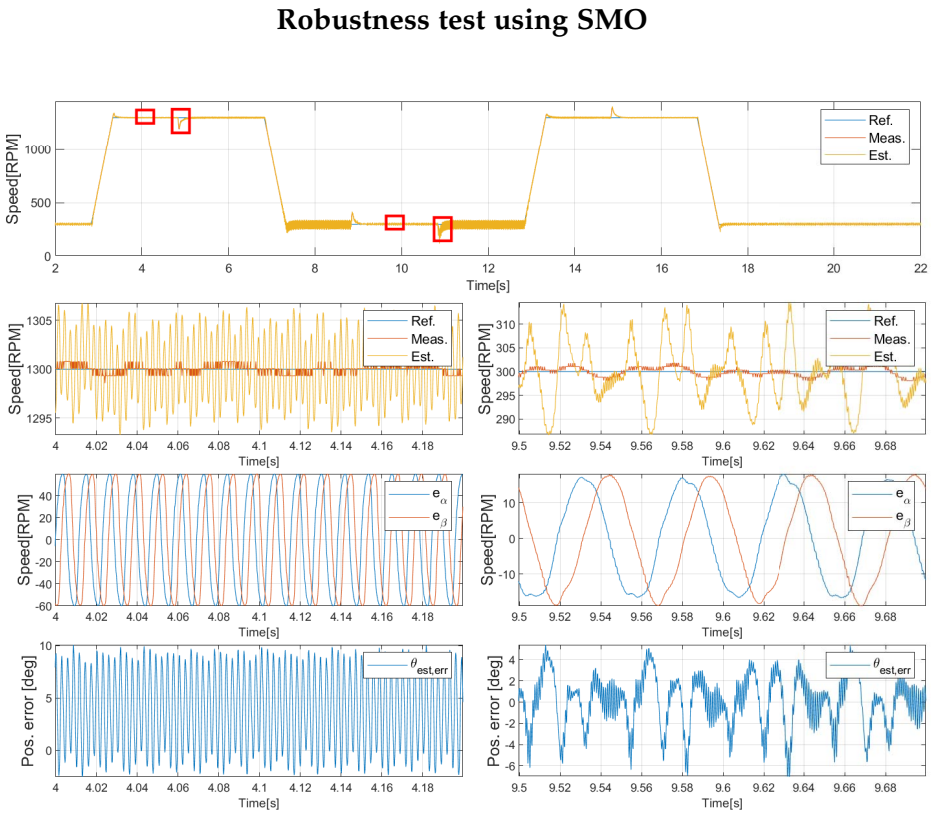

Figure 8.5: *Top graph, the full timeline showing the speed signals. Left side, top to bottom: high speed, no-load condition, steady state speed signals. α and β components of the estimated b-EMF. Position error expressed in degrees. Right side: same measured variables but using low speed, no-load conditions.*

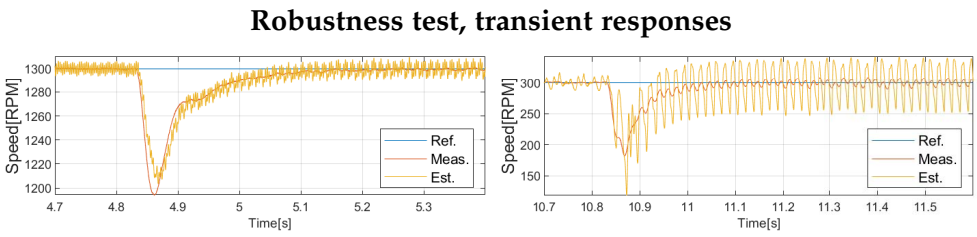

Figure 8.6: *Left graph: high speed. Right graph: low speed.*

It can be observed that the SMO is robust against system parameter changes. The performance of the estimator was decreased, but this is normal. This means that

a motor can be safely operated for prolonged periods of time. Also, spending less time identifying the parameters might be acceptable, which makes the designing of the control system more efficient.

Here as well, the transient responses of the system are shown in figure 8.6. The results follow a simila trend as it was discusses before.

It is worth noting, that further increasing the parameter error, namely doubling the system resistance and halving the other parameters made the system unstable. The exact point of the system becoming unstable was not identified, since it is out of scope of the project.

8.3 Second-order sliding mode observer results

In this section, the second-order sliding mode observer was implemented, tuned, and tested on the setup. The voltage error compensation was also included in the system. The advantages and basics of tuning the observer were discussed in section 5.6, and in section 7.4.

The system was tuned slightly differently than in section 7.4 to further improve the observer.
The parameters of the STO observer are dependent on the speed because the perturbation terms (see equation 5.24) of the motor are dependent on the speed. Thus, the observer gains were made to be a linear function of the reference speed. It was assumed that a linear relation between them is the optimal one. This means that in the coordinate system of n_{ref} and k_1 or k_2, the function is a line. Also, the reference speed was used because it was assumed that the speed error is relatively small, and it is a convenient signal to use, due to the fact that it does not contain any noise.

Keeping in mind the above mentioned, first, in steady-state, k_2 was tuned for a given speed, next k_1 was tuned for a small speed step-change (50-100rpm). It was observed in the laboratory that, in case the system is able to withstand this speed step-change, it will withstand the application of the load-torque as well, but not vice-versa. The tuning was done by changing the slope and offset of the aforementioned lines.
The steady-state performance was made worse as a trade-off to get a better transient response. However, the transient response still remained a problematic point. The equation of the k_1 gain calculation was augmented with the following term: $k_{1,error}(n_{est} - n_{ref})$. This is a pragmatic solution (not part of the original stability-proof) and partially enchanted the poor dynamic performance.

When relatively good parameters were found, the system was fine-tuned for as large of a speed range as possible. This required decreasing both of the observer gains, therefore the reduction of the total observer gain.
However, even after a long tuning-process, the system could not be made stable during the speed-step change. The speed range had to be changed from 300-1300 rpm to 500-1300 rpm, and the applied load-torque had to be decreased to $5Nm$ in order to make the system stable in the transients. This is the same change as the change made during the simulations. The tuning process was deemed to be problematic and elongated, therefore the tuning was not continued.

The used parameters for the STO are summarized in table 8.3.

Table 8.3: *Second-order sliding mode observer tuned parameters*

	Description	Notation	Value
STO parameters	Slope of k_1 gain	$k_{1,gain}$	0.0005
	Offset of k_1 gain	$k_{1,offset}$	-0.4
	Slope of k_2 gain	$k_{2,gain}$	1.5
	Offset of k_2 gain	$k_{2,offset}$	0
	Error gain of k_1	$k_{1,error}$	0.002

Using these values the parameters at $500rpm$ steady-state were the following: $k_1 = 0.006$ and $k_2 = 750$.

Finally, the results of the STO are compared with the SMO, using the inverter voltage error compensation, and the sensored system in figure 8.7. The different transient responses of the systems are also presented in figure 8.8.

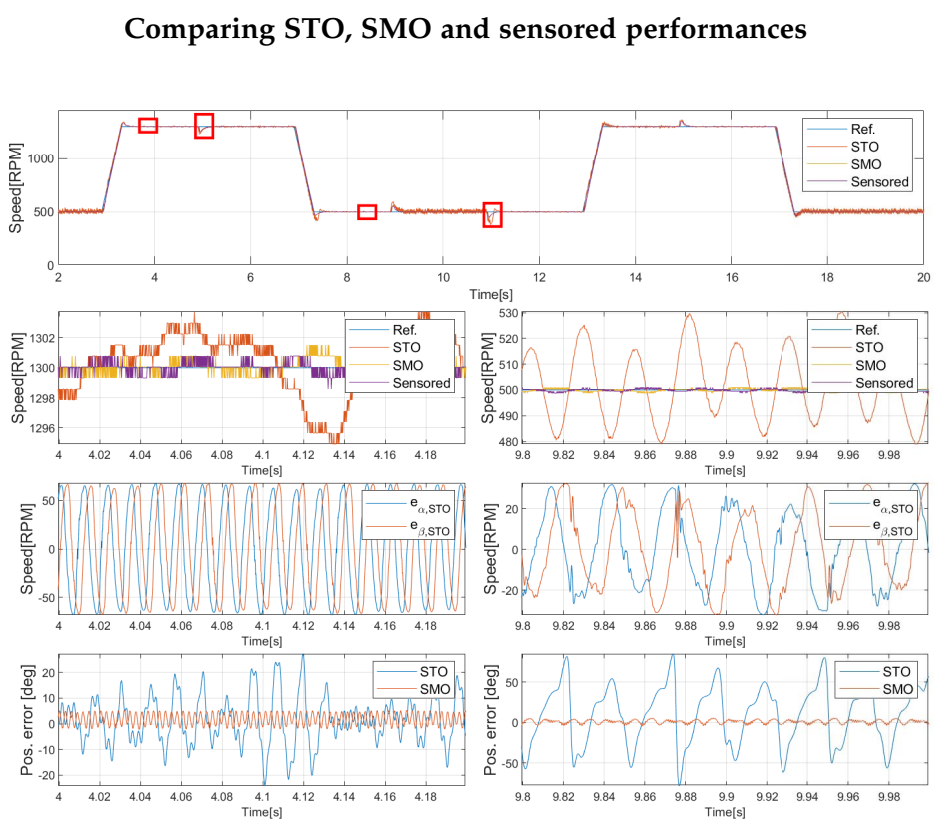

Figure 8.7: *Top graph, the full timeline showing the speed signals. Left to right, top to bottom: high speed, no-load condition, steady state speed signals. Low speed, no-load condition, steady state speed signals. High speed transient response, and low speed transient response. Position error expressed in degrees: left for high speed, right for low speed.*

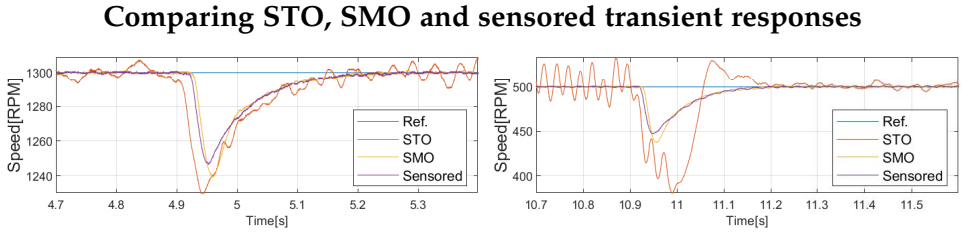

Figure 8.8: *Left graph: high speed. Right graph: low speed.*

It is worth noting that the SMO behaved slightly differently than before. This is due to the modified testing profile and the fact that the filters were tuned for a lower speed operation condition.

The statistical metrics are calculated for this case and the results are shown in table

8.4.

Table 8.4: *Statistical results of the STO experimental tests*

Estimators/Operating condition	SMO	STO
Position error, high speed	1.78 °± 3.79°	-38.84 °± 25.72°
Position error, low speed	1.02 °± 4.93°	-29.67 °± 81.92 °
Overall speed RMSE	7.3 rpm	16.05 rpm

As expected, from the preliminary tests, the STO performed worse in every metric compared to the SMO. Also, keep in mind, that the STO is far from reaching the same low speeds as the SMO.

The conclusion is the same as it was in section 7.4. The STO has the potential to give good results but the time investment might be too immense for certain systems. It might be more efficient to use a first-order sliding mode observer instead, and put more focus into the filtering structure. It is worth noting that this could widely change from setup to setup.

Chapter 9

Discussion and Conclusion

In this chapter, the discussion and conclusion of the project are presented. The decisions made during the design and the implementation process are further analyzed. The possible options will also be listed.

Also, the chapter ends with the final conclusion of the report. The results are summarized and then compared with the criteria defined in the problem statement section, section 1.4.

9.1 Discussion

The system was modeled without including noise and disturbances. This was done to simplify the modeling part of the project and allow more time to be spent on the estimators. It has to be stated the total system is very complex and modeling each and every one of the parts, for instance, the VSI, was out of the scope of this thesis.

The chosen control scheme of the system was FOC because this is the most used control scheme in the industry and in research papers. Using this ensures wider viability of the estimators designed in this report. FOC has two control loops, one for current, and one for speed. In compliance with linear control theory, the outer loop was chosen to have 10 times smaller bandwidth, than the one of the inner loop. This choice is also supported by the natural system dynamics because the mechanical system is always slower than the electrical one. As indicated before, the design of the controllers is heavily based on [16], this is due to the FOC not being the main focus of this thesis.

A detailed coupling effect analysis was also done because it is an often overlooked

topic in research papers. It can be seen from the motor voltage equations that the system is coupled. The equations can be decoupled by compensating for the back-EMF term. This term is not known precisely in sensorless control systems, therefore the compensation cannot be done. It is rather assumed that the current PI controllers regard this term as a disturbance and are able to successfully reject it. The coupling effect was analyzed using SVD and it was found that, at the speeds examined by this thesis, the coupling effect can be safely disregarded.

The CLFO was introduced to have a flux-linkage based estimator as a baseline of the tests. Due to the closed-loop property of it, it showed good performance in many research papers. Later on, the first order sliding mode observer was designed using the sigmoid function. It was proven to need heavy filtering and therefore the complexity of the system was increased. To tackle this problem, first, a second-order SMO (namely, an STO) was implemented. With the use of an integral term in the observer law, it was shown in research papers that the direct output signal of the observer was improved (e.g. had decreased chattering), and thus, less filtering was needed. Next, a first-order SMO was designed in the dq-reference frame, because in this reference frame, the signals used for the estimation are DC signals. Manipulating DC signals introduces less phase-delay in the system than when it is done with sinusoidal signals. This also results in the need for less filtering than before.
The observer parameters were calculated based on model parameters, and it is important to emphasize that these always contain errors due to parameter uncertainties.

It was found in [16], that the system using the first order SMO has oscillations in the estimated speed and position signals. The problem was revisited, and after experimental tests and further analysis, it was found that the implementation of a voltage error compensator would result in a decent improvement. Next, the compensator was designed based on dead-time, switching on and off time, and based on the voltage loss on the device. It was determined that the dead-time has the biggest effect on the calculation. Also, the other parameters are not known precisely. For these reasons, only the dead-time was used in the final version of the compensator. However, it was not used in any of the simulations. This is because the VSI was not modeled in details, therefore the voltage error was not present in the simulation model.

The simulations showed that the transient response of the systems is rather slow. The settling time was 0.4 - 0.5 secs, and there was no overshoot present. A need for a load torque compensator arose. Even with the utilization of a simple feed-forward load torque compensation, the transient response was significantly improved.

During all of the simulation and experimental tests, the system was started up from standstill using regular, sensored FOC. The sensorless mode was turned on after the system has stabilized. This was done to make the tests more fluent and also quicker.
In order to design a fully sensorless system, an individual start-up control, such as *I-f* or *V/f*, also has to implemented. An example of this can be found in [16].

The filter parameters were kept the same for all of the estimators. This means that they were not tuned individually for an estimator. This was done to have fewer variables between systems. The background of the filters (PLLs, and LPFs) was already established in [16] and it was not revisited again. No new filter was introduced in this report.

9.2 Conclusion

This section concludes the project in an organized manner. The objective, or problem statement, of this thesis, was to develop a sensorless control strategy for a PMSM motor that would perform better than the first-order sliding mode observer developed in the report [16].

A dynamic model of the SPMSM was developed to use as a basis for further development of estimators, and also for simulations. A state-space model of the SPMSM was also formulated which was used to further analyze the coupling effect of the system. Field oriented control was introduced to control the torque and flux in the motor separately, and effectively. The FOC control scheme met the set design criteria of overshoot, steady-state error, bandwidth, and stability.

Four sensorless estimators were designed and explained. All estimators were designed to estimate the rotor speed and angle. First, a closed-loop flux observer was designed. The basis of this estimator is a PI controller. The stability of this was verified with linear control theory tools. The states are calculated from the estimated flux-linkage vector.
Next, a first-order sliding mode observer, a second-order sliding mode observer, and a sliding mode observer in an estimated dq-reference frame were developed. In this time, the speed and position are calculated from the estimated back-EMF signals. The stability of the sliding mode observers was proven using the Lyapunov-theory. These also gave equations for the gain choices. Later, all estimators were fine-tuned experimentally where an emphasis was put on the low-speed performance.

Simulation data of all estimators are presented, and as a conclusion, the sliding mode observer in the estimated dq-reference frame was proven to have the best

overall performance. This is true for both at low speed and at high speed. It is worth mentioning that the SMOdq output signals required less filtering, there for the order of the PLL and LPF could be reduced to a fist-order one. This was only shown in simulations.
The lowest achievable speed with a sensorless control system is always of interest. The lowest speed during all the tests was kept at 300 rpm. It was found the all observers are stable at this speed, except for the STO, and using this speed is representative enough of the low-speed performance of the estimators. 300 rpm is 6.7% of the rated speed. It is also worth noting, that the minimum achievable speed of the SMO was 75 rpm, 125 rpm for the SMOdq, and 125 rpm for the CLFO. However, these tests were done in simulation, and the limiting factors are the noise and disturbances found in the real system. Thus, a major conclusion cannot be made from this data.
To counter the increased noise in the real system, and to push the speed even lower, the filter cutoff frequencies have to be reduced. This can be safely done up to 10 times the frequency of the bandwidth of the controller in the given loop. Below this frequency, the controller performance is reduced. Therefore, an estimator which requires less filtering is desired. The SMOdq also excels in this regard.

Unfortunately, only the first-order sliding mode observer and the second-order sliding mode observer were tested in the laboratory due to access restrictions. Out of those two, the first order sliding mode observer showed to have better performance. A better tuning strategy needs to be developed for the second-order sliding mode observer to have improved performance.

All aspects of this thesis were aimed to make improvements and further develop the previously mentioned system. The SMO strategy is robust against parameter uncertainties and noise, and in the estimated dq-reference frame the signals emulate a DC signal which is easier to follow and phase-lag is no longer an issue. This sensorless control is able to work well down to 300 rpm while maintaining a sub 5°rotor position angle error ($\tilde{\theta}_r$). Namely, the angle estimation error was $0.72° \pm 0.0°$ at high speed, and $2.88° \pm 0.01°$ at low speed, which is well under the set performance criteria. The SMOdq provided a steady-state speed error of less than 1 rpm at both high and low speed.
By implementing the feed-forward torque compensation, the settling time after a torque change was reduced by 0.4 secs. This is a significant improvement.
In the laboratory, the effectiveness of the voltage error compensation was shown. The system proved to be robust against parameter changes up to 25% of their base value. The disturbance and noise rejection of the system was also satisfactory.

The final conclusion is made by only relying on simulation results. It can, therefore, be concluded that the SMOdq is able to fulfill all of the performance criteria set for

this thesis in section 1.4. A continuation of this project would be to implement the SMOdq in the drive-lab and see if those results hold up there as well.

Chapter 10

Future Work

In this chapter, the possible future work that could be done for this project is presented. Further improvements of the system could yield lower minimum operation speed, smaller rotor position angle error, and better transient response

10.1 Re-tuning of the STO

It has to be noted, that the tuning of the STO was not a hundred percent successful. An efficient re-tuning method of the Super Twisting observer could improve the already established results. If an algorithm was found that could adequately tune the system based on the reference speed or the speed error, the STO has the potential of having the best performance of all the other estimators. However, the known tuning methods were already revised in this report, thus a new way has to be developed or a new research paper has to be published before continuing with this problem.

10.2 Sliding mode load-torque observer

Furthermore, a sliding mode load-torque observer could be developed to improve the transient response of the system even more. A sliding mode load-torque observer is thought to have better performance than the compensation explained in section 6.3, due to the advantages that a sliding mode observer has, such as the disturbance and noise rejection. It also has low parameter sensitivity and is fairly easy to implement [38].

The mathematical model of load torque identification algorithm sliding mode observer (LTID-SMO) is derived from the mechanical equations of the system. These are repeated in equations (10.1) and (10.2).

$$\frac{d\omega_m}{dt} = \frac{1}{J}(T_e - T_{dist} - B_m\omega_m) \tag{10.1}$$

$$T_e = \frac{3}{2}N_{pp}\left(\lambda_{mpm}i_q\right) \tag{10.2}$$

The mathematical model of load torque identification algorithm sliding mode observer (LTID-SMO) is acquired by substituting (10.1) into equation (10.2).

$$\frac{d\omega_m}{dt} = \frac{1}{J}(\frac{3}{2}N_{pp}(\lambda_{mpm}i_q) - B_m\omega_m - T_L) \tag{10.3}$$

Where J is the total inertia of the system and T_L is the load torque.

Then, the estimated equation of the LTID-SMO can be expressed such as [38]:

$$\frac{d\hat{\omega}_m}{dt} = \frac{1}{J}(\frac{3}{2}N_{pp}(\lambda_{mpm}i_q) - B_m\hat{\omega}_m - ksign(\hat{\omega}_m - \omega_m)) \tag{10.4}$$

Where $\hat{\omega}_m$ is the estimated speed, and k is the observer gain.
The system defined in equation (10.3) is first order, therefore the sliding variable directly gives the speed estimation error, as seen in equation (10.5).

$$S = \tilde{\omega}_m = \hat{\omega}_m - \omega_m \tag{10.5}$$

According to the stability theory of a conventional SMO, as explained many times in this thesis, when the sliding variable reaches the sliding surface, the system reaches steady-state and the following is satisfied:

$$S = \dot{S} = 0 \tag{10.6}$$

Furthermore, the estimated load torque can be defined such as:

$$\hat{T}_L = J \cdot k \cdot sign(\tilde{\omega}_m) \tag{10.7}$$

By using the sign function, system chattering is introduced, and to achieve a smoother signal a low pass filter is implemented to filter out the high-frequency chattering of the signal [38].

$$LPF = \frac{\omega_{LPF}}{s + \omega_{LPF}} \tag{10.8}$$

Where ω_{LPF} is the cut-off frequency of the LPF. A block diagram of the LTID-SMO is shown in figure 10.1.

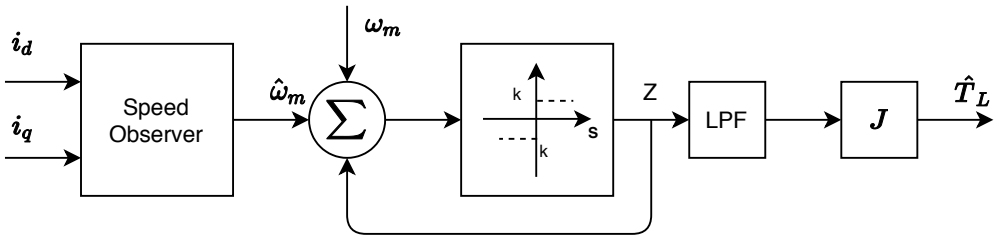

Figure 10.1: Block diagram of the conventional LTID-SMO

The stability analysis of this SMO is not considered here but can be found in [38]. The sign function could be replaced, in order to reduce chattering and to get a smoother signal, like it was explained in [38]. This observer could be used in place of the feed-forward torque observer to improve the torque control of the system.

10.3 Second order sliding mode observer in *dq*-reference frame

Finally, it would be interesting to see if a sliding mode observer in the *dq*-reference frame could be designed since that observer showed the most promising performance during the project.

The previous version of the observer law would be extended. The general, simplified form of a Super twisting observer is repeated in equation (10.9).

$$\begin{aligned} \dot{x}_1 &= -k_1\sqrt{|\ \tilde{x}_1\ |}sign(\tilde{x}_1) + x_2 \\ \dot{x}_2 &= -k_2 sign(\tilde{x}_1) \end{aligned} \tag{10.9}$$

Where the notation is the usual one.
Dividing the sliding mode part of the observer law into two parts has several advantages. First of all, the chattering of the observer output now can be controlled by the second, integrator term. This could potentially mean a better output signal which requires less filtering before feedback. Secondly, with the usage of the first term, the dynamic performance of the system could be enhanced.

Bibliography

[1] J.-J.E. S. Li and Weiping, *Applied Nonlinear Control*. New Jersey: Prentice Hall, 1991, ISBN: 0-13-040890-5.

[2] H. Kim, J. Son, and J. Lee, "A high-speed sliding-mode observer for the sensorless speed control of a PMSM", *IEEE Transactions on Industrial Electronics*, vol. 58, no. 9, pp. 4069–4077, 2011, ISSN: 02780046. DOI: 10.1109/TIE.2010.2098357.

[3] M. Blanke, M. Kinnaert, J. Lunze, and M. Staroswiecki, *Diagnosis and Fault-Tolerant Control*, Second edi. New York: Springer, 2006, p. 685, ISBN: 9783540356523.

[4] D. Wilson, *Motor Control Compendium*, 2011.

[5] P. Vas, *Sensorless Vector and Direct Torque Control*. Oxford: Oxford University Press, 1998, ISBN: 0 19 856465 1.

[6] K. Lu, "Control of Electrical Drive Systems and Converters Lecture 1 Slides", pp. 1–30, 2019.

[7] M. Schroedl, "Sensorless control of AC machines at low speed and standstill based on the 'INFORM' method", *Conference Record - IAS Annual Meeting (IEEE Industry Applications Society)*, vol. 1, pp. 270–277, 1996, ISSN: 01972618. DOI: 10.1109/ias.1996.557028.

[8] O. Benjak and D. Gerling, "Review of position estimation methods for PMSM drives without a position sensor, part III: methods based on saliency and signal injection", *2010 International Conference on Electrical Machines and Systems, ICEMS2010*, pp. 873–878, 2010.

[9] G. Xie, K. Lu, S. K. Dwivedi, J. R. Rosholm, and F. Blaabjerg, "Minimum-Voltage Vector Injection Method for Sensorless Control of PMSM for Low-Speed Operations", *IEEE Transactions on Power Electronics*, vol. 31, no. 2, pp. 1785–1794, 2016, ISSN: 08858993. DOI: 10.1109/TPEL.2015.2426200.

[10] Y. D. Yoon, S. K. Sul, S. Morimoto, and K. Ide, "High-bandwidth sensorless algorithm for AC machines based on square-wave-type voltage injection", *IEEE Transactions on Industry Applications*, vol. 47, no. 3, pp. 1361–1370, 2011, ISSN: 00939994. DOI: 10.1109/TIA.2011.2126552.

[11] G. R. Slemon, "A Permanent Magnet Motor Drive without a Shaft Sensor", *IEEE Transactions on Industry Applications*, vol. 27, no. 5, pp. 1005–1011, 1991, ISSN: 0093-9994. DOI: 10.1109/28.90359.

[12] D. Wang, K. Lu, and P. O. Rasmussen, "Improved Closed-Loop Flux Observer Based Sensorless Control Against System Oscillation for Synchronous Reluctance Machine Drives", *IEEE Transactions on Power Electronics*, vol. 34, no. 5, pp. 4593–4602, 2019, ISSN: 08858993. DOI: 10.1109/TPEL.2018.2865348.

[13] Z. Zheng, Y. Li, and M. Fadel, "Sensorless control of PMSM based on extended Kalman filter", *2007 European Conference on Power Electronics and Applications, EPE*, 2007. DOI: 10.1109/EPE.2007.4417275.

[14] Z. Wang, K. Lu, and F. Blaabjerg, "A simple startup strategy based on current regulation for back-EMF-based sensorless control of PMSM", *IEEE Transactions on Power Electronics*, vol. 27, no. 8, pp. 3817–3825, 2012, ISSN: 08858993. DOI: 10.1109/TPEL.2012.2186464.

[15] M. Rashid, N. Kumar, and A. Kulkarni, *Power Electronics Devices, Circuits and Applications*. 2014, p. 1027, ISBN: 978-0-273-76908-8.

[16] MCE2-823 (incl. Barna Temesi), "Sensorless Control of PMSM Drive Using Sliding-Mode-Observer", Aalborg University, Aalborg, Tech. Rep., 2019.

[17] PED1-740, "Parameter Identification Aiming for High Performance Permanent Magnet Drive System", Aalborg University, Aalborg, Tech. Rep., 2018.

[18] J. S. Kim and S. K. Sul, "High performance PMSM drives without rotational position sensors using reduced order observer", *Conference Record - IAS Annual Meeting (IEEE Industry Applications Society)*, vol. 1, pp. 75–82, 1995, ISSN: 01972618. DOI: 10.1109/ias.1995.530286.

[19] G. Zhang, F. Zhao, Y. Wang, X. Wen, and W. Cong, "Analysis and optimization of current regulator time delay in Permanent Magnet Synchronous Motor drive system", *2013 International Conference on Electrical Machines and Systems, ICEMS 2013*, no. 5, pp. 2286–2290, 2013. DOI: 10.1109/ICEMS.2013.6713235.

[20] C. L. Phillips and R. D. Harbor, *Feedback Control Systems*, 4th Editio. New Jersey: Prentice Hall, 2000, ISBN: 0-13-949090-6.

[21] G. Torkel, L. Lennart, and L. Lennart, *Control Theory: Multivariable and Nonlinear Methods*. London: Taylor & Francis, 2000, p. 467, ISBN: 0-7484-0877-0.

[22] S. Skogestad and I. Postlethwaite, *Multivariable Feedback Control: Analysis and design*, Second edi. JOHN WILEY & SONS, 2001, p. 590, ISBN: 978-0-470-01167-6.

[23] K. Lu, "Control of Electrical Drive Systems and Converters Lecture 2 Slides", pp. 1–20, 2019.

[24] Z. Qiao, T. Shi, Y. Wang, Y. Yan, C. Xia, and X. He, "New sliding-mode observer for position sensorless control of permanent-magnet synchronous motor", *IEEE Transactions on Industrial Electronics*, vol. 60, no. 2, pp. 710–719, 2013, ISSN: 02780046. DOI: 10.1109/TIE.2012.2206359.

[25] Y. Shtessel, C. Edwards, L. Fridman, and A. Levant, *Sliding Mode Control and Observation*, 1st. Birkhäuser Basel, 2014, p. 356, ISBN: 978-0-8176-4892-3. DOI: 10.1007/978-0-8176-4893-0.

[26] C. Zhou, Z. Zhou, W. Tang, Z. Yu, and X. Sun, "Improved Sliding-Mode Observer for Position Sensorless Control of PMSM", *2018 Chinese Automation Congress (CAC)*, no. 3, pp. 2374–2378, 2018. DOI: 10.1109/CAC.2018.8623482. [Online]. Available: https://ieeexplore.ieee.org/document/8623482/.

[27] M. Comanescu, "Speed, rotor position and load torque estimation of the PMSM using an extended dynamic model and cascaded sliding mode observers", *2016 International Symposium on Power Electronics, Electrical Drives, Automation and Motion, SPEEDAM 2016*, pp. 98–103, 2016. DOI: 10.1109/SPEEDAM.2016.7525806.

[28] D. Liang, J. Li, and R. Qu, "Super-twisting algorithm based sliding-mode observer with online parameter estimation for sensorless control of permanent magnet synchronous machine", *ECCE 2016 - IEEE Energy Conversion Congress and Exposition, Proceedings*, pp. 1–8, 2016. DOI: 10.1109/ECCE.2016.7855479.

[29] V. C. Ilioudis, S. Member, and N. I. Margaris, "Speed and Position Estimation Technique for PMSM Based on Modified Machine Model", pp. 407–415, 2010.

[30] L. Guo, H. Wang, N. Jin, L. Dai, L. Cao, and K. Luo, "A Speed Sensorless Control Method for Permanent Magnet Synchronous Motor Based on Super-Twisting Sliding Mode Observer", *2019 14th IEEE Conference on Industrial Electronics and Applications (ICIEA)*, pp. 1179–1184, 2019. DOI: 10.1109/iciea.2019.8834074.

[31] A. Levant, "Sliding order and sliding accuracy in sliding mode control", *International Journal of Control*, vol. 58, no. 6, pp. 1247–1263, 1993, ISSN: 13665820. DOI: 10.1080/00207179308923053.

[32] D. Liang, J. Li, R. Qu, and W. Kong, "Adaptive second-order sliding-mode observer for PMSM sensorless control considering VSI Nonlinearity", *IEEE Transactions on Power Electronics*, vol. 33, no. 10, pp. 8994–9004, 2018, ISSN: 08858993. DOI: 10.1109/TPEL.2017.2783920.

[33] S.-K. Choi, Jong-Woo; Sul, "Inverter Output Voltage Syn . thesis Using", *IEEE Transactions on Power Electronics*, vol. 11, no. 2, 1996, ISSN: 00219738. DOI: 10.1172/JCI117060.

[34] Z. Kuang, B. Du, S. Cui, and C. C. Chan, "Speed Control of Load Torque Feedforward Compensation Based on Linear Active Disturbance Rejection for Five-Phase PMSM", *IEEE Access*, vol. 7, pp. 159 787–159 796, 2019, ISSN: 21693536. DOI: 10.1109/ACCESS.2019.2950368.

[35] K. Lu, "Modern Electrical Drives Lecture 7 Slides", 2019.

[36] Y. Inoue, K. Yamada, S. Morimoto, and M. Sanada, "Effectiveness of voltage error compensation and parameter identification for model-based sensorless control of IPMSM", *IEEE Transactions on Industry Applications*, vol. 45, no. 1, pp. 213–221, 2009, ISSN: 00939994. DOI: 10.1109/TIA.2008.2009617.

[37] A. Munoz-Garcia and T. A. Lipo, "On-line dead time compensation technique for open-loop PWM-VSI drives", *Conference Proceedings - IEEE Applied Power Electronics Conference and Exposition - APEC*, vol. 1, no. 608, pp. 95–100, 1998.

[38] W. Lu, Z. Zhang, D. Wang, K. Lu, D. Wu, K. Ji, and L. Guo, "A New Load Torque Identification Sliding Mode Observer for Permanent Magnet Synchronous Machine Drive System", *IEEE Transactions on Power Electronics*, vol. 34, no. 8, pp. 7852–7862, 2019, ISSN: 08858993. DOI: 10.1109/TPEL.2018.2881217.

[39] K. Lu and W. Dong, "Dynamic Modelling of Electrical Machines and Control Systems Lecture 2 Slides", Lecture slides 2, 2018.

[40] ——, "Dynamic Modelling of Electrical Machines and Control Systems Lecture 10 Slides", Lecture slides 10, 2018.

[41] J. A. Moreno and M. Osorio, "A Lyapunov approach to second-order sliding mode controllers and observers", *Proceedings of the IEEE Conference on Decision and Control*, pp. 2856–2861, 2008, ISSN: 01912216. DOI: 10.1109/CDC.2008.4739356.

Appendix A

Reference Frame Transformation

A reference frame transformation is done by using vector projection. Vector projection is a powerful tool that consists of two parts. To aid the explanation, arbitrarily chosen vectors are presented in figure A.1. First, the given f vector is rotated by the angle α. Now, vector v is aligned with the x-axis and f vector is placed $\gamma - \alpha$ degrees from the axis. As the last step, by taking the real part of the vector, the projected vector is acquired.

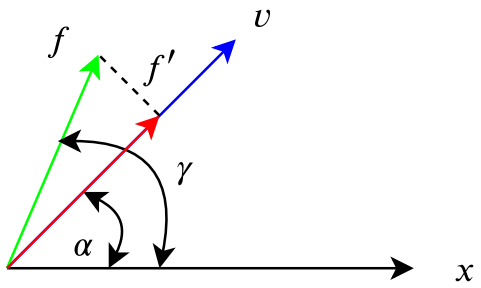

Figure A.1: *Vector projection using arbitrary vectors*

The vector projection is summarized in the equation (A.1) below.

$$f' = Re(\frac{f}{e^{j\alpha}}) \tag{A.1}$$

Where taking the real part of the expressions is done by forming the complex conjugate of the given f vector, denoted as $\bar{f}$, and using it in equation (A.2).

$$Re(f) = \frac{f + \bar{f}}{2} \tag{A.2}$$

The reason for this transformation is mainly to reduce complexity when working with differential equations and to eliminate time-varying components. The following method is applied when deriving the voltage equation from stationary *abc* to rotating *dq*0-reference frame transformation. The rotating *dq*0-reference frame is chosen to describe the differential equations of the motor because it allows for the motor variables to be seen as constant values [39].

A general vector in the *abc* reference frame is given by equation A.3.

$$\bar{f}_{abc} = \frac{2}{3}(f_a e^{j0^\circ} + f_b e^{j120^\circ} + f_c e^{-j120^\circ}) \tag{A.3}$$

A general vector in the *dq*0-reference fram is given by equation A.4

$$\bar{f}_{dq} = (f_d - f_q)e^{j\theta} \tag{A.4}$$

where θ is the angle between the two reference frames as shown in figure A.2. Since the system *a*,*b*,*c* variables are balanced or symmetrical, the zero component $f_0 = 0$ or as illustrated in equation A.5.

$$f_0 = \frac{1}{3}(f_a + f_b + f_c) = 0 \tag{A.5}$$

In figure A.2 the two reference frames are illustrated where $\bar{f}$ is an arbitrary vector seen in both *abc* and *dq*0 frames.

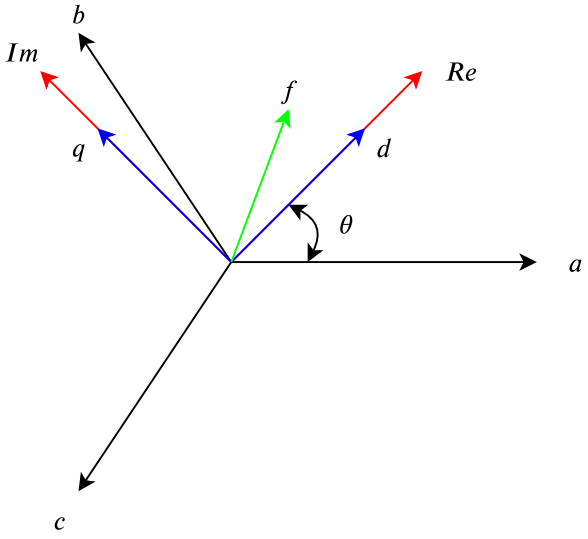

Figure A.2: *dq reference frame in the abc reference frame illustration.*

From the figure, it can be seen that the q-axis is leading the d-axis by 90° and shifted from the a-axis by angle θ. If the a-axis is used as a reference axis the d and q components become the following.

$$\begin{aligned} f_d &= Re\left(\frac{\bar{f}_{abc}}{e^{j\theta}}\right) = Re\left(\frac{2}{3}\left(\frac{f_a e^{j0^{\circ}} + f_b e^{j120^{\circ}} + f_c e^{-j120^{\circ}}}{e^{j\theta}}\right)\right) \\ &= \frac{2}{3}(f_a cos(\theta) + f_b cos(\theta - 120^{\circ}) + f_c cos(\theta + 120^{\circ})) \end{aligned} \tag{A.6}$$

$$\begin{aligned} f_q &= Re\left(\frac{\bar{f}_{abc}}{e^{j\theta+90^{\circ}}}\right) = Re\left(\frac{2}{3}\left(\frac{f_a e^{j0^{\circ}} + f_b e^{j120^{\circ}} + f_c e^{-j120^{\circ}}}{e^{j\theta+90^{\circ}}}\right)\right) \\ &= \frac{2}{3}(-f_a sin(\theta) - f_b sin(\theta - 120^{\circ}) - f_c sin(\theta + 120^{\circ})) \end{aligned} \tag{A.7}$$

Therefore, the transformation matrix for the abc to $dq0$ transformation becomes equation (A.8)

$$\begin{bmatrix} f_d \\ f_q \\ f_0 \end{bmatrix} = K_{abc2dq} = \frac{2}{3}\begin{bmatrix} cos(\theta) & cos(\theta - 120^{\circ}) & cos(\theta + 120^{\circ}) \\ -sin(\theta) & -sin(\theta - 120^{\circ}) & -sin(\theta + 120^{\circ}) \\ \frac{1}{2} & \frac{1}{2} & \frac{1}{2} \end{bmatrix}\begin{bmatrix} f_a \\ f_b \\ f_c \end{bmatrix} \tag{A.8}$$

Substituting this to the motor voltage differential equation (A.9), results in the following calculations.

$$\begin{bmatrix} i_a \\ i_b \\ i_c \end{bmatrix} = \begin{bmatrix} R_s & 0 & 0 \\ 0 & R_s & 0 \\ 0 & 0 & R_s \end{bmatrix}\begin{bmatrix} i_a \\ i_b \\ i_c \end{bmatrix} + \frac{d}{dt}\begin{bmatrix} \lambda_a \\ \lambda_b \\ \lambda_c \end{bmatrix} \tag{A.9}$$

Multiplying equation (A.8) with equation (A.9) gives the voltage equation in the $dq0$-reference frame, (A.10) [39].

$$\begin{aligned} \begin{bmatrix} i_d \\ i_q \\ i_0 \end{bmatrix} &= K_{abc2dq}\begin{bmatrix} R_s & 0 & 0 \\ 0 & R_s & 0 \\ 0 & 0 & R_s \end{bmatrix}\begin{bmatrix} i_a \\ i_b \\ i_c \end{bmatrix} + K_{abc2dq}\frac{d}{dt}\begin{bmatrix} \lambda_a \\ \lambda_b \\ \lambda_c \end{bmatrix} \\ &= \begin{bmatrix} R_s & 0 & 0 \\ 0 & R_s & 0 \\ 0 & 0 & R_s \end{bmatrix}\begin{bmatrix} i_d \\ i_q \\ i_0 \end{bmatrix} + \frac{d}{dt}\begin{bmatrix} \lambda_d \\ \lambda_q \\ \lambda_0 \end{bmatrix} - \omega_r \begin{bmatrix} 0 & 1 & 0 \\ -1 & 0 & 0 \\ 0 & 0 & 0 \end{bmatrix}\begin{bmatrix} \lambda_d \\ \lambda_q \\ \lambda_0 \end{bmatrix} \end{aligned} \tag{A.10}$$

The reference frame transformation from dq to $\alpha\beta$ is achieved with the same procedure as above. The $\alpha\beta$ reference frame is aligned with the phase a-axis and the β-axis is 90° away from the α-axis.

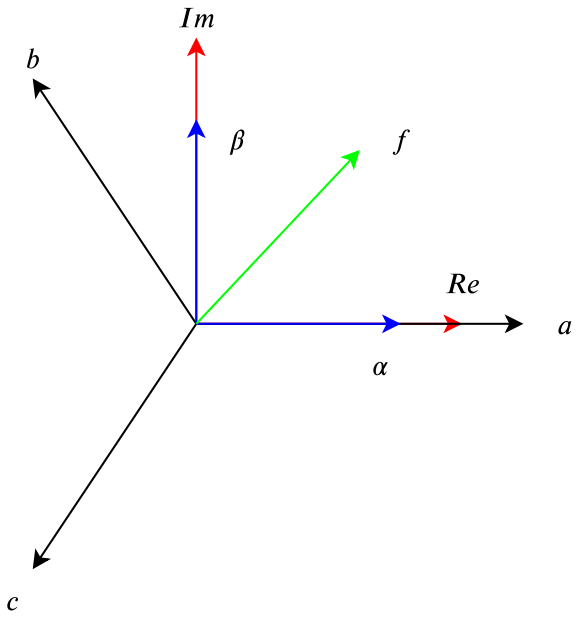

Figure A.3: *$\alpha\beta$ reference frame in the abc reference frame illustration.*

With vector projection the same calculations as illustrated above are done which yields the following transformations matrix, equation (A.11)

$$\begin{bmatrix} f_\alpha \\ f_\beta \\ f_0 \end{bmatrix} = K_{dq2\alpha\beta} = \frac{2}{3} \begin{bmatrix} 1 & cos(120^\circ) & cos(-120^\circ) \\ 0 & sin(120^\circ) & sin(-120^\circ) \\ \frac{1}{2} & \frac{1}{2} & \frac{1}{2} \end{bmatrix} \begin{bmatrix} f_d \\ f_q \\ f_0 \end{bmatrix} \tag{A.11}$$

The transformation matrix is then multiplied with equation (A.10) resulting in a voltage equation in the $\alpha\beta$ reference frame [39].

Appendix B

Voltage Source Inverter

A voltage source inverter (VSI) is a power converter that produces an AC output waveform from a DC voltage source input. The VSI has the capability of controlling the AC output voltage. The inverter controls the magnitude and the frequency of the output with a chosen modulation technique, for instance with Space vector modulation, to emulate a three-phase sinusoidal waveform. This is explained in more detail below. A simplified structure of a two-level voltage source inverter with a DC link is shown in figure B.1, where the DC-link is assumed to be constant, and the rectifier side is omitted for simplicity [15].

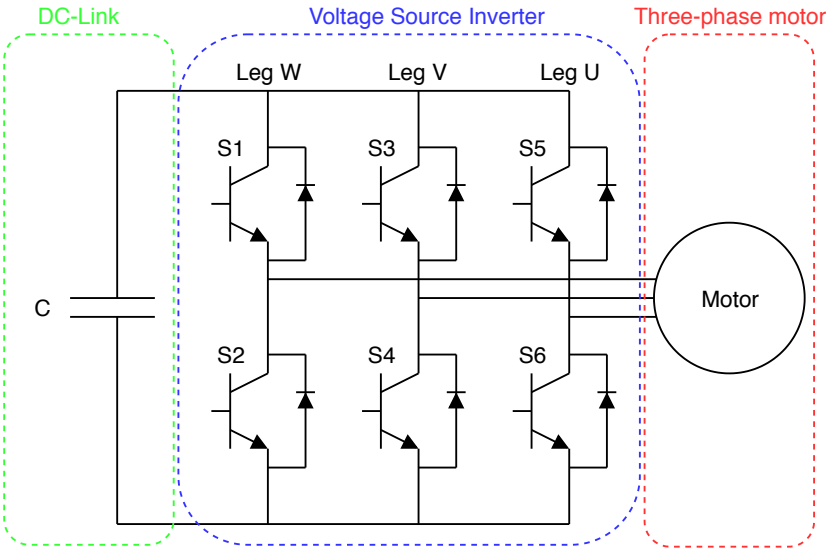

Figure B.1: *A simplified schematic of a VSI where the DC-link is assumed constant and the rectifier omitted.*

B.1 Modulation Technique

Space vector modulation is a modulation technique where the objective is to generate a three-phase sinusoidal waveform where frequency and amplitude can be controlled. Modulation is achieved by properly selecting a switching state of the inverter for each sampling period and then, calculating the appropriate time for each state. From the simplified schematic of the VSI above, figure B.1, it is shown that there are six switches that can either be on or off. However, the switches are in pairs, where S1 and S2 are considered to form one leg, thus the total number of switching states is $2^3 = 8$ [15].

Out of these eight vector configurations, six correspond to different voltages applied. The other two are the so-called zero vectors or when there is zero voltage on the terminals. These vector can be seen in figure B.2.

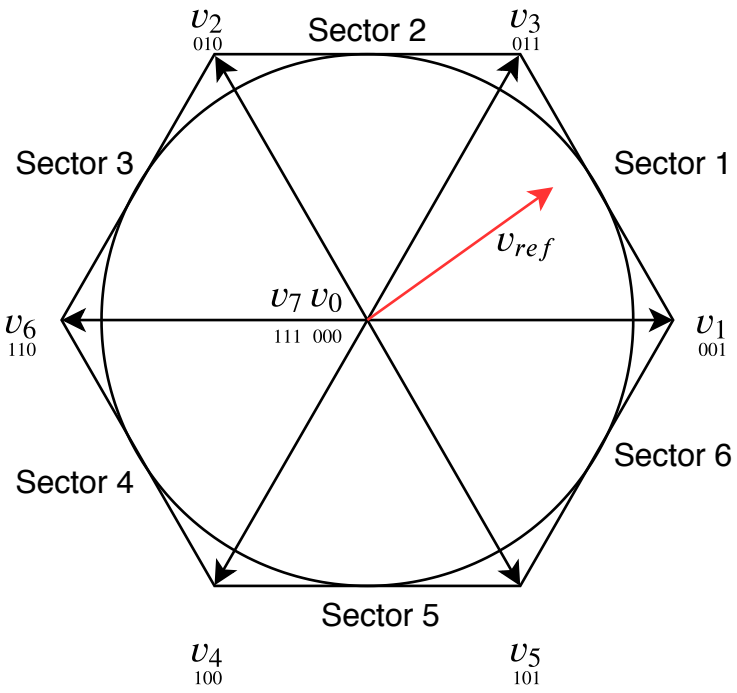

Figure B.2: *Vectors and zero vectors shown in correspondence with their physical location inside the stator.*

These vectors are divided into six sectors where each sector represents a different pair of switches. If each leg of the inverter is represented with 1 for on state (top switch closed and bottom switch open) and 0 for off-state (top switch open and bottom switch closed) a binary number can be formed for each vector as seen in figure B.2.

The reference is a space vector. This vector is acquired by adding the balanced *abc* voltage vectors together. This means, that the space vector is in the $\alpha\beta$-reference frame. The amplitude and angle of the space vector are calculated with the equations below.

$$V_{ref} = \sqrt{v_\alpha^2 + v_\beta^2} \tag{B.1}$$

$$\theta = tan^{-1}(\frac{v_\beta}{v_\alpha}) \tag{B.2}$$

The sector in which the reference voltage vector is located is identified, equation B.3, and determines the vector which will be used to incorporate the reference [15].

$$\theta_k = \theta - (k-1)\frac{\pi}{3} \quad for \quad 0 \leq \theta_k \leq \frac{\pi}{3} \tag{B.3}$$

Where k represents the sector number. Then, the desired reference voltage is transformed to on/off binary signals for each leg of the inverter called duty cycles. The duty cycles d_x, d_y represent the active vectors, and d_z represents the zero vectors. In space vector modulation, the zero vectors are made to be equal. This makes the modulated sinusoidal wave different than the ideal one, by distorting the wave around the peak values. This is shown in figure B.3, the amplitude is normalized.

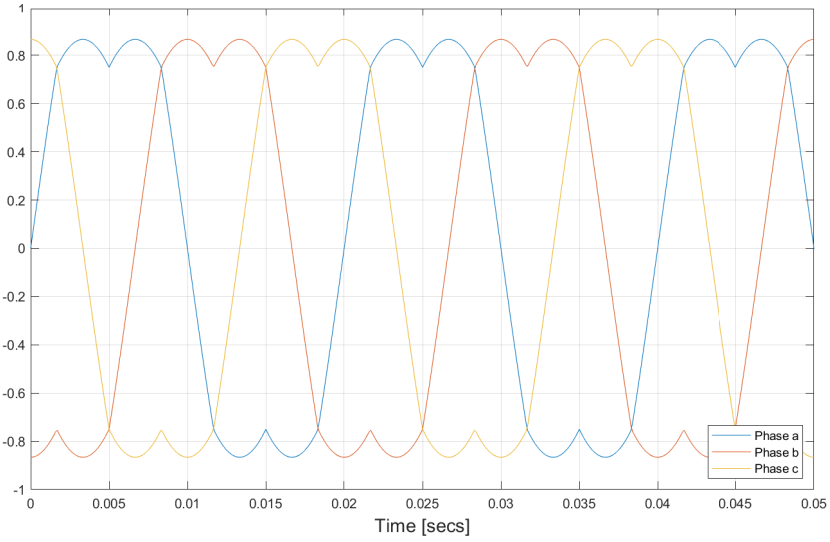

Figure B.3: *SVM waveforms*

The duty cycles are calculated using the following equations where sector 1 from figure B.4 is taken as an example.

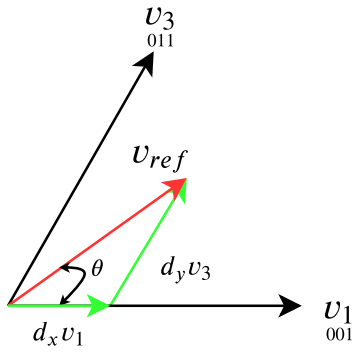

Figure B.4: *Sector 1 with reference vector.*

$$\vec{v}_{ref} = d_x\vec{v}_1 + d_y\vec{v}_3 \tag{B.4}$$

By changing the subscripts, the equations for the other sectors can be acquired as well. This equation can be rewritten such as:

$$d_x = \frac{\sqrt{3}v_{ref}}{v_1}\frac{2}{3}sin(\frac{\pi}{3} - \theta) \tag{B.5}$$

$$d_y = \frac{\sqrt{3}v_{ref}}{v_3}\frac{2}{3}sin(\theta) \tag{B.6}$$

$$d_z = t - (d_x + d_y) \tag{B.7}$$

Where v_{ref} and θ are known, t is sampling period [40]. The same procedure can be used for sectors 2 to 6 if θ_k for the kth sector is used instead of θ.

Finally, the space vector sequence is made to make the appropriate gate signals. To reduce the switching frequency, it is necessary to arrange the switching sequence so that the transition from one section to the next section is done by switching only one leg at a time. The zero vectors are the same, thus, the time interval d_z is split and distributed equally at the beginning and the end of the sampling period t. The duty cycle of each period adds up to the sampling period t.

For example, for sector 1, the switching sequence for the reference vector is $V_0, V_1, V_3, V_7, V_3, V_1, V_0$. Each of the switches in the inverter only turns on and off once per sampling period. Therefore, the sampling frequency is equal to $fs = \frac{1}{t}$ [15]. In a practical application, the duty cycles are calculated by comparing a reference signal with a high-frequency triangular carrier wave. This is visualized in figure B.5, taking sector 1 as an example again.

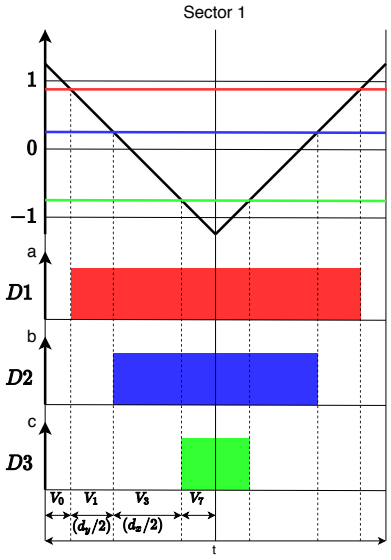

Figure B.5: *A visual representation of duty cycle is calculation in sector 1 for an arbitrary vector.*

For each sector, the gate signals and their sequence is generated as discussed in [40].

Appendix C

Stability of the Super Twisting Observer

The proof of the stability of the equilibrium point ($x = 0$) starts with the introduction of the Super Twisting Algorithm, as it was originally proposed in [31].

$$\begin{aligned} \dot{x}_1 &= -k_1\sqrt{\mid \tilde{x}_1 \mid}sign(\tilde{x}_1) + x_2 + \rho_1(x_1, t) \\ \dot{x}_2 &= -k_2 sign(\tilde{x}_1) + \rho_2(x_2, t) \end{aligned} \tag{C.1}$$

At first, it is assumed that perturbation terms are zero (ρ_1, ρ_2 = 0), later on, the proof of the stability will be extended when these terms are not zero. To prove the stability of the equilibrium point and to adequately choose the observer gains, k_1 and k_2, the Lyapunov theory is utilized.

A strong Lyapunov candidate function is chosen as seen in equation (C.2). This was first proposed in [41]. The strong adjective here means that the candidate function $V(x)$ is Positive definite (P.D) and $\dot{V}(x)$ is Negative definite (N.D). If the candidate function is proven to have the above mentioned properties, that will drive the error to zero in finite time, $\dot{\sigma} = \sigma = 0$ for $t \to t_{reaching} < \infty$.

$$V(x) = 2k_2 \mid x_1 \mid + \frac{1}{2}x_2^2 + \frac{1}{2}(k_1\sqrt{\mid x_1 \mid}sign(x_1 - x_2)^2 \tag{C.2}$$

This function is continuous everywhere, but not continuously differentiable, because of the point $x_1 = 0$. It was shown in [41], that the Lyapunov theorem can be applied in such cases like this, by considering only the differentiable points of $V(x)$.

It can be seen that if $k_2 > 0$, then $V(x)$ a positive definite function. Furthermore, $V(x)$ is globally radially unbounded.

The candidate function may be represented in a quadratic form.

$$V(x) = \zeta^T P \zeta \tag{C.3}$$

Where the P matrix is shown in equation (C.4), and ζ vector is shown in equation (C.5).

$$P = \frac{1}{2}\begin{bmatrix} 4k_2 + k_1^2 & -k_1 \\ -k_1 & 2 \end{bmatrix} \tag{C.4}$$

$$\zeta^T = \begin{bmatrix} \sqrt{|\ x_1\ |} sign(x_1) & , x_2 \end{bmatrix} \tag{C.5}$$

Differentiation of the candidate function $V(x)$ yields the next expression:

$$\dot{V} = -\frac{1}{\sqrt{|\ x_1\ |}} \zeta^T Q \zeta \tag{C.6}$$

Where Q is defined in equation (C.7).

$$Q = \frac{k_1}{2}\begin{bmatrix} 2k_2 + k_1^2 & -k_1 \\ -k_1 & 1 \end{bmatrix} \tag{C.7}$$

Therefore, $\dot{V}(x)$ is negative definite (N.D.) when Q matrix is positive definite. To check whether the Q matrix is positive definite or not, the eigenvalues of the matrix have to be calculated.

The definition for the eigenvalue calculation is presented in equation (C.8).

$$det(\lambda \boldsymbol{I} - Q) = 0 \tag{C.8}$$

Substituting Q matrix into equation (C.8) yields:

$$det(\begin{bmatrix} \lambda - -\frac{k_1}{2}(2k_2 + k_1^2) & k_1 \\ k_1 & \lambda - 1 \end{bmatrix}) = 0 \tag{C.9}$$

$$(\lambda - \frac{k_1}{2}(2k_2 + k_1^2))(\lambda - 1) - k_1^2 = 0 \tag{C.10}$$

Using the quadratic formula to solve the problem, equation (C.11) is acquired.

$$k_1^2(4+k_2^2)+k_1^4k_2+\frac{k_1^6}{4}+2k_1k_2-3k_1^3>-1 \tag{C.11}$$

The relation in equation (C.11) is always true when the gains are positive, $k_1, k_2 > 0$. This can be shown be considering 4 cases based on whether $k_1 > 1$, $k_2 > 1$, $1 > k_1 > 0$ or $1 > k_2 > 0$. Therefore, the matrix in question becomes a positive definite matrix, which ensures that $\dot{V}$ is negative definite for all cases.

It was also shown in [41], but will not be explained in details here, that the reaching time of the sliding mode of observer can be calculated such as: $t_{reaching} = \frac{2\sqrt{V}(x_0)}{\gamma}$, where $\gamma = \frac{\sqrt{MIN}(P)MIN(Q)}{MAX(P)}$.

In conclusion, it is proven that by choosing the observer gains $k_1, k_2 > 0$, the origin $x = 0$ is an equilibrium point that is strongly globally asymptotically stable. This is true under the condition that the perturbation terms are zero.

The proof of the stability can be extended when the perturbation terms are not zero, but bounded such as shown in equation (C.12), where $\delta_1, \delta_2 > 0$ [41].

$$\begin{aligned} \mid \rho_1 \mid &\leq \delta_1\sqrt{\mid x_1 \mid} \\ \mid \rho_2 \mid &\leq \delta_2 \end{aligned} \tag{C.12}$$

In this case, the derivative of the candidate function becomes:

$$\dot{V} = -\frac{1}{\sqrt{\mid x_1 \mid}}\zeta^T Q\zeta + \frac{\rho_1}{\sqrt{\mid x_1 \mid}}q_1^T\zeta + \rho_2 q_2^T\zeta \tag{C.13}$$

Where q_i is defined in equation (C.14).

$$\begin{aligned} q_1^T &= \begin{bmatrix}(2k_2+\frac{k_1^2}{2}) & -\frac{k_1}{2}\end{bmatrix} \\ q_2^T &= \begin{bmatrix}-k_1 & 2\end{bmatrix} \end{aligned} \tag{C.14}$$

Using the upper boundaries for the perturbation terms defined in equation (C.12), it can be seen that by omitting the last two terms and introducing the $\tilde{Q}$ matrix, as seen in equation (C.16), the left side of equation (C.15) will be less than or equal to the right side [41].

$$\dot{V} \leq -\frac{1}{\sqrt{\mid x_1 \mid}}\zeta^T\tilde{Q}\zeta \tag{C.15}$$

$$\tilde{Q} = \frac{k_1}{2}\begin{bmatrix} 2k_2 + k_1^2 - (\frac{4k_2}{k_1} + k_1)\delta_1 - 2\delta_2 & -(k_1 + 2\delta_1 + \frac{2\delta_2}{k_1}) \\ -(k_1 + 2\delta_1 + \frac{2\delta_2}{k_1}) & 1 \end{bmatrix} \tag{C.16}$$

In this case, $\dot{V}(x)$ is negative definite, when $\tilde{Q}$ matrix is positive definite. This can be assured by choosing the gains as presented in equation (C.17) [41]. This equation is acquired by using the eigenvalue formula again.

$$\begin{aligned} k_1 &> 2\delta_1 \\ k_2 &> k_1 \frac{5\delta_1 k_1 + 6\delta_2 + 4(\delta_1 + \delta_2/k_1)^2}{2(k_1 - 2\delta_1)} \end{aligned} \tag{C.17}$$

For certain applications, it might be true that $\rho_2 = 0$. The equation for the gains can be simplified, by setting δ_2 to be zero, as seen in equation (C.18).

$$\begin{aligned} k_1 &> 2\delta_1 \\ k_2 &> k_1 \frac{5\delta_1 k_1 + 4\delta_1^2}{2(k_1 - 2\delta_1)} \end{aligned} \tag{C.18}$$

The reaching time can be calculated again using the matrix $\tilde{Q}$, $\tilde{t}_{reaching} = \frac{2\sqrt{V}(x_0)}{\tilde{\gamma}}$, where $\tilde{\gamma} = \frac{\sqrt{MIN}(P)MIN(\tilde{Q})}{MAX(P)}$. The proof for this can be seen in [41], but it is not shown in this report.